PHILOSOPHICAL TRANSACTIONS OF THE ROYAL SOCIETY A MATHEMATICAL, PHYSICAL & ENGINEERING SCIENCES

Analysis of Large-Strain Shear in Rate-Dependent Face-Centred Cubic Polycrystals: Correlation of Micro- and Macromechanics

S. Harren, T. C. Lowe, R. J. Asaro and A. Needleman

Phil. Trans. R. Soc. Lond. A 1989 **328**, 443-500
doi: 10.1098/rsta.1989.0048

Phil. Trans. R. Soc. Lond. A **328**, 443–500 (1989) [443]
Printed in Great Britain

ANALYSIS OF LARGE-STRAIN SHEAR IN RATE-DEPENDENT FACE-CENTRED CUBIC POLYCRYSTALS: CORRELATION OF MICRO- AND MACROMECHANICS

BY S. HARREN[1], T. C. LOWE[2], R. J. ASARO[1] AND A. NEEDLEMAN[1]
[1]*Division of Engineering, Brown University, Providence, Rhode Island* 02912, *U.S.A.*
[2]*Sandia National Laboratories, Livermore, California* 94551-0969, *U.S.A.*

(*Communicated by M. F. Ashby, F.R.S. – Received* 27 *January* 1988)

CONTENTS

Micro- and macroscopic aspects of large-strain deformation are examined through analyses of shear by using physical and phenomenological models. Past experiments and analyses are first reviewed to reveal current issues and put the present work in perspective. These issues are addressed by a complete set of simulations of large-strain shear with a finite-strain, rate-dependent polycrystal model. The model is based on a rigorous constitutive theory for crystallographic slip that accounts for the development of crystallographic texture and the effects of texture on constitutive response. The influences of strain hardening, latent hardening, strain-rate sensitivity, boundary constraints, and initial textures on texture evolution and constitutive

response are studied. Coupled stress and strain effects such as axial elongation during unconstrained shear and the development of normal stresses during constrained shear are related to material properties, boundary constraint and texture. The formation of ideal textures and their role in determining polycrystalline behaviour is discussed in quantitative terms. Large-strain shear is also studied by using several phenomenological constitutive theories including J_2-flow theory, J_2-corner theory, and two versions of finite-strain kinematic hardening theory. The behaviours predicted by these phenomenological theories and the physically based polycrystal model are directly compared. A noteworthy outcome is the close correspondence found between the predictions of J_2-corner theory and those of the micromechanically based physical model.

1. Introduction

Large-strain deformation behaviour of metals and alloys is commonly studied by experimental and theoretical analyses of shear. The aim of the experimental studies is to document strain hardening at large strains, thus providing a base for developing more complete, and physically sound, constitutive laws. Recent work has additionally been aimed at correlating initial microstructures, along with the evolution of microstructure and texture, with multiaxial large-strain response (see, for example, Hecker & Stout 1982; Budiansky *et al.* 1951; Montheillet *et al.* 1984; Hughes 1986). This ambitious yet vital approach is new, and comprehensive studies of even microstructurally simple 'model' systems have yet to be completed. The present work is specifically aimed at contributing to the theoretical framework for guiding such experimental studies, interpreting them, and formulating rigorous three-dimensional constitutive theories for strain-rate-dependent materials deformed to arbitrarily large strains. Such a framework is necessary because of the complexity of the observed behaviour and the difficulty in representing it with continuum constitutive laws.

Shear deformation, in particular through torsion, is used to achieve large strains because of the inherent geometric stability of this state. None the less, the phenomenology is complicated and intepretation requires theoretical study using models that account for the effects of boundary constraint and material properties such as texture, strain-rate sensitivity, and strain hardening. In the present work the phenomenology of large-strain shear is studied in detail. Axial effects which accompany shear, such as the development of normal strains or stresses, are emphasized because they are experimentally observed to depend sensitively upon material properties. Consequently, these effects provide a focus for testing theoretical models of material response. A recently developed polycrystal model based on strain-rate-dependent crystallographic slip is used to explore the influence of crystallographic strain hardening, latent hardening, and strain-rate sensitivity on the overall shear behaviour. The model can only be implemented numerically and thus the results are those of a number of large computer simulations. The influence of material properties on texture evolution and full constitutive response is studied: a number of novel correlations are made concerning the role of texture, strain-rate sensitivity, strain hardening, and boundary constraint on shear behaviour. In addition, shear behaviour is studied by using various phenomenological theories that are 'calibrated' against the physical (slip) theory. The intent is to distinguish between features of shear deformation that can be described by using classical constitutive relations, recently proposed phenomenological models, and the more detailed crystal plasticity model.

The plan of the paper is as follows. In §1.1 previous experimental and theoretical work on

the shear problem is reviewed to help put our new work in perspective. Section 1.2 presents two classical descriptions of large-strain shear response: that afforded by J_2-flow theory with isotropic hardening and that of an isotropic hyperelastic (deformation theory) constitutive law. In §2 the crystal constitutive theory and the polycrystal physical model are described. A set of homogeneous boundary value problems is presented in §2.2; we will use this set to model various aspects of polycrystalline shear. Grain distributions and 'ideal' textures are described in §§2.3 and 2.4. Numerical results are described in §3. In §4 the predictions of the physical model are compared to those of several recently introduced phenomenological theories: J_2-corner theory and two versions of large-strain kinematic hardening theory. Also in §4, discussion and interpretations of the results are presented. In all of what is presented we have tried to be comprehensive in laying out micromechanical, crystallographic, and continuum phenomenological aspects of the shear problem in the hope that the present paper might provide a conceptual and mathematical framework for future experimental and theoretical studies.

Standard mathematical notations are used throughout. Vectors and higher-order tensors are denoted by bold-faced symbols, the orders of which are clear in context. Products are written in diadic notation, e.g. with $\boldsymbol{e}_1$, $\boldsymbol{e}_2$ and $\boldsymbol{e}_3$ representing a set of orthonormal base vectors,

$$\boldsymbol{B}\cdot\boldsymbol{C} = B_{ij}C_{jk}\boldsymbol{e}_i\boldsymbol{e}_k \qquad \boldsymbol{B}:\boldsymbol{C} = B_{ij}C_{ji}$$

$$\boldsymbol{BC} = B_{ij}C_{kl}\boldsymbol{e}_i\boldsymbol{e}_j\boldsymbol{e}_k\boldsymbol{e}_l \qquad \boldsymbol{aa} = a_ia_j\boldsymbol{e}_i\boldsymbol{e}_j$$

$$\boldsymbol{A}:\boldsymbol{B} = A_{ijkl}B_{lk}\boldsymbol{e}_i\boldsymbol{e}_j \qquad \boldsymbol{B}:\boldsymbol{A} = B_{ji}A_{ijkl}\boldsymbol{e}_k\boldsymbol{e}_l.$$

Summation over Latin indices is implied whereas summation over Greek indices is explicitly indicated. Superposed dots are used to denote time derivatives, e.g.

$$\dot{\boldsymbol{B}} = \frac{\partial}{\partial t}\{B_{ij}\boldsymbol{e}_i\boldsymbol{e}_j\}.$$

1.1. *Perspectives on past work*

Experimental and theoretical studies of shear deformation have examined the axial effects that accompany shear. These effects are readily observed in torsion as a small change in length or as axial stresses that develop during twisting. This behaviour has been observed at small elastic strains by Poynting (1909), and at very large plastic strains by Swift (1947), Billington (1976), and Montheillet *et al.* (1984). Identification of the small-strain effect has been attributed to Poynting (1909) who first observed it in wires of steel, brass, and copper. In the present paper, our principal interest is in the large-strain effect, sometimes referred to as the 'Swift effect' (Swift 1947). Most of the experimental measurements and analytical results discussed in the following section will be re-evaluated in the context of the model calculations in later sections.

1.1.1. *Axial effects in shear: mechanical measurements*

Swift (1947) initially investigated length changes in rods and tubes of brass, aluminium, steel and copper during large-strain torsion. The influence of specimen geometry and material properties upon these changes were examined in some detail. From his work, and subsequent measurements by others, it has been shown that most initially isotropic metals tend to elongate

PHILOSOPHICAL TRANSACTIONS OF THE ROYAL SOCIETY A MATHEMATICAL, PHYSICAL & ENGINEERING SCIENCES

during torsion when the specimen's ends are free, or to develop compressive axial stresses when the ends are fixed. The magnitude of the elongation varies between metals but is typically of the order of 10% for a shear strain of 3. Although a near-parabolic relation between shear strain and axial strain has been most often observed, Swift found that the ratio of axial strain to shear strain was constant and approximately 0.03 for brass and stainless steel. He also noted that tests using tubes showed as much as 50% more extension compared to similar tests on solid rods. Billington (1976) and Ronay (1968) also observed greater extensions in thin-walled cylinders than in solid rods. In addition, in Billington's experiments, the rate of axial extension decreased dramatically when his thin-walled cylinders contracted enough radially to contact an inner plug. Stout (1984) observed similar behaviour in thin-walled tubes of brass into which a mandrel was inserted during torsion. In each case the plug, or mandrel, constrained the axial effect in the same manner that it was constrained during torsion of solid rods. Ronay (1966) observed a similar dependence of the magnitude of the Swift effect upon specimen type in fixed-end torsion experiments. The compressive stresses in a tube with fixed ends were typically twice as large as those estimated at the outer radius of the comparable solid rod. In §3 we demonstrate how constraints that prevent contraction in the shearing direction, which would prevent hoop strains in the case of torsion, nearly eliminate axial strains.

The effect of strain hardening on axial effects was judged to be of great significance by Swift (1947). His experiments showed the largest axial elongations in metals having the strongest strain hardening. For lead, which showed essentially no strain hardening at intermediate strains and room temperature, his sample contracted. Swift's conclusion that axial elongations were related to strain hardening was contradicted by the experiments of Billington (1976) who observed continuous elongations in iron independent of the hardening. Montheillet *et al.* (1984) suggested that the development of compressive axial stresses for 'fixed-end' torsion could be associated with the high rates of hardening observed at small strains and low temperature. Similarly, they associated observed tensile stresses during torsion with the negligible hardening rates observed at very large strains and intermediate temperature. The effect of work hardening upon axial stress response will be treated in §3 by using the crystal plasticity model. There it is shown that strain hardening *per se* affects the magnitude of the normal stresses (in much the same way as it affects the increase in shear strength) while leaving the qualitative trends exhibited by these stresses essentially unaffected.

Although there exists no systematic study of the effects of initial texture upon the Swift effect, axial effects have been compared in copper twisted in the as-received condition and after heat treatment at 550 °C for 16 h (Billington 1976). Axial extension was much smaller in the heat-treated copper, which presumably had a more nearly isotropic texture because of annealing or recrystallization. Swift prestrained mild steel samples by 18% in tension before twisting. He found that these samples contracted axially before extending like unprestrained samples. Similar axial contraction transients were observed following reversals of the twisting direction by Swift (1947) and others (see, for example, Gil-Sevillano *et al.* 1975). We have simulated Swift's reverse torsion tests using the rate-dependent polycrystal (crystal plasticity) model and the results are presented in §3. We indeed find that there are transient axial contractions and the phenomenology is quite similar to that reported by Swift although the magnitudes of our calculated strains are much higher. This may also be because of the effects of the constraints that act on the specimen as noted above. Aside from these transient contractions, however, axial strains have been found by experiment, and our calculations, to be cumulative, independent of the direction of shear.

PHILOSOPHICAL TRANSACTIONS OF THE ROYAL SOCIETY A MATHEMATICAL, PHYSICAL & ENGINEERING SCIENCES

Strain rate dependence of the Swift effect has been investigated through experiments done at different strain rates and temperatures. Billington (1976) compared high-rate torsion measurements ($100\ s^{-1} < \dot{\gamma} < 1000\ s^{-1}$) with quasi-static torsion data and concluded that no axial effects occurred at very high strain rates. Montheillet *et al.* (1984) examined a lower range of shear rates and found that the axial forces changed with rate. The ratio of axial stress to shear stress increased with strain rate in aluminium deformed at 200 °C but showed no systematic variation in copper deformed at 300 °C. However, there was a clear trend for this ratio to decrease with increasing temperature for both aluminium and copper. This decrease in the magnitude of the Swift effect at higher temperatures was accompanied by a tendency for axial tensile stresses to develop at large strains. Furthermore, the data of Montheillet *et al.* show that the amount of strain required before axial stresses change from compression to tension decreases with increasing temperature. An explanation for the dependence of the Swift effect upon temperature was suggested by them in terms of the effects of temperature upon texture development. Tensile axial stresses developed at elevated temperatures have also been reported by Swift (1947), Portevin (1970) and Hughes (1952). The experiments by Portevin using chromium steels showed that the tensile and compressive stress transients during hot torsion were dramatically affected by variations in the chromium content and the corresponding variations in microstructure. One might speculate several origins of these variations: changes in stacking fault energy, crystal structure, or phase composition could each be significant. This level of microstructural detail is not addressed in the present study because of a lack of sufficient experimental documentation.

1.1.2. *Axial effects in shear: deformation-induced textures*

1.1.2.1. *Ideal torsion textures.* The ideal textures that result from torsion can be derived from the symmetry of shear and the physics of slip. As suggested by van Houtte & Aernoudt (1976), the symmetry of torsion requires that these textures (hereafter referred to as torsion textures) be centrally symmetric about the radial direction (i.e., independent of a 180° rotation about the radial direction). Canova *et al.* (1984) have classified three texture components based upon considerations of the geometry of shear and crystallographic slip: a partial A-fibre texture A_f having {111} planes normal to the axial direction, a partial B-fibre texture B_f having ⟨110⟩ directions aligned with the shear direction, and a C-texture, which is the discrete orientation within the B-fibre that has a cube direction aligned with the torsion axis. These components are referenced below to describe experimental textures and are illustrated in our computed pole figures. A more thorough discussion of ideal torsion textures is presented in §2.4.

1.1.2.2. *Experimental torsion textures.* X-ray measurements of shear textures have been reported by several investigators (see Montheillet *et al.* 1984; Aernoudt & Gil-Sevillano 1973; Backofen 1950; Gibbard 1951; van Houte & Aernoudt 1976; Backofen & Hundy 1953; Williams 1962). In general, combinations of the ideal C-texture and components of the A-texture have been reported in copper, aluminium, and brass. Other textures have been less commonly reported. The relative intensities of A_f, B_f, and C-textures differ between materials and vary with strain, temperature, and prior texture. However, because of the complexity of shear textures and the limitations of pole figure measurements, it is difficult to resolve the sometimes subtle texture characteristics that influence axial effects. Nevertheless, some significant observations are noted which will be discussed later along with our model predictions. Measurements of Williams and Backofen & Hundy demonstrated that the pole figures were, as deduced by van Houtte & Aernoudt (1976) centrosymmetric. Looking ahead

to the {111} pole figures presented in §3, we note they are most usefully plotted such that the pole of the shear direction lies at the outer right on the perimeter and the normal to the shearing direction lies at the top pole (see, for example, figure 3). In this orientation centrosymmetry implies that opposing quadrants such as the first and third are identical, as are the second and fourth. During simple shear along the positive x_1-direction the principal directions of the rate of deformation lie at 45° clockwise to the vertical axis; thus orientations in the second and fourth quadrants are shortened and orientations in the first and third quadrants are lengthened. Textures produced by positive and negative shear should therefore exhibit mirror symmetry with respect to each other on such a {111} pole figure with the radial direction at the centre.

A dependence of axial effects upon texture was suggested by Montheillet *et al.* (1984) in connection with their experiments. They interpreted axial effects in terms of their reported observations of rotations of the ideal texture components about the radial direction, as suggested by the analyses of Gil-Sevillano *et al.* (1975). Note that they use the notation 'A' and 'B' to designate discrete crystallite orientations within the A_f and B_f fibres, respectively. 'A' refers to $\{1\bar{1}1\}\langle 110\rangle$ orientations and 'B' refers to $\{\bar{1}12\}\langle 110\rangle$ orientations. At low strains and low temperature, the development of compressive axial stresses in rods of aluminium and copper was attributed to rotations of A- and C-ideal textures opposite to the sense of shear. Similarly, at high strains and intermediate temperature, the development of tensile axial stresses was attributed to rotation of the A-component of ideal texture in the same sense as shear. At higher temperatures the absence of axial forces was attributed to the increasing presence of the B-texture and the decreasing intensity of the A-texture. In a later paper the effects of these textures and their rotations upon axial stresses were quantified by Montheillet *et al.* (1985) in a phenomenological model. However, the effects of temperature upon texture development have not been explained except at high temperatures where the influence of dynamic recrystallization is obvious. Also, the effects of sample geometry, torsion boundary conditions (fixed against free end), and strain-rate sensitivity upon texture development have not been assessed even though these parameters are known to strongly influence the Swift effect. These effects will be considered in the present calculations. A noteworthy outcome of our calculations is that we find that the unrotated ideal partial A_f-fibre texture itself produces a tensile force in the case of fixed ends. This may provide a simple explanation of tensile stresses in cases where this component becomes dominant. However, looking ahead to our numerical results in §§3.1 and 3.2, we find that the maximum axial tensile stresses occur at stages in the deformation where the intensity of the A_f-fibre is decreasing and is no longer dominant. As will be explained in §4, these maxima result from large numbers of grains with orientations outside of the ideal texture orientations. On the other hand, we find no rotations of the textures following shear with fixed ends. When the shear is unconstrained, however, and normal strains are allowed texture rotations do occur.

1.1.3. *Axial effects in shear: theoretical analyses*

The elongation of metals during shear has been described in both continuum models and strain rate independent Taylor-like models of deformation. Analyses with continuum phenomenological constitutive models by Poynting (1909), Hill (1950), Nadai (1950), Rivlin (1953), Ronay (1967, 1968), Billington (1976) and Van Arsdale *et al.* (1980) have shown that axial extensions or compressive axial stresses should be expected during torsion. This is

illustrated in the next section with a hyperelastic constitutive model. In these models, the prediction of axial effects is derived from several different arguments. Poynting (1909) used a simple geometric model to show the directions of maximum extension and contraction during simple shear. He then determined the stress state required to satisfy equilibrium given a small elastic shear strain. The axial extension in the absence of an axial force is then found by superposition of equilibrium states. Rivlin (1953) considered several torsion problems using second-order elasticity theory. He also used superposition to compute axial extension from a solution for fixed length. Billington (1976) considered inelastic torsion of an isotropic, incompressible strain hardening material by using the large-strain deformation theory of Hahn (1974). This approach yields axial effects that are entirely geometric in origin, just as found in the above elastic analyses. Van Arsdale *et al.* 1980) also treated inelastic torsion, but used the constitutive relations of Hart (1976). Hart's model includes an internal stress tensor variable. Axial effects are found to result entirely from the rotation of this tensor because of the material rotations that occur during torsion. All of these analyses, based on simple phenomenological models, predict an increasing axial strain or stress with increasing shear strain, but never the complex trends that have been observed experimentally, especially by Montheillet *et al.* (1984).

Some of these models approximate certain aspects of the Swift effect. For twisting with free ends, Van Arsdale *et al.* (1980) and Poynting (1909) predicted the near-parabolic relation observed between axial strain and shear strain at strains less than unity. The effects of torsion specimen wall thickness upon the Swift effect were treated theoretically by Rivlin (1953) and Ronay (1968). It was shown that axial effects increase with decreasing wall thickness and that in the limit, the axial stress in an ideal thin-walled cylinder will be twice that of a solid rod. These analyses assumed an ideally plastic material. In the present work geometric effects and the effects of work hardening will be considered.

Taylor-like deformation models (including the present model) account directly for grain rotations and the resulting textural anisotropy which strongly influences the Swift effect. In the past this calculational approach has been only marginally successful in the modelling of axial effects in shear such as the texture rotations reported in the experimental measurements by Gil-Sevillano *et al.* (1975). The present model has been much more successful in comparison where such rotations are a dominant feature of the calculated textures when normal strains are allowed to develop. This success is directly attributable to our mixed boundary value formulation of the problem. Montheillet *et al.* (1985) used a hybrid approach to calculate axial stresses due to individual texture components and their rotations about the radial direction. They found that the A, B, and C-textures do not of themselves produce axial stresses. However, when rotated, the A and C-textures produce axial effects that depend upon the direction of rotation. The B-texture produces no axial effect regardless of rotation. For negative torsion with fixed ends (which corresponds to simple shearing in the negative x_1-direction) the self-symmetric $\{\bar{1}11\}\langle 112\rangle$ and $\{11\bar{1}\}\langle 112\rangle$ components of the A-fibre have opposite effects, the former always causing tensile axial stresses and the latter always causing compressive axial stresses. These results (rotations aside) are consistent with the ideal texture calculations presented in §3. By using the quantitative results of their model, the complex axial stress histories and corresponding texture evolution measured by Montheillet *et al.* (1984) were reconciled in terms of the relative intensity and rotations of the ideal texture components. A similar analysis will be presented based upon the present model calculations.

1.2. *Large-strain shear for classical constitutive relations*

In this section we introduce the shear problem to be studied and provide solutions to it for materials obeying two simple constitutive laws, namely an isotropic hyperelastic theory and J_2-flow theory with isotropic hardening. This provides additional pespective on the model results described in §3.

For the circular cross sections widely used in the torsion testing of ductile metals at finite strain, torsion gives rise to inhomogeneous simple shearing, possibly combined with uniaxial or biaxial stretching. For a thin-walled circular section the deformations are nearly homogeneous and correspond to combined simple shear and plane strain extension, provided that the thickness of the tube remains constant. The kinematics of the torsion test and its relation to simple shear are discussed by Shrivastava *et al.* (1982) for solid circular bars, and by McMeeking (1982) for thin-walled tubes. Here, we confine attention to homogeneous combined simple shear and plane strain extension deformations, which include simple shear as a specific case. Although the main interest in these modes of deformation stems from their relation to the deformation modes encountered in torsion tests, we note that finite simple shear tests have been done by Williams (1962). Comparisons between our model results and Williams's measurements of shear textures are provided in §3.

The block shown in figure 1 is to be subjected to extension-shear deformations characterized by the shear strain γ and the extensional stretch e. With allusion to a thin-walled torsion tube in mind, the stretch e may be construed to be the stretch in the specimen's axial direction. In our polycrystal model calculations, four different constraints are imposed on the sheared block, one of which essentially fixes the deformation to be simple shear, and another of which allows significant extensions to develop along with the shearing. In this section we consider only plane deformations. Furthermore, to illustrate the sensitivity of the shear response to the constitutive characterization of the material, we consider two classical rate-independent material models: a hyperelastic solid and an isotropically hardening rigid-plastic solid. In each case we confine attention to incompressible materials. Furthermore, the constitutive relations are specified so that the uniaxial tension (and hence pure shear) response of these two material models is identical. The deformation gradient $\boldsymbol{F}$ is given by $\boldsymbol{F} = \partial \boldsymbol{x}/\partial \boldsymbol{X}$, where $\boldsymbol{x}$ represents the current position of a material point that is located in the reference state at $\boldsymbol{X}$. Both $\boldsymbol{x}$ and $\boldsymbol{X}$, and thus the components of $\boldsymbol{F}$, are referred to a fixed set of laboratory axis $\boldsymbol{e}_1$, $\boldsymbol{e}_2$ and $\boldsymbol{e}_3$. For the block subject to plane stretching and shear, as illustrated in figure 1, $\boldsymbol{F}$ can be written as

$$\boldsymbol{F} = \begin{bmatrix} 1/e & \gamma \\ 0 & e \end{bmatrix}, \tag{1.1}$$

where e is the stretch normal to the shearing plane and $\gamma = e \tan \phi$ is the shear. By using the polar decomposition theorem, $\boldsymbol{F}$ can also be written as

$$\boldsymbol{F} = \boldsymbol{V} \cdot \boldsymbol{R}, \tag{1.2}$$

where $\boldsymbol{V}$ is the left stretch tensor and $\boldsymbol{R}$ is the rotation tensor. We note that $\boldsymbol{R}$ is a pure rotation and $\boldsymbol{V}$ is symmetric and represents a pure deformation. The two eigenvalues of $\boldsymbol{V}$ are related by $\lambda_{\mathrm{II}} = 1/\lambda_{\mathrm{I}}$ because of the assumed incompressibility; the principal directions are related for

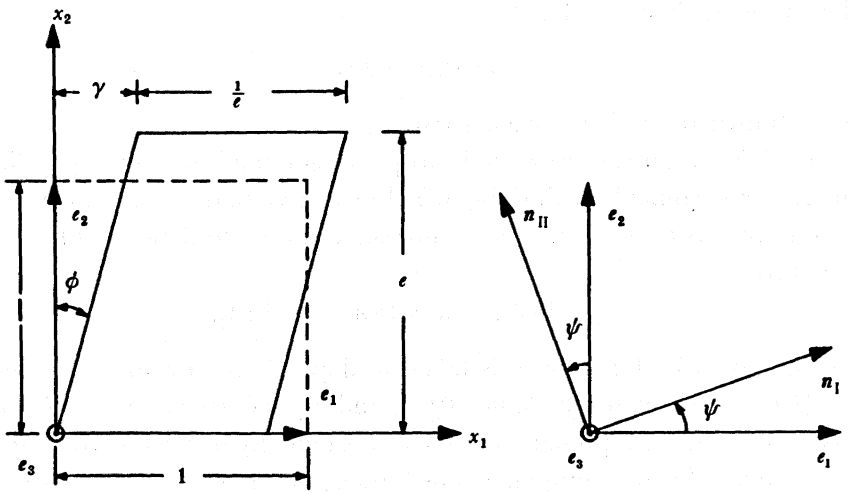

FIGURE 1. Schematic illustration of a block subjected to shear with shear strain γ and axial extension e; $\boldsymbol{n}_I$ and $\boldsymbol{n}_{II}$ are the orthonormal eigenvectors of the left stretch tensor, and $\boldsymbol{e}_1$, $\boldsymbol{e}_2$ and $\boldsymbol{e}_3$ form a fixed orthonormal basis.

this plane situation as $\boldsymbol{n}_{II} = \mathrm{d}\boldsymbol{n}_I/\mathrm{d}\psi$, where ψ is the angle $\boldsymbol{n}_I$ makes with the x_1-axis. Thus

$$\boldsymbol{n}_I = \cos\psi \boldsymbol{e}_1 + \sin\psi \boldsymbol{e}_2, \tag{1.3$_1$}$$

$$\boldsymbol{n}_{II} = -\sin\psi \boldsymbol{e}_1 + \cos\psi \boldsymbol{e}_2, \tag{1.3$_2$}$$

and

$$\boldsymbol{V} = \lambda_I \boldsymbol{n}_I \boldsymbol{n}_I + \lambda_{II} \boldsymbol{n}_{II} \boldsymbol{n}_{II}. \tag{1.3$_3$}$$

With the definition $\mu \equiv \frac{1}{2}(e + 1/e)$, it may be shown by solving the eigenvalue problem for $\boldsymbol{V}$ that

$$\lambda_I = \frac{1}{\lambda_{II}} = \sqrt{\left(\mu^2 + \frac{\gamma^2}{4}\right)} + \sqrt{\left(\mu^2 + \frac{\gamma^2}{4} - 1\right)}, \tag{1.4}$$

and

$$\psi = \arctan\left(2\chi/e\gamma\right) \tag{1.5}$$

with

$$\chi \equiv \mu^2 - \frac{\mu}{e} - \frac{\gamma^2}{4} + \sqrt{\left[\left(\mu^2 + \frac{\gamma^2}{4}\right)\left(\mu^2 + \frac{\gamma^2}{4} - 1\right)\right]}. \tag{1.6}$$

With these definitions, and for later reference, we note that

$$\sin 2\psi = \frac{\chi e \gamma}{\chi^2 + (\frac{1}{2}e\gamma)^2}, \tag{1.7$_1$}$$

and

$$\cos 2\psi = \frac{(\frac{1}{2}e\gamma)^2 - \chi^2}{\chi^2 + (\frac{1}{2}e\gamma)^2}. \tag{1.7$_2$}$$

It is also of interest to note that if $\boldsymbol{R}$ is written as

$$\boldsymbol{R} = \begin{bmatrix} \cos\alpha & \sin\alpha \\ -\sin\alpha & \cos\alpha \end{bmatrix}, \tag{1.8}$$

then

$$\alpha = \arctan\left[\gamma/2\mu\right]. \tag{1.9}$$

Note also that if $e \equiv 1$, then $\mu = 1$ and

$$\tan 2\psi = 2/\gamma, \tag{1.10}$$

which is a well-known result (Chadwick 1976).

Hyperelastic solid. For an incompressible isotropic elastic solid, the principal directions of the true (or Cauchy) stress coincide with those of $\boldsymbol{V}$. We assume that the deviatoric parts of stresses are derived from an elastic potential that is further assumed to depend only on the principal logarithmic strains

$$\epsilon_{\mathrm{I}} = \ln \lambda_{\mathrm{I}}, \quad \epsilon_{\mathrm{II}} = \ln \lambda_{\mathrm{II}} = -\ln \lambda_{\mathrm{I}}. \tag{1.11}$$

Furthermore, the potential function Φ is taken to depend only on the 'effective' part of the strain, $\epsilon_{\mathrm{e}} = \sqrt{[\frac{2}{3}(\epsilon_{\mathrm{I}}^2 + \epsilon_{\mathrm{II}}^2)]}$, such that $S_{\mathrm{I}} = \partial\Phi/\partial\epsilon_{\mathrm{I}}$ and $S_{\mathrm{II}} = \partial\Phi/\partial\epsilon_{\mathrm{II}}$, where $\boldsymbol{S}$ is the deviatoric (Cauchy) stress. Then if σ_{m} represents the mean normal (hydrostatic) stress, the above leads to the following results for the components of Cauchy stress on the laboratory axes:

$$\sigma_{12} = \tfrac{1}{\sqrt{3}}\mathrm{d}\Phi/\mathrm{d}\epsilon_{\mathrm{e}} \sin 2\psi, \tag{1.12$_1$}$$

$$\sigma_{11} = \tfrac{1}{\sqrt{3}}\mathrm{d}\Phi/\mathrm{d}\epsilon_{\mathrm{e}} \cos 2\psi + \sigma_{\mathrm{m}}, \tag{1.12$_2$}$$

and

$$\sigma_{22} = -\tfrac{1}{\sqrt{3}}\mathrm{d}\Phi/\mathrm{d}\epsilon_{\mathrm{e}} \cos 2\psi + \sigma_{\mathrm{m}}. \tag{1.12$_3$}$$

Note that $(\sigma_{11} - \sigma_{22})/\sigma_{12} = 2\cot 2\psi$ and thus when $e \equiv 1$, $(\sigma_{11} - \sigma_{22})/\sigma_{12} = \gamma$ from equation (1.10) independent of the particular potential function Φ. This result is also well known (see, for example, Gurtin 1981).

To provide background for the various phenomena discussed above and later in §3, two sets of boundary conditions are considered here. For one set of conditions, the height of the block remains fixed throughout the deformation history so that $e \equiv 1$. In general, normal stresses are required to maintain the fixed height. The other set of boundary conditions requires the normal stresses to vanish so that in this case the block is free to extend.

When the extension is constrained so that $e \equiv 1$, equation (1.7), together with the definition of effective strain and (1.12) yield

$$\sigma_{12} = \tfrac{1}{\sqrt{3}}\mathrm{d}\Phi/\mathrm{d}\epsilon_{\mathrm{e}} \operatorname{sech}(\tfrac{\sqrt{3}}{2}\epsilon_{\mathrm{e}}), \tag{1.13$_1$}$$

$$\sigma_{11} = \tfrac{1}{\sqrt{3}}\mathrm{d}\Phi/\mathrm{d}\epsilon_{\mathrm{e}} \tanh(\tfrac{\sqrt{3}}{2}\epsilon_{\mathrm{e}}) + \sigma_{\mathrm{m}}, \tag{1.13$_2$}$$

and

$$\sigma_{22} = -\tfrac{1}{\sqrt{3}}\mathrm{d}\Phi/\mathrm{d}\epsilon_{\mathrm{e}} \tanh(\tfrac{\sqrt{3}}{2}\epsilon_{\mathrm{e}}) + \sigma_{\mathrm{m}}. \tag{1.13$_3$}$$

When the block is free to expand and there are no normal stresses, $\sigma_{\mathrm{m}} = 0$, and equations (1.12) show that $\cos 2\psi = 0$. From (1.7) this implies that

$$\chi^2 - (\tfrac{1}{2}e\gamma)^2 = 0. \tag{1.14}$$

Factorization of this relation shows that e depends on γ according to

$$e = \sqrt{\{(\tfrac{1}{2}\gamma^2) + \sqrt{[1 + (\tfrac{1}{2}\gamma^2)^2]}\}}. \tag{1.15}$$

With $\sigma_{11} = \sigma_{22} = 0$, equations (1.6) and (1.7$_1$) also show that $\sin 2\psi = 1$ so that according to (1.12$_1$)

$$\sigma_{12} = \tfrac{1}{\sqrt{3}}\mathrm{d}\Phi/\mathrm{d}\epsilon_{\mathrm{e}}. \tag{1.16}$$

Curves of shear stress against shear strain for these two sets of boundary conditions are shown in figure 2 for a material with a power law strain energy function

$$\Phi(\epsilon_e) = \sigma_0/(N+1)\,\epsilon_e^{N+1}/\epsilon_0^N \tag{1.17}$$

with $N = 0.1$ and $\epsilon_0 = 0.002$. For the case $\sigma_{11} = \sigma_{22} = 0$, the development of normal (axial) strain $\epsilon_{22} = \ln e$ is also shown in the figure. For the hyperelastic solid, the shear-stress–shear-strain curve is quite sensitive to the imposed axial constraint. With $e \equiv 1$, the shear stress

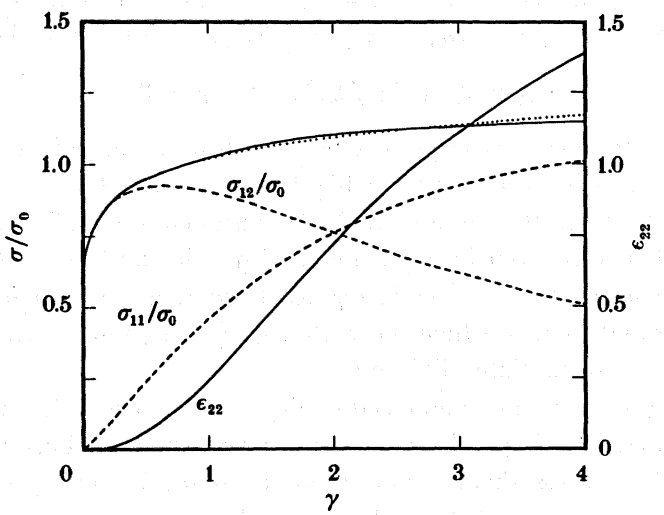

FIGURE 2. Stress against shear strain for a hyperelastic solid and a material described by J_2-flow theory (· · · ·) with isotropic hardening. Two sets of constraints are used, 'constrained' for which $\epsilon_{22} = 0$ (– – – –) and 'unconstrained' for which $\sigma_{11} = \sigma_{22} = 0$ (——). Also shown is the axial strain $\epsilon_{22} = \ln(e)$ for the unconstrained hyperelastic solid (—— referred to the right ordinate).

reaches a maximum, then decreases asymptotically to zero whereas when the ends are free to extend the shear stress monotonically increases. The rotation also depends on the boundary conditions. With $e \equiv 1$, α in equation (1.9) approaches $\frac{1}{2}\pi$ at large γ. On the other hand, with $\sigma_{11} = \sigma_{22} = 0$, it is easily shown that for large γ equation (1.15) implies $e \to \gamma$ so that the angle ϕ in figure 1 approaches $\frac{1}{4}\pi$ as does the angle of rotation α. For $\gamma \ll 1$, $e \approx 1 + \frac{1}{4}\gamma^2$ and a near-parabolic relation between the stretch e and the shear strain is observed, in agreement with earlier classical analyses by Poynting (1909) and Van Arsdale *et al.* (1980).

1.2.1. *J_2-flow theory with isotropic hardening*

For an isotropically hardening rigid-plastic solid, the flow rule takes the form

$$\boldsymbol{D} = 3\dot{\bar{\epsilon}}/2\sigma_e\,\boldsymbol{S}, \quad \sigma_e = \sqrt{(\tfrac{3}{2}\boldsymbol{S}:\boldsymbol{S})}, \quad \dot{\bar{\epsilon}} = \sqrt{(\tfrac{2}{3}\boldsymbol{D}:\boldsymbol{D})}, \tag{1.18}$$

where $\boldsymbol{S}$ is again the deviator of Cauchy stress, σ_e is the effective stress, $\dot{\bar{\epsilon}}$ is the effective strain rate, and $\boldsymbol{D} = \mathrm{sym}\,(\dot{\boldsymbol{F}}\cdot\boldsymbol{F}^{-1})$ is the rate of deformation. Note that $\bar{\epsilon}$, the effective strain obtained by the integration of $\dot{\bar{\epsilon}}$, does not in general correspond to ϵ_e, i.e. the effective strain defined just before relations (1.12). Only for proportional loading histories, i.e., those in which the principal

axes of $\boldsymbol{S}$ do not rotate (e.g. uniaxial tension), do $\bar{\epsilon}$ and ϵ_e coincide. Here, the flow theory material is taken as a pure power law hardening solid, i.e.

$$\sigma_e = \sigma_0(\bar{\epsilon}/\epsilon_0)^N \tag{1.19}$$

with $N = 0.1$ and $\epsilon_0 = 0.002$. With this hardening description, the response in uniaxial tension is the same as that for the hyperelastic solid (1.17).

We now focus on the constrained boundary conditions $e \equiv 1$, where the only non-vanishing components (on $\boldsymbol{e}_i$) of $\boldsymbol{D}$ are $D_{12} = D_{21} = \frac{1}{2}\gamma$. From the first relation of (1.18) we see that the only non-vanishing components of $\boldsymbol{S}$ are $S_{12} = S_{21} = \sigma_{12}$, and under these conditions, the last two relations of (1.18) give $\sigma_e = \sqrt{3}\,\sigma_{12}$ $\alpha\nu\delta$ $\gamma = \sqrt{3}\,\bar{\epsilon}$. Use of these in the power law (1.19) yields

$$\sigma_{12} = \sigma_0/\sqrt{3}\,(\bar{\epsilon}/\epsilon_0)^N, \quad \bar{\epsilon} = \gamma/\sqrt{3}. \tag{1.20}$$

Furthermore, because no normal stresses develop for this material, this is also the solution for the condition $\sigma_{11} = \sigma_{22} = 0$ (where $\sigma_m = 0$ has been chosen). The $\sigma_{12}-\gamma$ curve (1.20) is depicted in figure 2. It is interesting to note that the solution obtained for the hyperelastic solid (under $\sigma_{11} = \sigma_{22} = 0$) is recovered by replacing $\bar{\epsilon}$ with ϵ_e in the first of (1.20). As the figure shows, the J_2-flow theory curve of σ_{12} against γ nearly coincides with that of the hyperelastic material under no normal stresses, which shows that $\epsilon_e(\gamma) \approx \bar{\epsilon}(\gamma)$ in this case (even though the deformation modes are substantially different).

As also shown in figure 2 these two material models predict very different normal stress and normal strain responses. The hyperelastic constitutive relation predicts a strong qualitative dependence of the shear-stress–shear-strain response on the boundary conditions, whereas isotropic hardening rigid-plastic J_2-flow theory predicts a response independent of these boundary conditions. What is also significant in the present context is the dependence of material rotation on boundary conditions indicated by the hyperelastic constitutive relation. Consider a scribe line initially parallel to the x_2-axis. When $e \equiv 1$, the material points on this scribe line become parallel to the x_1-axis for large γ. On the other hand, when the block is free to extend, $e \approx \gamma$ for large γ, and the scribe line approaches 45°. Hence, relative to the fixed height case, the unconstrained boundary conditions induce a counterclockwise rotation.

These results provide useful background for the model simulations described next and for our planned comparisons with the behaviour of the phenomenological theories presented in §4.

2. The polycrystal model

Crystal plasticity models explicitly represent deformation by crystallographic slip. In single crystal and polycrystalline metals with face-centered cubic (FCC) or body-centered cubic (BCC) structures, slip is the dominant mechanism of deformation over wide ranges of temperature and strain rate. One of the first quantitative analyses of the behaviour of FCC single crystals was made by Taylor (1938*a*, *b*). Taylor's model assumed rigid-plastic rate-independent deformation so that the choice of active slip systems was non-unique. Because at most five slip systems need to be active to accommodate an arbitrarily prescribed increment of deviatoric external strain, Taylor chose five (accommodating) increments of crystallographic slip such that the sum of their absolute values was minimized. However, as noted by Taylor (1938*a*), in many instances more than one such set of five shears could be chosen. The minimum shear principle of Bishop & Hill (1951*a*, *b*) contains Taylor's model as a specific case, and thus

problems of non-uniqueness arise here also. A more general framework describing the incremental rate independent elastic-plastic response of single crystals has been presented by Hill (1966). In this work, the uniqueness of rate-independent slip systems was shown to be inextricably linked to the crystal's hardening behaviour: given either the value of the Jaumann rate of Cauchy stress based on lattice spin or the value of the (external) rate of deformation, the slip system shear rates are uniquely determined if the crystal's hardening moduli are positive definite. Hence, positive definiteness of the hardening moduli is sufficient for the unique solution of mixed rate boundary value problems. Using a physically based kinematical model for crystallographic slip, Asaro & Rice (1977) have cast the (rather sparse) incremental framework of Hill in a more definite form. Although the main thrust of their paper is the relation of non-Schmid hardening descriptions to bifurcation phenomena, they also examined various measures of the resolved shear stress increment in some detail. Rice (1971) has shown how crystallographic slip (or continuum slip) models fit into his theory of finite strain elastic-plastic constitutive equations that use internal variables to characterize the current state of 'microstructural rearrangement'. More importantly, at least for our purposes, Asaro & Rice (1977) interpreted Lee's (1969) deformation gradient decomposition in a physically more meaningful way: the orientation of the intermediate configuration, i.e., that defined by $\boldsymbol{F}^{\mathrm{p}}$ below in equation (2.1), was taken to be determined solely by the kinematics of slip. This interpretation of the decomposition is pictured in figure 1 of Asaro & Rice (1977). Using this interpretation and a convenient (and correct) measure of the resolved shear stress increment, Asaro (1983*a*) and Peirce *et al.* (1982) recast the incremental forms of Asaro & Rice (1977) to give a rather general and computationally convenient rate-independent finite-strain elastic-plastic continuum slip description that was used to solve rate boundary value problems for the two-dimensional crystal model of Asaro (1979). Also, one should mention that a very general rate-independent finite-strain elastic-plastic crystallographic slip framework has been provided by Hill & Rice (1972), which was later elucidated by Hill & Havner (1982). As mentioned above, the solution of rate boundary value problems requires that the rate constitutive equation be invertible, i.e. that the choice of slip system shear increments be unique under both prescribed increments of stress and prescribed increments of strain. Peirce *et al.* (1982) found that for most (experimentally motivated) hardening descriptions, the rate constitutive equation became singular. This problem of non-uniqueness was later resolved by Peirce *et al.* (1983), where rate-dependent slip relations that guarantee invertibility were used. Additional discussion on this point has been given by Asaro (1983*a*, *b*).

An early extension of the theory of single crystal behaviour to that of polycrystalline response was made by Taylor (1938*a*, *b*). Using the slip minimization procedure described above, he calculated the response of a polycrystal under uniaxial extension with the assumption that each grain of the aggregate is subject to the same external or global increment of strain. He took his measure of macroscopic stress to be (most simply) the average of the stresses developed within each grain. The formulation of a polycrystal model should contain clear concepts of macroscopic stress and deformation measures: Hill (1972) has given a general treatment concerning the construction of these macrovariables for heterogeneous materials composed of homogeneous microconstituents under the conditions of finite strain. The use of Taylor-like assumptions in polycrystal models can be defended to some extent with Hill's constructions. The polycrystal model used for the finite shear simulations of §3 is the rate-dependent model of Asaro & Needleman (1985), which extends the single crystal framework used by Peirce

PHILOSOPHICAL TRANSACTIONS OF THE ROYAL SOCIETY A MATHEMATICAL, PHYSICAL & ENGINEERING SCIENCES

et al. (1983) via such Taylor-like assumptions. The rate-dependent formulation gives a unique specification of slip system shear rates, which gives unique predictions of lattice reorientations, and hence unique predictions of texture development.

2.1. *Constitutive behaviour of crystallites*

The mechanics of crystal deformation by slip is represented in two parts. The first part is a set of plastic simple shears from the reference configuration on the slip systems of the crystallite. Here, the material is envisioned to flow through the lattice via dislocation glide. Next, the lattice with its embedded material elastically deforms and rigidly rotates from this plastically sheared state to reach the current configuration. Hence, following Rice (1971) and Asaro & Rice (1977) (see their figure 1), the deformation gradient $\boldsymbol{F}$, introduced in the previous section, is decomposed as

$$\boldsymbol{F} = \boldsymbol{F}^{*} \cdot \boldsymbol{F}^{\mathrm{p}}. \tag{2.1}$$

In this decomposition, $\boldsymbol{F}^{\mathrm{p}}$ is the description of the material shear flow along the various slip systems of the crystallite, and $\boldsymbol{F}^{*}$ is the description of the elastic distortion of the lattice along with the rigid rotation of the crystallite. From (2.1) the spatial gradients of velocity are

$$\boldsymbol{L} = \dot{\boldsymbol{F}} \cdot \boldsymbol{F}^{-1} = \dot{\boldsymbol{F}}^{*} \cdot \boldsymbol{F}^{*-1} + \boldsymbol{F}^{*} \cdot \dot{\boldsymbol{F}}^{\mathrm{p}} \cdot \boldsymbol{F}^{\mathrm{p}-1} \cdot \boldsymbol{F}^{*-1}. \tag{2.2}$$

The plastic shear flow from the reference configuration is written as

$$\dot{\boldsymbol{F}}^{\mathrm{p}} \cdot \boldsymbol{F}^{\mathrm{p}-1} = \sum_{\alpha} \dot{\gamma}^{(\alpha)} \boldsymbol{s}^{(\alpha)} \boldsymbol{m}^{(\alpha)}, \tag{2.3}$$

where $\dot{\gamma}^{(\alpha)}$ is the shear rate on slip system α. The slip system α is defined by the unit crystallographic vectors $\boldsymbol{s}^{(\alpha)}$ and $\boldsymbol{m}^{(\alpha)}$, where $\boldsymbol{s}^{(\alpha)}$ is along the slip direction in the reference configuration, and $\boldsymbol{m}^{(\alpha)}$ is normal to the slip plane in the reference configuration. Hence, $\boldsymbol{s}^{(\alpha)}$ and $\boldsymbol{m}^{(\alpha)}$ are orthogonal. Here, the shear rate on each slip system is allowed to be positive or negative. With this convention, α ranges from 1 to 12 in equation (2.3) for an FCC crystallite. Hence,

$$\boldsymbol{F}^{*} \cdot \dot{\boldsymbol{F}}^{\mathrm{p}} \cdot \boldsymbol{F}^{\mathrm{p}-1} \cdot \boldsymbol{F}^{*-1} = \boldsymbol{D}^{\mathrm{p}} + \boldsymbol{W}^{\mathrm{p}} = \sum_{\alpha} \dot{\gamma}^{(\alpha)} \boldsymbol{s}^{*(\alpha)} \boldsymbol{m}^{*(\alpha)}, \tag{2.4}$$

where $\boldsymbol{s}^{*(\alpha)} = \boldsymbol{F}^{*} \cdot \boldsymbol{s}^{(\alpha)}$ convects with the lattice and $\boldsymbol{m}^{*(\alpha)} = \boldsymbol{m}^{(\alpha)} \cdot \boldsymbol{F}^{*-1}$ remains orthogonal to $\boldsymbol{s}^{*(\alpha)}$. Define the tensors

$$\boldsymbol{P}^{(\alpha)} = \mathrm{sym}\{\boldsymbol{s}^{*(\alpha)} \boldsymbol{m}^{*(\alpha)}\}, \quad \boldsymbol{W}^{(\alpha)} = \mathrm{skew}\{\boldsymbol{s}^{*(\alpha)} \boldsymbol{m}^{*(\alpha)}\}, \tag{2.5}$$

so that

$$\boldsymbol{D}^{\mathrm{p}} = \sum_{\alpha} \dot{\gamma}^{(\alpha)} \boldsymbol{P}^{(\alpha)}, \quad \boldsymbol{W}^{\mathrm{p}} = \sum_{\alpha} \dot{\gamma}^{(\alpha)} \boldsymbol{W}^{(\alpha)}. \tag{2.6}$$

Now, break $\dot{\boldsymbol{F}}^{*} \cdot \boldsymbol{F}^{*-1}$ into its symmetric part $\boldsymbol{D}^{*}$ and its skew-symmetric part $\boldsymbol{W}^{*}$ so that

$$\boldsymbol{D} = \boldsymbol{D}^{*} + \boldsymbol{D}^{\mathrm{p}}, \quad \boldsymbol{W} = \boldsymbol{W}^{*} + \boldsymbol{W}^{\mathrm{p}}, \tag{2.7}$$

where $\boldsymbol{D}$ and $\boldsymbol{W}$ are the symmetric and skew-symmetric parts of $\boldsymbol{L}$. Relations (2.7) give the natural additive decompositions afforded by (2.1). Note that $\boldsymbol{D}^{*}$ is the rate of deformation associated with lattice elasticity and $\boldsymbol{W}^{*}$ is the spin associated with lattice elasticity and rigid rotation of the crystallite, whereas $\boldsymbol{D}^{\mathrm{p}}$ and $\boldsymbol{W}^{\mathrm{p}}$ arise solely from the plastic slip. Note that this physically motivated model gives an explicit formula for the plastic spin $\boldsymbol{W}^{\mathrm{p}}$, which in most phenomenological models is assumed to vanish.

The plastic response of a crystallite is cast in terms of the resolved shear stress on each slip

system and the shear rate on each system. This is a simple extension of the well-known Schmid rule (for a critical resolved shear stress for yield) to the case of ongoing plastic flow. The rate of work per unit of volume in the reference configuration is

$$\boldsymbol{\tau}:\boldsymbol{D} = \boldsymbol{\tau}:\boldsymbol{D}^{*} + \boldsymbol{\tau}:\boldsymbol{D}^{\mathrm{p}} = \boldsymbol{\tau}:\boldsymbol{D}^{*} + \sum_{\alpha} \tau^{(\alpha)}\dot{\gamma}^{(\alpha)}, \tag{2.8}$$

where $\tau^{(\alpha)} = \boldsymbol{\tau}:\boldsymbol{P}^{(\alpha)} = \boldsymbol{m}^{*(\alpha)}\cdot\boldsymbol{\tau}\cdot\boldsymbol{s}^{*(\alpha)}$ is the resolved shear stress acting on the slip system α, and $\boldsymbol{\tau}$ is the Kirchhoff stress. Note that $\tau^{(\alpha)}$ is the proper work conjugate to the slip rate $\dot{\gamma}^{(\alpha)}$. The relation between the resolved shear stress and the slip rate is given by

$$\dot{\gamma}^{(\alpha)} = \dot{a}\,\mathrm{sgn}\{\tau^{(\alpha)}\}\{|\tau^{(\alpha)}/g^{(\alpha)}|\}^{1/m}, \tag{2.9}$$

where $\dot{a}$ is a reference shear rate (which is the same for all slip systems), $g^{(\alpha)}$ is the slip system hardness, m is the material rate sensitivity (which is also the same for all slip systems), and sgn ( ) means 'the sign of'. This viscoplastic power law has been used previously by Asaro & Needleman (1985). As $m \to 0$, rate-independent response is achieved. Note that each of the slip systems is active as long as the resolved shear stress on that system does not vanish. Hence, the constitutive description is free from various loading or unloading criteria. The hardness function $g^{(\alpha)}$ for multiple slip is constructed from the assumed single slip law

$$g(\gamma) = \tau_{\mathrm{o}} + h_{\mathrm{s}}\gamma + (\tau_{\mathrm{s}} - \tau_{\mathrm{o}})\tanh\left\{\left(\frac{h_{\mathrm{o}} - h_{\mathrm{s}}}{\tau_{\mathrm{s}} - \tau_{\mathrm{o}}}\right)\gamma\right\}, \tag{2.10}$$

where $g(\gamma)$ is the resolved shear stress on the slip system (when the shear rate is at its reference value $\dot{a}$), γ is the amount of shear (absolute value) on the system, τ_{o} is the initial (or critical) shear stress of the system, and h_{o} and h_{s} are the system's initial and asymptotic hardening rates. If $h_{\mathrm{s}} = 0$, then τ_{s} represents the asymptotic (or saturation) value of the shear stress. From (2.10), the single slip hardening rate is

$$h(\gamma) = h_{\mathrm{s}} + (h_{\mathrm{o}} - h_{\mathrm{s}})\,\mathrm{sech}^{2}\left\{\left(\frac{h_{\mathrm{o}} - h_{\mathrm{s}}}{\tau_{\mathrm{s}} - \tau_{\mathrm{o}}}\right)\gamma\right\}. \tag{2.11}$$

These single slip laws are generalizations of those used previously by Peirce *et al.* (1983) and Asaro & Needleman (1985) based on measurements of strain hardening of single crystals of aluminium alloys by Chang & Asaro (1981). For the present purposes, (2.11) provides a convenient relation for exploring the interaction between material strain hardening and texture development.

The generalization of these single slip equations to multiple slip is achieved by taking $g^{(\alpha)} = g^{(\alpha)}(\gamma_{\mathrm{a}})$, where γ_{a} is the accumulated sum of slips, i.e.

$$\gamma_{\mathrm{a}} = \int_{0}^{t} \sum_{\alpha} |\dot{\gamma}^{(\alpha)}|\,\mathrm{d}t. \tag{2.12}$$

For multiple slip, the evolution of the hardness is governed by

$$\dot{g}^{(\alpha)} = \sum_{\beta} h_{\alpha\beta}|\dot{\gamma}^{(\beta)}|, \tag{2.13}$$

where $g^{(\alpha)}(0) = \tau_{\mathrm{o}}$, and where $h_{\alpha\beta}$ are the hardening moduli. The form of the moduli is

$$h_{\alpha\beta} = h(\gamma_{a})\,q_{\alpha\beta}, \tag{2.14}$$

where $h(\gamma_a)$ is the single-slip relation (2.11), and $q_{\alpha\beta}$ is the matrix describing the latent hardening behaviour of the crystallite. The form of $q_{\alpha\beta}$ is motivated by the body of experimental studies reported in the literature (see Kocks (1970) for a discussion), and by the overshoot calculations by Asaro (1983*a*) and Peirce *et al.* (1982). For FCC crystallites possessing 12 slip systems of the type {111}⟨110⟩, we have taken the simple form

$$q_{\alpha\beta} = \begin{pmatrix} A & qA & qA & qA \\ & A & qA & qA \\ & & A & qA \\ \text{sym} & & & A \end{pmatrix}, \tag{2.15}$$

where q is the ratio of the latent hardening rate to the self hardening rate, and A is a 3×3 matrix fully populated by ones. In (2.15), the numbering of the slip systems is such that systems 1, 2 and 3 are co-planar; as are 4, 5 and 6; 7, 8 and 9; and 10, 11 and 12. Hence, the ratio of the latent hardening rate to the self hardening rate for coplanar systems is taken as unity, in reasonable accordance with experiment. The form of the hardening description as given by equations (2.13), (2.14), and (2.15) has been used previously by Asaro & Needleman (1985).

The elastic response of the crystallite is governed by the form

$$\overset{\nabla}{\boldsymbol{\tau}}{}^{*} = \boldsymbol{L}:\boldsymbol{D}^{*}, \tag{2.16}$$

where $\overset{\nabla}{\boldsymbol{\tau}}{}^{*}$ is the Jaumann rate of Kirchhoff stress based on the lattice spin $\boldsymbol{W}^{*}$, i.e.

$$\overset{\nabla}{\boldsymbol{\tau}}{}^{*} = \dot{\boldsymbol{\tau}} - \boldsymbol{W}^{*}\cdot\boldsymbol{\tau} - \boldsymbol{\tau}\cdot\boldsymbol{W}^{*T}. \tag{2.17}$$

To define $\boldsymbol{L}$, let $\boldsymbol{a}_i$ be the (orthonormal cartesian) base vectors of the reference crystal configuration and let $\boldsymbol{a}_i^{*}$ be the covariant (or convected) base vectors associated with lattice motion, i.e.

$$\boldsymbol{a}_i^{*} = \boldsymbol{F}^{*}\cdot\boldsymbol{a}_i. \tag{2.18}$$

The vectors $\boldsymbol{a}_i$ are taken to be aligned with the axes of the undeformed cubic crystal. the elastic moduli $\boldsymbol{L}$ are then given by

$$\boldsymbol{L} = L^{ijkl}\boldsymbol{a}_i^{*}\boldsymbol{a}_j^{*}\boldsymbol{a}_k^{*}\boldsymbol{a}_l^{*}, \tag{2.19}$$

where the elastic stiffnesses L^{ijkl} are consistent with linear elasticity. As discussed by Asaro & Needleman (1985), the relation (2.16) may be viewed as an approximation to hyperelastic response if the magnitude of the elastic stiffnesses is large compared to that of the stress components. The relation between the Jaumann rate $\overset{\nabla}{\boldsymbol{\tau}}{}^{*}$ based on $\boldsymbol{W}^{*}$ and the conventional Jaumann rate $\overset{\nabla}{\boldsymbol{\tau}}$ based on the total spin $\boldsymbol{W}$ is

$$\overset{\nabla}{\boldsymbol{\tau}}{}^{*} = \overset{\nabla}{\boldsymbol{\tau}} + \sum_{\alpha}\dot{\gamma}^{(\alpha)}\boldsymbol{\beta}^{(\alpha)}, \tag{2.20}$$

where

$$\boldsymbol{\beta}^{(\alpha)} = \boldsymbol{W}^{(\alpha)}\cdot\boldsymbol{\tau} - \boldsymbol{\tau}\cdot\boldsymbol{W}^{(\alpha)}. \tag{2.21}$$

Combine (2.6), (2.7), (2.16), and (2.20) to find the governing rate form

$$\overset{\nabla}{\boldsymbol{\tau}} = \boldsymbol{L}:\boldsymbol{D} - \sum_{\alpha} \dot{\gamma}^{(\alpha)} \boldsymbol{R}^{(\alpha)}, \tag{2.22}$$

where

$$\boldsymbol{R}^{(\alpha)} = \boldsymbol{L}:\boldsymbol{P}^{(\alpha)} + \boldsymbol{\beta}^{(\alpha)}. \tag{2.23}$$

Looking ahead, it is most convenient to write (2.22) in the form

$$\dot{\boldsymbol{n}} = \boldsymbol{K}:\dot{\boldsymbol{F}} - \dot{\boldsymbol{B}}, \tag{2.24}$$

where $\dot{\boldsymbol{n}}$ is the rate of nominal stress, $\boldsymbol{n} = \boldsymbol{F}^{-1}\cdot\boldsymbol{\tau}$. As described in Asaro & Needleman (1985), the rate tangent modulus method of Peirce *et al.* (1983) is used for the numerical implementation of (2.24).

2.2. *Homogeneous deformation of aggregates under shear loading*

Given the constitutive behaviour of single crystallites, the constitutive response of a polycrystalline aggregate is sought. Here, each grain of the aggregate is assumed to be identical in terms of constitutive response. In the spirit of Taylor's model (1938*a*, *b*), the aggregate is subject to a uniform deformation and continuity among the various crystallites (or grains) is enforced by requiring that each is subject to the same (global) homogeneous deformation. Contrary to Taylor's model (where each component of the deformation gradient is prescribed), the present model incorporates the homogeneous (shearing) deformations into rate boundary value problems involving the average nominal stress rate $\dot{\bar{\boldsymbol{n}}}$ and the global deformation gradient rate $\dot{\bar{\boldsymbol{F}}}$. Superposed bars are used to indicate average quantities, while quantities dealing with the kth crystallite are indicated by a superscripted k. The average nominal stress is given by

$$\bar{\boldsymbol{n}} = \frac{1}{V}\sum_{k=1}^{N}\int_{V^{(k)}} \boldsymbol{n}^{(k)}\,\mathrm{d}V^{(k)} \tag{2.25}$$

whose rate is

$$\dot{\bar{\boldsymbol{n}}} = \frac{1}{V}\sum_{k=1}^{N}\int_{V^{(k)}} \dot{\boldsymbol{n}}^{(k)}\,\mathrm{d}V^{(k)}, \tag{2.26}$$

where

$$V = \sum_{k=1}^{N} V^{(k)}. \tag{2.27}$$

Here, $V^{(k)}$ is the reference volume of the kth crystallite, $\boldsymbol{n}^{(k)}$ ($\dot{\boldsymbol{n}}^{(k)}$) is the nominal stress (rate) in that crystallite, and N is the number of grains that make up the polycrystal. In terms of the model, (2.26) is written more simply as

$$\dot{\bar{\boldsymbol{n}}} = \frac{1}{N}\sum_{k=1}^{N} \dot{\boldsymbol{n}}^{(k)} \tag{2.28}$$

because the stress state in each grain is homogeneous and each grain is taken to have the same (arbitrary) volume. Note that the average Kirchhoff stress is

$$\bar{\boldsymbol{\tau}} = \bar{\boldsymbol{F}}\cdot\bar{\boldsymbol{n}} \tag{2.29}$$

because $\boldsymbol{\tau}^{(k)} = \boldsymbol{F}^{(k)}\cdot\boldsymbol{n}^{(k)} = \bar{\boldsymbol{F}}\cdot\boldsymbol{n}^{(k)}$. In the same manner, the average of (2.24) is

$$\dot{\bar{\boldsymbol{n}}} = \bar{\boldsymbol{K}}:\dot{\bar{\boldsymbol{F}}} - \dot{\bar{\boldsymbol{B}}}, \tag{2.30}$$

where $$\bar{\boldsymbol{K}} = \frac{1}{N}\sum_{k=1}^{N} \boldsymbol{K}^{(k)}, \quad \dot{\bar{\boldsymbol{B}}} = \frac{1}{N}\sum_{k=1}^{N} \dot{\boldsymbol{B}}^{(k)}. \tag{2.31}$$

For an aggregate that is subject to velocity boundary conditions that correspond to the deformation gradient rate $\dot{\bar{\boldsymbol{F}}}$, Hill (1972) has shown that $\bar{\boldsymbol{n}}$ as given by (2.25) is indeed the proper work conjugate to $\dot{\bar{\boldsymbol{F}}}$ (as long as continuity and equilibrium are satisfied throughout the aggregate), and hence $\bar{\boldsymbol{n}}$ is a proper measure of global stress. Within the context of the model, each grain is homogeneously stressed so that equilibrium is not satisfied at the grain boundaries, but nevertheless, $\bar{\boldsymbol{n}}$ is taken as the measure of global stress. This assumption is the basis of the averaging procedure, and it is inherent in any type of Taylor model. A more thorough discussion of the averaging is given in Asaro & Needleman (1985).

We consider an aggregate of grains subject to boundary constraints consistent with uniform deformations of a homogeneous medium. The boundary conditions are expressed in terms of the deformation gradient, $\boldsymbol{F}$ and the unsymmetric nominal stress, $\boldsymbol{n}$. The deformation gradient is defined as $\boldsymbol{F} = \partial\bar{\boldsymbol{x}}/\partial\boldsymbol{x}$, where $\bar{\boldsymbol{x}}$ denotes the current position, relative to a fixed cartesian frame of a material particle initially at $\boldsymbol{x}$. The unsymmetric nominal stress, $\boldsymbol{n}$, is related to the force transmitted across a material element by $\mathrm{d}\boldsymbol{P} = \boldsymbol{v}\cdot\boldsymbol{n}\cdot\mathrm{d}S$, where $\boldsymbol{v}$ and $\mathrm{d}S$ are the orientation and area of the material element in the reference configuration, respectively, and $\boldsymbol{T} = \boldsymbol{v}\cdot\boldsymbol{n}$ is termed the traction vector. An overall homogeneous simple shearing deformation is specified in terms of various combinations of prescribed average nominal stress rate and aggregate deformation gradient rate. In each case the plane of shearing is the x_1–x_2 plane and, to examine the importance of boundary constraints, four rate boundary value problems are examined. Each is cast so as to constrain any rigid-body rotation. Common to all are the conditions

$$\dot{\bar{n}}^{33} = \dot{\bar{n}}^{31} = \dot{\bar{n}}^{32} = 0, \quad \dot{\bar{F}}_{21} = \dot{\bar{F}}_{31} = 0, \quad \dot{\bar{F}}_{32} = 0, \quad \dot{\bar{F}}_{12} = \dot{\gamma}, \tag{2.32}$$

where $\dot{\gamma}$ is the prescribed shear rate.

The first relation in (2.32) expresses the requirement that the out-of-plane traction vector vanishes. The second relation in (2.32) requires a line of material particles along the shearing direction (the x_1 axis) to remain along that axis, whereas the third relation in (2.32) constrains the rotation of material points initially along the x_2 axis. Alternatives to (2.32) could have been employed; for example, the rotation of planes parallel to the plane of shearing (the x_1–x_2 plane) could be constrained, with $\dot{\bar{F}}_{13} = \dot{\bar{F}}_{23} = 0$ prescribed rather than $\dot{\bar{n}}^{31} = \dot{\bar{n}}^{32} = 0$. For classical isotropic (or orthotropic) phenomenological constitutive relations, such as considered in §1 here, these various out-of-plane boundary conditions are equivalent. Nevertheless, because the polycrystalline aggregate is not exactly orthotropic, the constraint combinations must be chosen with some care to avoid overconstraining the aggregate; for example, if the kinematic constraints preclude any volume change, the elastic compressibility induces a large hydrostatic stress. With (2.32), the numerical results show that the quantity work conjugate to the one constrained remains small; for example, $|\bar{F}_{13}|/\lambda$ and $|\bar{F}_{23}|/\lambda$, where λ is the maximum principal stretch, are of the order of 10^{-2} or smaller. This indicates that prescribing the work conjugate quantities would not significantly affect the results. By way of contrast, the various in-plane constraints considered here do affect the overall response.

For the first problem, the boundary conditions supplementing (2.32) are

$$\dot{\bar{F}}_{11} = \dot{\bar{F}}_{22} = 0; \tag{2.33}$$

PHILOSOPHICAL TRANSACTIONS OF THE ROYAL SOCIETY A MATHEMATICAL, PHYSICAL & ENGINEERING SCIENCES

for the second problem, the remaining conditions are

$$\dot{\bar{n}}_{22} = 0, \quad \dot{\bar{F}}_{11} = 0; \tag{2.34}$$

for the third problem, they are

$$\dot{\bar{\tau}}_{11} = (\bar{F}_{11}\bar{n}_{11} + \bar{F}_{12}n_{21})^{\cdot} = 0, \quad \dot{\bar{F}}_{22} = 0; \tag{2.35}$$

and finally for the fourth problem, they are

$$\dot{\bar{n}}_{22} = 0, \quad \dot{\bar{\tau}}_{11} = (\bar{F}_{11}\bar{n}_{11} + \bar{F}_{12}\bar{n}_{21})^{\cdot} = 0. \tag{2.36}$$

The initial conditions for each of these rate problems correspond to zero stress and deformation.

Although each of the above sets of boundary conditions refers to a state of homogeneous deformation, each is meant to model various aspects of finite-strain torsion experiments. A torsion specimen (rod or tube) is usually described in terms of circular polar coordinates r, θ, and z. In the above boundary condition sets, the $\boldsymbol{e}_1$-direction may be construed to be the circumferential (or θ) direction; the $\boldsymbol{e}_2$-direction, the axial (or z) direction; and the $\boldsymbol{e}_3$-direction, the radial (or r) direction. In each of the sets, any face with normal $\pm\boldsymbol{e}_3$ is traction free, which would correspond to a traction-free lateral surface on a torsion specimen. With these allusions to torsion in mind, the first rate boundary value problem will subsequently be referred to as 'fully constrained torsion', because here the hoop and axial components of normal strain are prescribed zero while the hoop and axial components of normal (Kirchhoff) stress are allowed to develop. This is analogous to torsion of a solid rod with fixed ends, or more precisely, torsion of a thin-walled tube with a rigid internal mandrel and fixed ends. The second problem will be referred to as 'torsion with mandrel', because the hoop component of normal strain is prescribed zero while the hoop component of normal stress is allowed to develop. Also, axial strains are allowed to develop. The third problem will be referred to as 'torsion with end constraint', because the axial normal strain is set to zero while the axial normal stress is allowed to vary. Also, hoop strains are allowed to develop as they would in a thin-walled tube without a mandrel. Finally, the fourth rate boundary value problem will be referred to as 'unconstrained torsion', because all three normal stress components are made to be zero while all three normal strains may develop. It is worth reiterating that, in all four of the above boundary condition sets, the shear strain components $\bar{F}_{13}$ and $\bar{F}_{23}$ are allowed to accumulate. If these two shear strains become too large in magnitude, then a reasonable description of torsion will no longer be had, but for aggregates that remain nearly orthotropic, these two (undesirable) shear components will be small. As noted above, our numerical results show this to be true.

The rate boundary value problems (2.32)–(2.36) are designed to model the response of polycrystals that are initially free from any kind of stress or deformation, i.e. the aggregates are thought of as being in the fully annealed condition at the start of the torsion test. In the experiments done by Montheillet *et al.* (1984) this is indeed the case, but Williams (1962), on the other hand, performed his finite shear experiments on as-received rolled plate stock. Even though the as-received stock is globally free from stress ($\bar{\boldsymbol{n}} = 0$), it has residual stresses ($\boldsymbol{n}^{(k)} \neq 0$) present from previous working. In fact, Williams presents pole figures that show

the initial rolling texture of his stock. To quantify this situation, the deformation gradient will be written as

$$\bar{F} = \bar{F}_a \cdot \bar{F}_o, \tag{2.37}$$

where $\bar{F}_o$ is the (global) deformation gradient that measures the residual deformation of the as-received state with respect to the virgin (or fully annealed) state, and where $\bar{F}_a$ is the (global) deformation gradient that measures the deformation of the current (sheared) state with respect to the as-received state. The stress measure $\bar{n}_a$ that is conjugate to $\dot{\bar{F}}_a$ is found by looking at the total work rate, i.e.

$$\int_V \bar{n} : \dot{\bar{F}} \, dV = \int_{V_a} \bar{n}_a : \dot{\bar{F}}_a \, dV_a, \tag{2.38}$$

where dV is an element of material volume in the virgin state and dV_a is that element of material volume in the as-received state. Hence,

$$\bar{n}_a = \frac{1}{J_o} \bar{F}_o \cdot \bar{n}, \tag{2.39}$$

where $J_o = \det \bar{F}_o$. The rate boundary value problems that model finite torsion of as-received material are then obtained from (2.32)–(2.36) by replacing $\dot{\bar{n}}$ with $\dot{\bar{n}}_a$ and $\dot{\bar{F}}$ with $\dot{\bar{F}}_a$. The initial conditions are then $\bar{n} = 0$ and $\bar{F} = \bar{F}_o$.

2.3. *Initial grain distributions and model parameters*

To solve the above rate boundary value problems for a polycrystalline material, the virgin aggregate itself must first be defined. This is done by specifying a group of orthogonal transformations that give the orientations of the crystallites' reference axes with respect to the laboratory axes, i.e.

$$a_i^{(k)} = \psi_{ij}^{(k)} e_j, \tag{2.40}$$

where k ranges from 1 to the number of crystallites in the aggregate. Two different initial grain distributions have been used for the calculations presented here: one contains 489 grains; the other, 300 grains. Both are meant to be approximations of an initially isotropic aggregate.

Orientations of crystallites that make up an aggregate are measured via X-ray diffraction, and traditionally the data generated are presented in terms of pole figures and inverse pole figures. In accordance with most of the literature dealing with FCC polycrystalline shear, the pole figures presented in this paper are exclusively e_3 stereographic projections of $\langle 111 \rangle$ crystallographic directions. In these figures, the laboratory shear direction e_1 is labelled as x_1, and the shear plane normal e_2 is labelled as x_2. The direction e_3 will also be referred to as x_3. The inverse pole figures presented in this paper are [100] stereographic projections of either the x_1-direction or the x_2-direction. The direction indices of the resulting inverse pole points are arranged so that they fall within the [100], [110], [111] standard triangle.

The distribution with 489 grains is generated in a manner similar to that used by Asaro & Needleman (1985). First, a regular array of 55 points is plotted on the standard triangle so that it is uniformly covered. Each of these points is taken as an inverse pole point of the x_2-axis. The grain corresponding to the first of these points is chosen so that the x_2-axis corresponds to the [100] crystal direction; the x_1-axis, the [001] direction. Each of the remaining 54 points correspond to three grains. For the first of the three grains, the x_1-axis is given a random orientation in the plane normal to the x_2-axis. The next two grains are obtained by $+120°$ and $-120°$ rotations about the x_2-axis from the first. In this manner 163 grains are generated. Now,

the inverse pole figures of the x_1, x_2 and x_3-axes of this distribution of 163 grains are all different, but for isotropic material, all three of these should be the same. Persuant, two more grains are generated from each of the first 163 grains in such a way so as to yield three identical inverse pole figures. Hence, this distribution consists of 489 grains.

The distribution with 300 grains is generated in somewhat of a simpler manner. As above, this set actually consists of 100 grains, from each of which is derived two more grains so that the three inverse pole figures are identical. Each of the original 100 grains is generated by choosing a random x_3-direction that lies within the standard triangle, and then by choosing the x_2-axis to have a random orientation in the plane normal to the x_3-axis. A fairly uniform coverage of orientations is obtained for both initial grain distributions as shown in the resulting pole figures in figure 3.

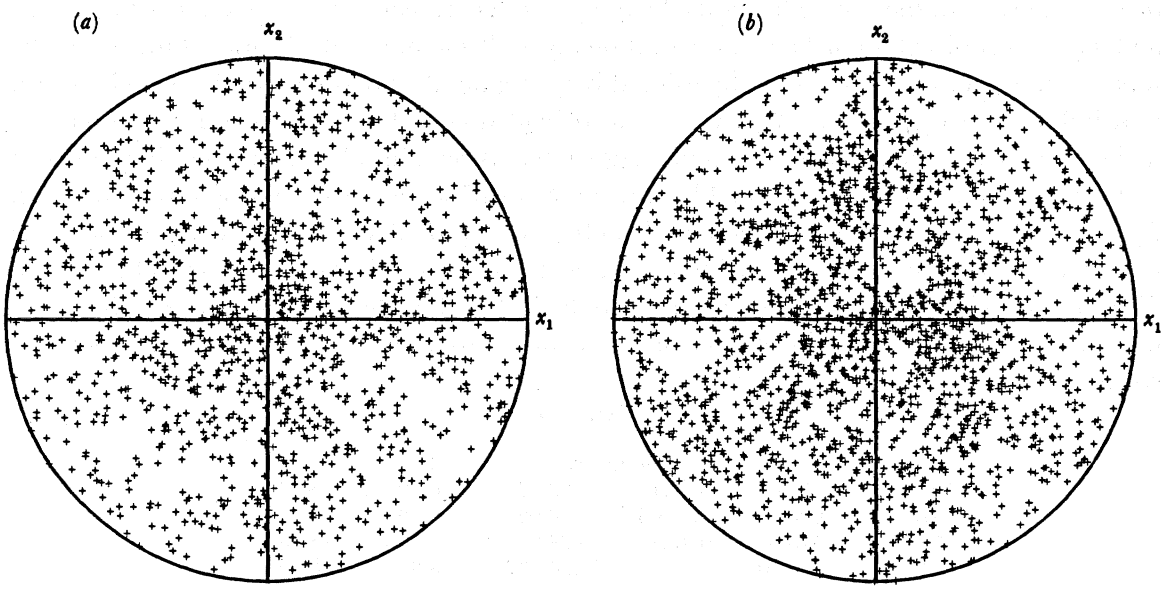

FIGURE 3. Initial grain orientation distributions for (*a*) 300 grains and (*b*) 489 grains represented by {111} stereographic pole figures. The axes x_1 and x_2 correspond to those shown in figure 1.

In the virgin state, $\bar{K}$ in (2.30) has the needed information to form the initial elasticity tensor $\bar{L}^o$ for an aggregate. The $\bar{L}^o$ provides a measure of an aggregate's degree of isotropy. On the laboratory axes, $\bar{L}^o$ in matrix form is

$$\bar{L}^o = \begin{Bmatrix} \bar{L}^o_{1111} & \bar{L}^o_{1122} & \bar{L}^o_{1133} & \bar{L}^o_{1112} & \bar{L}^o_{1113} & \bar{L}^o_{1123} \\ & \bar{L}^o_{2222} & \bar{L}^o_{2233} & \bar{L}^o_{2212} & \bar{L}^o_{2213} & \bar{L}^o_{2223} \\ & & \bar{L}^o_{3333} & \bar{L}^o_{3312} & \bar{L}^o_{3313} & \bar{L}^o_{3323} \\ & & & \bar{L}^o_{1212} & \bar{L}^o_{1213} & \bar{L}^o_{1223} \\ & & & & \bar{L}^o_{1313} & \bar{L}^o_{1323} \\ \text{sym} & & & & & \bar{L}^o_{2323} \end{Bmatrix}. \tag{2.41}$$

For an isotropic polycrystal one would have

$$\left.\begin{aligned} \bar{L}^{o}_{1111} = \bar{L}^{o}_{2222} = \bar{L}^{o}_{3333} = \lambda + 2\mu, \quad \bar{L}^{o}_{1122} = \bar{L}^{o}_{1133} = \bar{L}^{o}_{2233} = \lambda, \\ \bar{L}^{o}_{1212} = \bar{L}^{o}_{1313} = \bar{L}^{o}_{2323} = \mu, \end{aligned}\right\} \tag{2.42}$$

with the other components being zero, and where λ and μ are the usual elastic constants. The crystal elasticity is governed by

$$C_{11} = 842\tau_o, \quad C_{12} = 607\tau_o, \quad C_{44} = 377\tau_o, \tag{2.43}$$

where τ_o is as in §2.1, and where C_{11}, C_{12} and C_{44} are the usual cubic elasticities. These constants represent the anisotropy of copper crystals. In table 1, the initial elasticity tensors $\bar{\boldsymbol{L}}^{o} \div \tau_o$ are presented in matrix form for three different grain distributions. The distribution with 196 grains was used previously by Asaro & Needleman (1985) for uniaxial and plane-strain deformations, with the x_2-axis being the loading axis. As evidenced by the values of $\bar{L}^{o}_{2212}$, $\bar{L}^{o}_{2213}$ and $\bar{L}^{o}_{2223}$, this distribution behaves exceptionally well for uniaxial histories. But, when the torsion simulations were first tried by using this aggregate, the non-orthotropic behaviour, e.g. that induced by $\bar{L}^{o}_{1112} = 0.10\bar{L}^{o}_{1212}$, was deemed inadequate. The other two distributions are designed to give a more nearly isotropic aggregate. As seen in table 1, the distribution with 489 grains satisfies the relations (2.42), but there is still some non-orthotropic response, e.g. $\bar{L}^{o}_{1112} = 0.033\bar{L}^{o}_{1212}$. The distribution with 300 grains provides a more nearly orthotropic material, e.g. $\bar{L}^{o}_{2212} = -0.0014\bar{L}^{o}_{1212}$, but this is at the expense of relations (2.42). Other grain distributions with more than 1000 grains were looked at, but the improvement obtained was not substantial enough to justify the increase in computational time that one would be required.

TABLE 1

196 grains

1043.8	510.06	502.15	28.26	0.00	8.83
510.06	1035.9	510.06	0.00	0.00	0.00
502.15	510.06	1043.8	−28.26	0.00	−8.83
28.26	0.00	−28.26	280.06	8.83	0.00
0.00	0.00	0.00	8.83	272.15	−28.26
8.83	0.00	−8.83	0.00	−28.26	280.06

489 grains

1049.6	503.20	503.20	9.04	−3.64	−5.40
503.20	1049.6	503.20	−3.64	−5.40	9.04
503.20	503.20	1049.6	−5.40	9.04	−3.64
9.04	−3.64	−5.40	273.20	−5.40	−5.40
−3.64	−5.40	9.04	−5.40	273.20	−5.40
−5.40	9.04	−3.64	−5.40	−5.40	273.20

300 grains

1076.7	489.66	489.66	0.25	−0.37	0.12
489.66	1076.7	489.66	−0.37	0.12	0.25
489.66	489.66	1076.7	0.12	0.25	−0.37
0.25	−0.37	0.12	259.66	0.12	0.12
−0.37	0.12	0.25	0.12	259.66	0.12
0.12	0.25	−0.37	0.12	0.12	259.66

In addition to two grain distributions, various hardening and strain-rate sensitivity properties have been used in the calculations. Two different single-slip hardening descriptions have been employed; cf. (2.10). The first, designated by $h_s = 0.0$, corresponds to the constants

$\tau_s = 1.8\tau_o$, $h_o = 8.9\tau_o$ and $h_s = 0$; the second, designated by $h_s = 0.1$, corresponds to $\tau_s = 1.89\tau_o$, $h_o = 8.9\tau_o$ and $h_s = 0.1\tau_o$. Note that when $h_s = 0$, hardening quickly saturates so that slip system hardening essentially vanishes when γ (in single slip) is larger than *ca.* 0.1. Thus, the influences of texture on polycrystal strain hardening are more readily apparent in this case than for $h_s = 0.1\tau_o$. Two values of the ratio of latent-hardening rate to self-hardening rate, cf. (2.15), have been used: these are $q = 1.0$ and $q = 1.4$. The value $q = 1.0$ corresponds to Taylor's isotropic hardening whereas $q = 1.4$ is taken to be an upper limit, at larger strains, of the strong latent hardening observed in lower stacking fault energy materials (see, for example, Asaro 1983*a* and Kocks 1970). We have observed that the effects of latent hardening are continuous in the range $q = 1.0$–1.4 and so these two values provide a relatively complete description of the influence of latent hardening specialized, of course, to the present simplification of constant q and the matrix form of equation (2.15). The reference shear rate $\dot{a}$ of (2.9) is given by the material time constant $\tau_o \div (C_{11}\dot{a}) = 1.19$, and the global shear rate $\dot{\gamma}$ of (2.32) has been set to $\dot{\gamma} = \dot{a}$. Finally, various values of the material rate sensitivity m, cf. (2.9), have been employed: $m = 0.005$, $m = 0.02$, $m = 0.05$, $m = 0.2$ and $m = 0.5$. The latter two values are used to explore some rather interesting effects of viscous behaviour in the power law region of $0.1 \leqslant m < 1$.

2.4. *Ideal shearing textures*

Before examining the numerical calculations of §3, it is helpful to look at some simple results that pertain to pole figure geometry and ideal textures of FCC polycrystal subject to shear. For convenience, attention is confined to rigid-plastic behaviour so that the covariant lattice base vectors $\boldsymbol{a}_i^*$, cf. (2.18), form an orthonormal triad.

The first of these results follows from the ideas of van Houtte & Aernoudt (1976), and deals with equivalent orientations of crystallites with respect to the applied mode of deformation. For the shear problems at hand, it is sufficient to consider spatial velocity gradients of the form

$$\boldsymbol{L} = L_{11}\,\boldsymbol{e}_1\boldsymbol{e}_1 + L_{22}\,\boldsymbol{e}_2\boldsymbol{e}_2 + L_{33}\,\boldsymbol{e}_3\boldsymbol{e}_3 + L_{12}\,\boldsymbol{e}_1\boldsymbol{e}_2. \tag{2.44}$$

Now, consider two differently oriented grains and write

$$\boldsymbol{L} = L_{ij}^{(1)}\,\boldsymbol{a}_i^{*(1)}\,\boldsymbol{a}_j^{*(1)} = L_{ij}^{(2)}\,\boldsymbol{a}_i^{*(2)}\,\boldsymbol{a}_j^{*(2)}. \tag{2.45}$$

It is a simple matter to see that

$$L_{ij}^{(1)} = L_{ij}^{(2)} \tag{2.46}$$

if the orientation of the second grain is obtained by rotating that of the first 180° about the x_3-axis. Next, consider an arbitrary crystallographic direction $[hkl]$ through two grains oriented in this manner: it is easily shown that the [001] stereographically projected pole point of the first grain's $[hkl]$ direction is centrosymmetric to that of the second grain's $[hkl]$ direction. In view of equation (2.46), both grains feel the same spatial gradients of velocity with respect to their crystal axes, and thus, both will continue to be related by equation (2.46) as the indicated deformation mode proceeds. Hence, the pole points of these two grains will remain centrosymmetric. The above results are true regardless of the crystal class involved. Obviously, an initial grain distribution does not consist of pairs of grains oriented in this manner, but these results do suggest that any texturing that occurs will be characterized by pole figures that exhibit global (as opposed to point by point) centrosymmetry.

Various workers (Montheillet *et al.* 1984, 1985; Canova *et al.* 1984) have classified the

texture components that form when FCC polycrystals are subject to shear. Both Canova *et al.* (1984) and Montheillet *et al.* (1984) use the notation $\{hkl\}\langle uvw\rangle$ to describe ideal texture components, i.e. crystallite orientations that may undergo shear without lattice rotation. Here, the crystallographic planes $\{hkl\}$ correspond to the shear plane, i.e. to the x_1–x_3 plane, and the $\langle uvw\rangle$ directions correspond to the direction of shear, i.e. to the x_1-direction. Whereas Canova *et al.* (1984) describe these textures in terms of ranges of orientations (fibres), Montheillet *et al.* (1984) use specific, discrete orientations.

As introduced earlier, past experimental works, as well as past and present computational works, suggest that two basic fibre textures form. The first, the A-fibre, consists of orientations whereby the $\langle 111\rangle$ crystal directions align with the global shear plane normal x_2. This fibre is represented by the orthogonal transformation

$$\boldsymbol{a}_i^* = A_{ij}\boldsymbol{e}_j, \tag{2.47}$$

where

$$\left.\begin{array}{lll} A_{11}=-2b & A_{12}=\dfrac{1}{\sqrt{3}} & A_{13}=-2d \\ A_{21}=-a+b & A_{22}=\dfrac{1}{\sqrt{3}} & A_{23}=c+d \\ A_{31}=a+b & A_{32}=\dfrac{1}{\sqrt{3}} & A_{33}=-c+d, \end{array}\right\} \tag{2.48}$$

and where

$$a=\frac{1}{\sqrt{2}}\cos\alpha, \quad b=\frac{1}{\sqrt{6}}\sin\alpha, \quad c=\frac{1}{\sqrt{2}}\sin\alpha, \quad d=\frac{1}{\sqrt{6}}\cos\alpha. \tag{2.49}$$

The axis of this transformation is the $\boldsymbol{e}_2$-axis, and α measures the angular position of the A-fibre crystallites about this axis. The symmetry operation for this fibre is a 120° rotation about the $\boldsymbol{e}_2$-axis. For convenience, label the $\langle 111\rangle$ crystal directions as follows: $[111], 1$; $[\bar{1}11], 2$; $[1\bar{1}1], 3$; and $[11\bar{1}], 4$. Also, introduce the notation $I(X)$, where I is one of these four directions, and where X is the value of α in degrees. With these conventions, the upper-left figure of figure 4 shows the pole figure generated by transformation (2.47) for $-60° \leqslant \alpha \leqslant 60°$, where the plane of the pole figure is described by the cartesian coordinate system (y_1, y_2). If the bounding circle is taken as $y_1^2+y_2^2=4$, then the two net lines shown in the figure are circular arcs of radius $4\sqrt{2}$ centred at $(y_1, y_2)=(0, \pm 6)$. The top (bottom) net line corresponds to the locus of pole points 70.529° from the $\boldsymbol{e}_2(-\boldsymbol{e}_2)$-axis. On most of the pole figures that present the calculations of §3, bands are drawn whose centres correspond to the above net lines. The partial A_1-fibre of Canova *et al.* (1984) is denoted by $\{111\}\langle uvw\rangle$ and corresponds to $-60° \leqslant \alpha \leqslant 0°$. The A-type orientations of Montheillet *et al.* (1984) are given by $\alpha=\pm 60°$ for $\{1\bar{1}1\}\langle 110\rangle$; $\alpha=0°$ for $\{\bar{1}11\}\langle\bar{1}10\rangle$; $\alpha=30°$ for $\{\bar{1}\bar{1}1\}\langle 112\rangle$; and $\alpha=-30°$ for $\{11\bar{1}\}\langle 112\rangle$. Note that the texture designation $\{hkl\}\langle uvw\rangle$ of Montheillet *et al.* (1984) has been taken to mean the single component $(hkl)\,[uvw]$, and under this interpretation, the upper left-hand pole figure in figure 8 of Montheillet *et al.* (1984) has been incorrectly plotted: if one exchanges the upward-pointing triangle symbol for the downward-pointing triangle symbol and vice versa, then the figure is correct. The texture components given by $\alpha=\pm 60°$ and $\alpha=0°$ are single-slip configurations and symmetric double-slip configurations are given by $\alpha=\pm 30°$. As will be shown in §3, the behaviour of the components $-60° \leqslant \alpha \leqslant 0°$ differs from that of the components $0° \leqslant \alpha \leqslant 60°$, and for this reason, the A-fibre classification is split into two partial

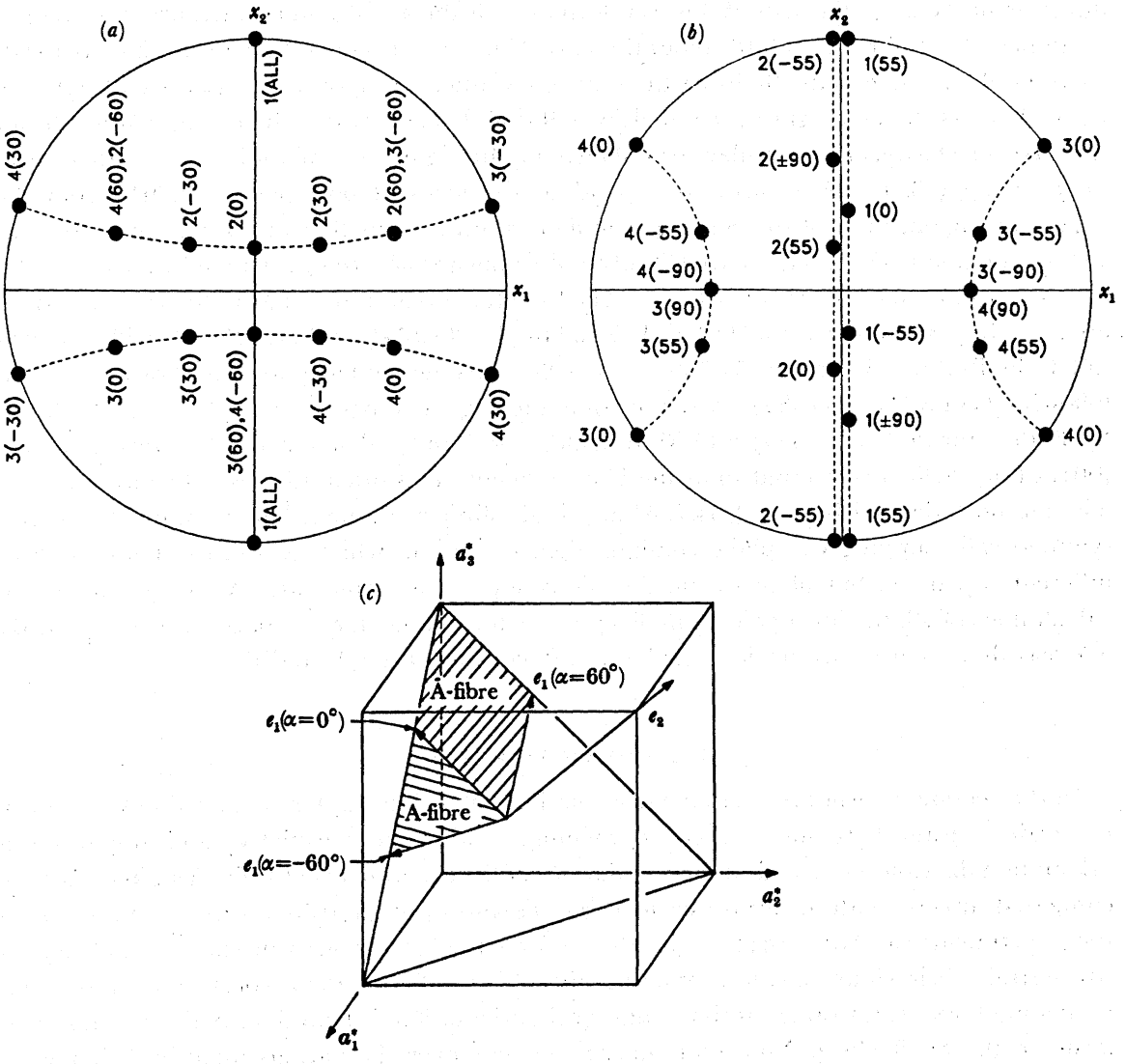

FIGURE 4. The {111} stereographic projections depict the ideal fibre textures (*a*) A and (*b*) B, as explained in the text. The A_f (A-fibre) and $\bar{A}_f$ ($\bar{A}$-fibre) orientation ranges are indicated in (*c*) with respect to the deformed crystal lattice base vectors a_1^*, a_2^*, and a_3^*.

fibres: A_f given by $-60° \leqslant \alpha \leqslant 0°$, and $\bar{A}_f$ given by $0° \leqslant \alpha \leqslant 60°$. The lower figure of figure 4 depicts the range of slip directions e_1 that make up these two fibres. The B-fibre of orientations is the second class of textures that develop under shear, and it is represented by the orthogonal transformation

$$a_i^* = B_{ij}\, e_j, \tag{2.50}$$

where

$$\left.\begin{aligned} B_{11} &= 0 & B_{12} &= \cos\beta & B_{13} &= -\sin\beta \\ B_{21} &= -\frac{1}{\sqrt{2}} & B_{22} &= \frac{1}{\sqrt{2}}\sin\beta & B_{23} &= \frac{1}{\sqrt{2}}\cos\beta \\ B_{31} &= -\frac{1}{\sqrt{2}} & B_{32} &= \frac{1}{\sqrt{2}}\sin\beta & B_{33} &= \frac{1}{\sqrt{2}}\cos\beta. \end{aligned}\right\} \tag{2.51}$$

This class consists of ideal components whose $\langle 110 \rangle$ crystal directions align with the global direction of shear x_1. The axis of this transformation is the $\boldsymbol{e}_1$-axis, and β measures the angular position of the B-fibre crystallites about this axis. The symmetry operation for this fibre is a 180° rotation about the $\boldsymbol{e}_1$-axis. By using the same conventions as above, the upper-right figure of figure 4 shows the pole figure generated by $-90° \leqslant \beta \leqslant 90°$, where the line $y_1 = 0$ is split for the sake of clarity. The circular arcs shown in the figure are of radius $\sqrt{2}$ with centres $(y_1, y_2) = (\pm\sqrt{6}, 0)$. These arcs correspond to the locus of pole points 35.264° from the $\pm\boldsymbol{e}_1$-axes. Again, most of the ensuing pole figures have bands that demarcate these arcs (as well as the line $y_1 = 0$). The partial B_f-fibre of Canova *et al.* (1984), denoted by $\{hkl\}\langle 110 \rangle$, corresponds to $-54.736° \leqslant \beta \leqslant 54.736°$. The B-texture orientations of Montheillet *et al.* (1984) are given by $\beta = -35.264°$ for $\{\bar{1}12\}\langle 110 \rangle$ and by $\beta = 35.264°$ for $\{1\bar{1}2\}\bar{1}10\rangle$. As will be shown in §3, the B-fibre orientations $54.736° < |\beta| \leqslant 90°$ have no tendency to form. For this reason, following Canova *et al.* (1984), we denote only the angular range $-54.736° \leqslant \beta \leqslant 54.736°$ as B_f. Both Canova *et al.* (1984) and Montheillet *et al.* (1984) define a third texture type, i.e. $\{001\}\langle 110 \rangle$, which is referred to as the C-component. This orientation is defined by $\beta = 0°$. The positions defined by $\beta = \pm 54.736°$ are single-slip orientations. The position $\beta = 0°$ is a symmetrically slipping two-plane configuration, i.e. one in which two slip systems (each of different slip plane but of the same direction) slip at the same rate. As suggested by the calculations of §3, the ideal pole figure for positive torsion, i.e. for $\dot{\gamma} > 0$, consists of A_f and B_f, whereas that for negative torsion, i.e. for $\dot{\gamma} < 0$, consists of the $\bar{A}_f$ and B_f.

3. Numerical results

In this section we will first examine deformation textures to explore the effects of boundary constraint, strain hardening, latent hardening, strain-state sensitivity, and initial grain orientation distribution. In addition, simulations of the experiments of Williams (1962) will be compared directly with his measured textures. Textures produced by reverse straining (as in the experiments of Swift (1947)) will also be presented. Next we will examine polycrystal stress–strain behaviour, again examining the effects of boundary constraint, slip-system hardening laws, strain-rate sensitivity, and grain orientation distribution. A third section will focus on the Swift effect. Note that superposed bars over the various quantities that were previously used to indicate average values over the aggregate are subsequently dropped, i.e. $\bar{\boldsymbol{\tau}}$ will be denoted by $\boldsymbol{\tau}$ and $\bar{\boldsymbol{F}}$ will be denoted by $\boldsymbol{F}$, etc.

3.1. *Shear textures*

Experimental measurements of shear textures have been briefly reviewed in §1.1. As already noted, our primary representations of texture are stereographic {111} pole figures although some examples of inverse pole figures are also given. The two initial grain distributions were shown earlier in figure 3.

The qualitative features of texture evolution can be seen in figure 5*a–d*. This calculation for 'fully constrained' shear of the '489' grain aggregate shows the rotation of individual grains into nearly ideal texture orientations. Movement of poles into ideal textures is evident in figure 5*a* even at a (global) shear of $\gamma = 0.562$. Sharp A_f and B_f textures form within a shear strain of 3. We note here, and discuss later, that the predicted textures are more intense than are observed in X-ray diffraction measurements of pole figures. Also note in figure 5*b* that the

poles moving into ideal orientations appear to be rotated slightly, as an aggregate, in the direction opposite to the shear direction (counterclockwise about the x_3-direction) before they sharpen into the ideal fibre textures. As this occurs the apparent global rotation of the pole figure disappears. These qualitative features of rapid formation of texture and slight 'ideal texture rotations' are characteristic of all of the calculations except those for high strain rate sensitivities.

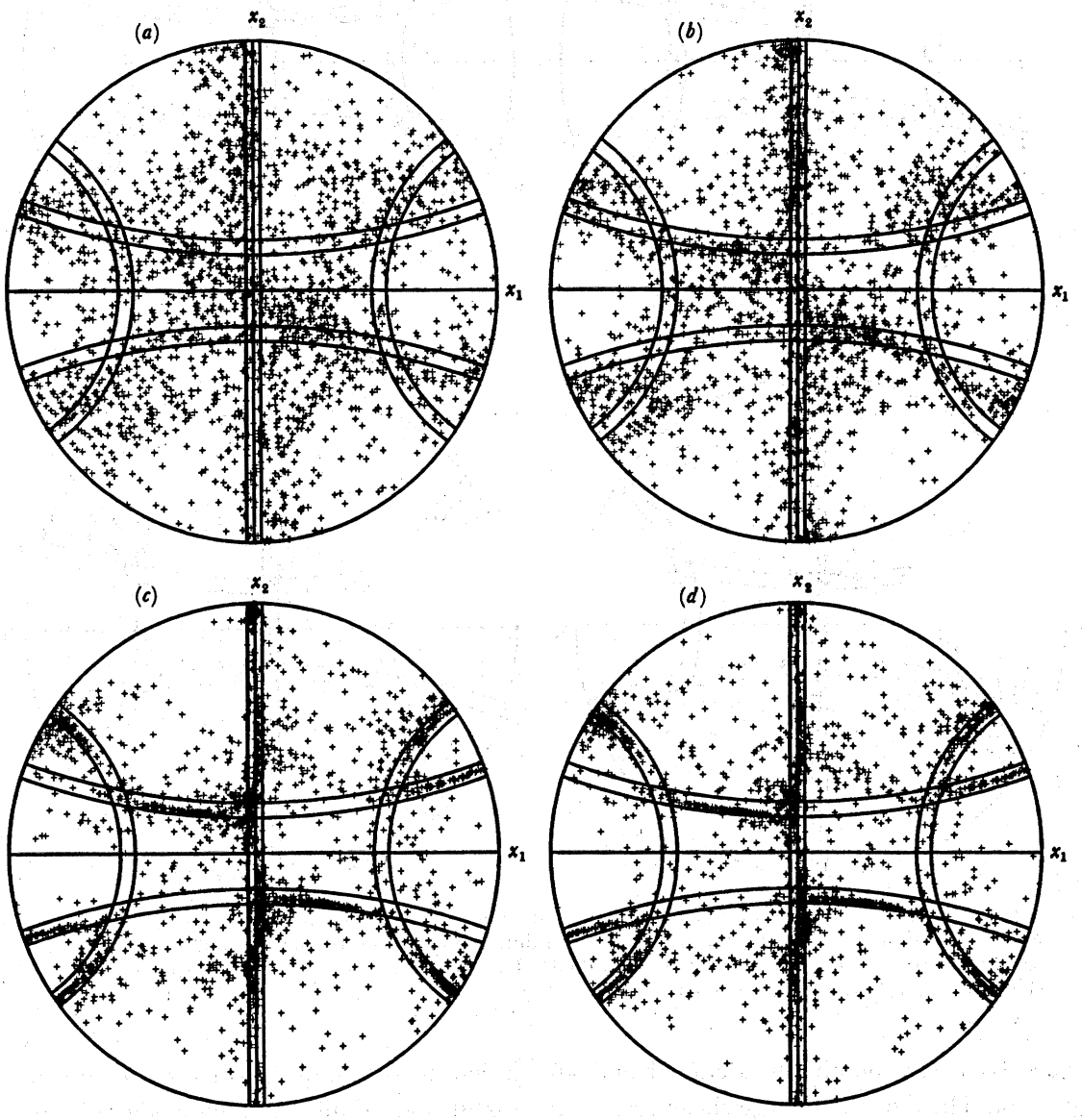

FIGURE 5. Pole figures for four strain levels (*a*) $\gamma = 0.562$, (*b*) $\gamma = 1.16$, (*c*) $\gamma = 3.16$, and (*d*) $\gamma = 3.56$ for the case of 'fully constrained' shear with material parameters $h_s = 0.0$, $q = 1.0$ and $m = 0.005$. The '489' grain distribution was used. Note the 'bands' whose centres correspond to the ideal textures plotted in figure 4. These bands also appear in subsequent pole figures.

The effects of boundary constraint upon the shear texture are nominal, except for the 'unconstrained' case. Textures calculated for the '300' grain orientation distribution after a shear of 3.60 are shown for each of the four sets of boundary conditions in figure 6*a–d*. The 'fully constrained,' 'torsion with mandrel,' and 'torsion with end constraint' textures

PHILOSOPHICAL TRANSACTIONS OF THE ROYAL SOCIETY A MATHEMATICAL, PHYSICAL & ENGINEERING SCIENCES

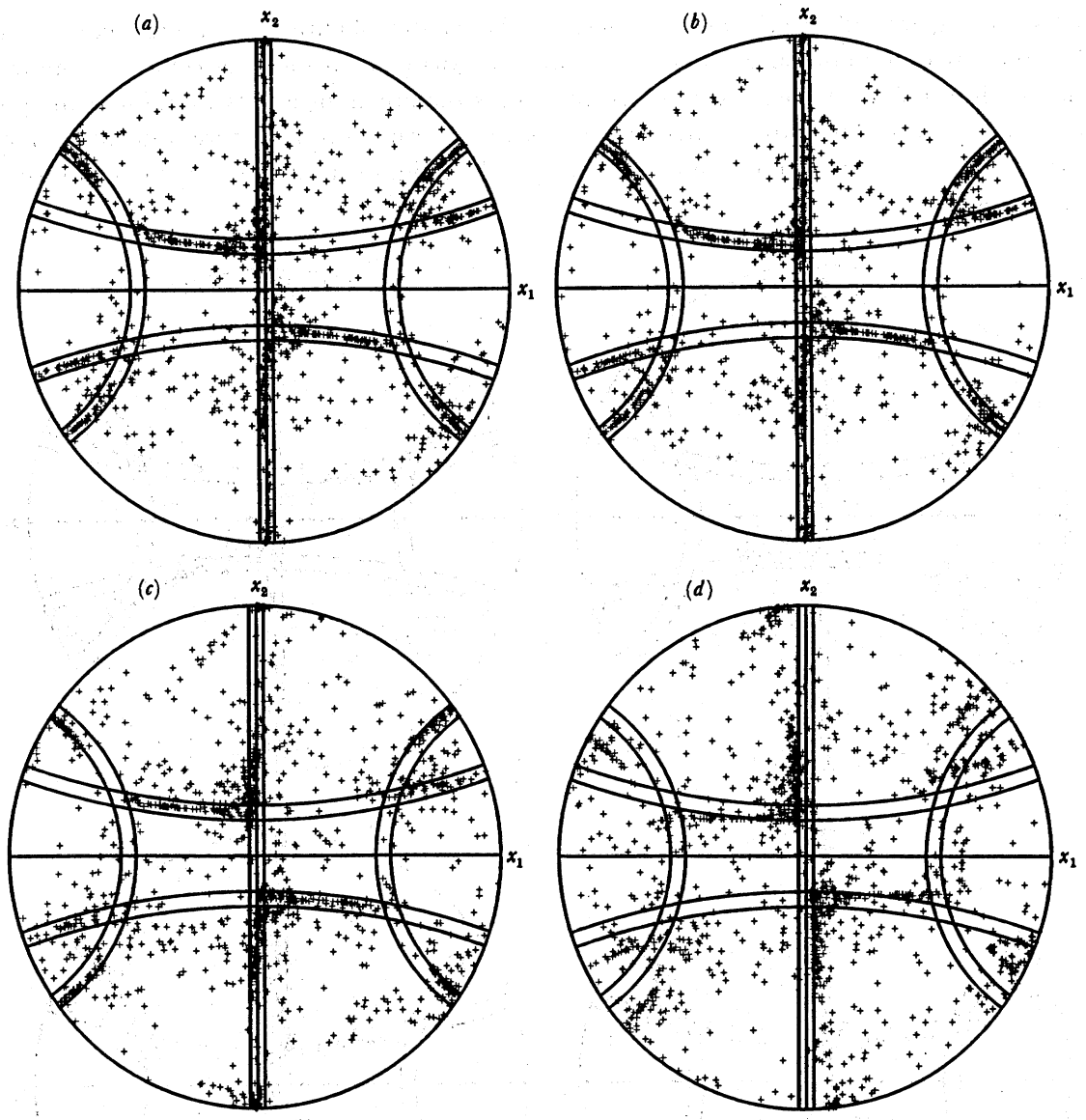

FIGURE 6. Pole figures at a shear strain of $\gamma = 3.60$ for the four sets of constraints: (*a*) fully constrained torsion, (*b*) torsion with mandrel, (*c*) torsion with end constraint, and (*d*) unconstrained torsion. Material parameters for all four cases are $h_s = 0.0$, $q = 1.0$ and $m = 0.005$. The use of the label 'torsion' is meant to be suggestive. The '300' grain distribution was used.

(figure 6*a–c*) are nominally identical and are similar to the '489' grain texture shown in figure 5*d*. Thus for these large shear strains, the textures are similar so long as there is either axial or hoop constraint. In addition, the slight differences between the '300' and '489' initial grain orientation distributions do not appear to affect the predicted textures. However, we will see later that the differences between the two distributions noticeably affect the constitutive response. The 'unconstrained' case differs from the others in that the entire pole figure is rotated *ca.* 7° counterclockwise (opposite to the direction of shear) about the x_3-axis. This rotation can also be viewed by comparing inverse pole figures computed along the shearing direction and the shear plane normal for the 'fully constrained' case (figure 7*a*) and

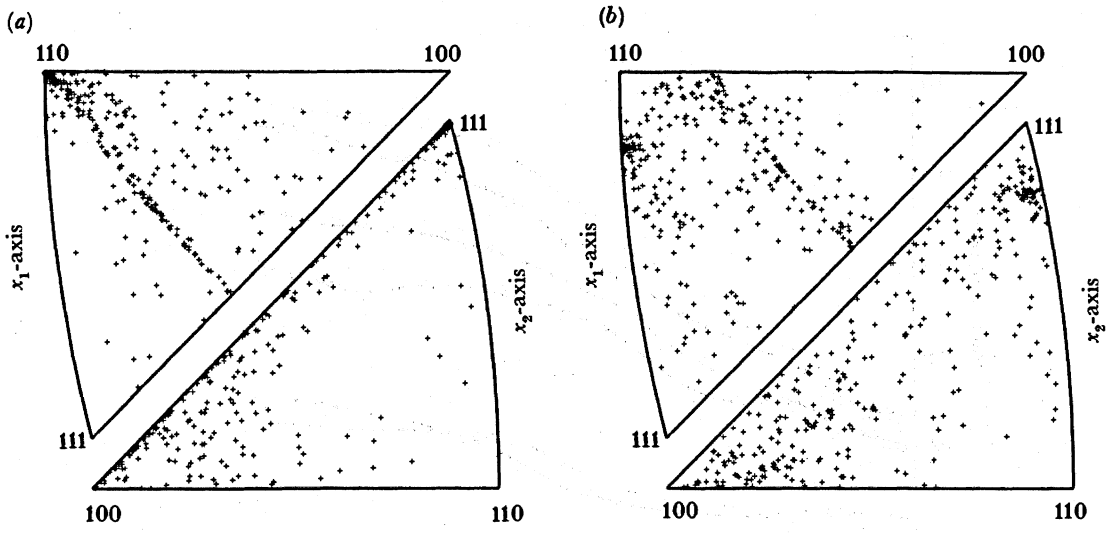

FIGURE 7. Stereographic inverse pole figures corresponding to the cases represented by (*a*) fully constrained torsion as in figure 6*a* and (*b*) unconstrained torsion as in figure 6*b*.

'unconstrained case' (figure 7*b*). The rotation of the A-fibre is evident as the motion of x_2-axis (z-axis) poles away from the {111} crystallographic plane normal. Similarly the rotation of the B-fibre is evident in the x_1 inverse pole figure as the motion of x_1 poles away from the ⟨110⟩ direction. The sense of this rotation is known to depend on the direction of shear, i.e. shearing in the negative x_1-direction would induce an opposite rotation. As will be explained in §4, the kinematics of deformation are also quite different for the 'unconstrained' specimen and this, along with the difference in stress state, accounts for the difference in texture.

The effects of strain hardening and strain-rate sensitivity on texture are not readily apparent in pole figures, especially for $\gamma < 4$. Quantitative means are needed to distinguish the trends. For this purpose, the fractions of the total number of poles having each ideal texture orientation were computed as a function of shear strain. A pole was said to belong to an ideal texture if it was within 3° of an ideal orientation. Note that the A-fibre in these calculations includes both partial fibres, A_f and $\bar{A}_f$. Texture evolution for four combinations of work hardening h_s and latent hardening ratio q is shown for 'fully constrained' shear in figure 8. For all four cases the B-fibre evolves most rapidly and is predominant. The intensity of the A-fibre also increases continuously, but at a slightly lower rate. The C-texture component does not begin to increase until $\gamma \approx 2$.

Slip-system 'self' hardening *per se* (i.e. $h_s = 0.0$ against $h_s = 0.1$) does not substantially influence texture evolution, regardless of latent hardening. However, latent hardening does have noticeable qualitative effects. For example, higher levels of latent hardening result in stronger A_f and B_f textures. Latent hardening also causes the C-texture to begin evolving at smaller strains. Strain-rate sensitivity also appears to have only minor effects upon texture evolution for $\gamma < 4$. However, if texture evolution is computed up to very large strains, e.g. $\gamma = 30$, one sees definite trends as shown in figure 9. Here we find for $m = 0.005$–0.05 that texture evolves similarly up to $\gamma = 9$, but that the three ideal texture components are sharper for lower strain rate sensitivities. Beyond $\gamma \approx 9$, it appears that the texture components each undergo different transients whose 'strain scale' depends upon strain-rate sensitivity. The

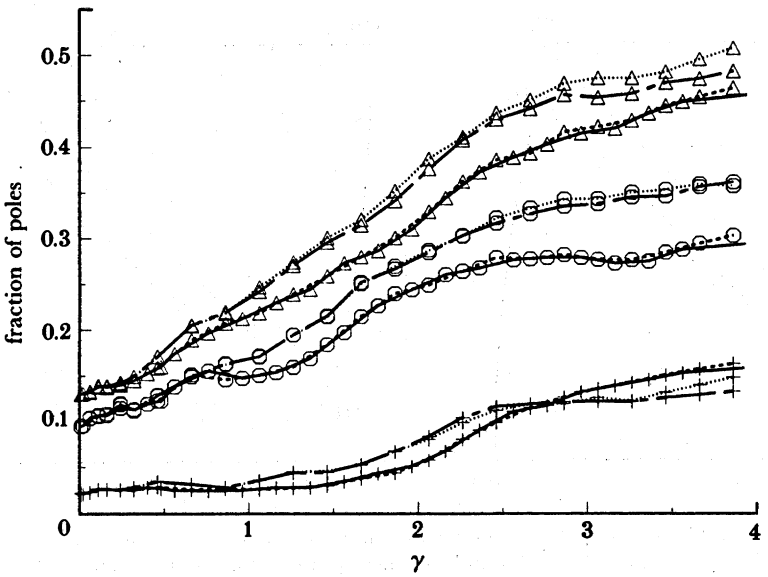

FIGURE 8. Fractions of grains (i.e. poles) within the three ideal textures A fibre (○), B fibre (△), and C (+) as a function of strain. Four cases illustrating the influence of strain hardening and latent hardening on texture development are shown: $h_s = 0.0$, $q = 1.0$ (——); $h_s = 0.1$, $q = 1.0$ (– – – –); $h_s = 0.1$, $q = 1.4$ (· · · ·); and $h_s = 0.0$, $q = 1.4$ (—·—). In all cases $m = 0.005$ and the '489' grain distribution was used.

transients are most rapid for higher rate sensitivities. For example, the C-texture increases abruptly at $\gamma \approx 10$ for $m = 0.05$, at $\gamma \approx 12$ for $m = 0.02$, and at $\gamma \approx 15$ for $m = 0.005$. The rate of increase in the C-texture intensity is more pronounced for higher rate sensitivities. Similar transients of the A-fibre texture begin at the same respective strain levels, e.g. the intensity decreases at $\gamma \approx 9$ for $m = 0.05$, $\gamma \approx 11$ for $m = 0.02$, and $\gamma \approx 14$ for $m = 0.005$. Turning attention to higher strain levels, the B-fibre also begins to decrease in intensity at $\gamma \approx 25$ for $m = 0.05$. Presumably the number of B poles would decrease at strains larger than 33 for $m = 0.02$ and $m = 0.005$. There is concern whether calculations at such large strains are meaningful because the grain shape is highly distorted and no effects of grain shape are accounted for in the present model. However, by calculating textures for $\gamma > 10$ we have been able to see an effect of strain-rate sensitivity that is not apparent for $\gamma < 10$. Later we show how these very large strain calculations provide an interpretation of Swift-effect measurements at elevated temperatures. We also note here that the motion picture films of Lowe & Asaro (1985) indicate that a significant number of poles move into orientations within the $\bar{A}_f$ partial fibre in the strain range just before the A-fibre exhibits its abrupt drop in intensity. This development of $\bar{A}_f$ poles seems to be the dominant cause, e.g. for $m = 0.05$, of the observed increase in the A-fibre intensity in the range $5.0 \gtrsim \gamma \gtrsim 7.5$. Perhaps also this $\bar{A}_f$ development has a role in precipitating the abrupt drop in the A-fibre intensity.

Our computed textures are compared with textures measured by Williams (1962) in copper plates in figure 10. Williams's tests were carried out in shear, rather than in torsion, and his pole figures are among the most complete. Also, his copper plate was pretextured by a 20% reduction in thickness during rolling. Williams's starting texture is shown in figure 10*a* by his plotted contours of X-ray intensity along with our computed texture for the '489' grain distribution subjected to a plane strain compression of the same amount. In the {111} pole

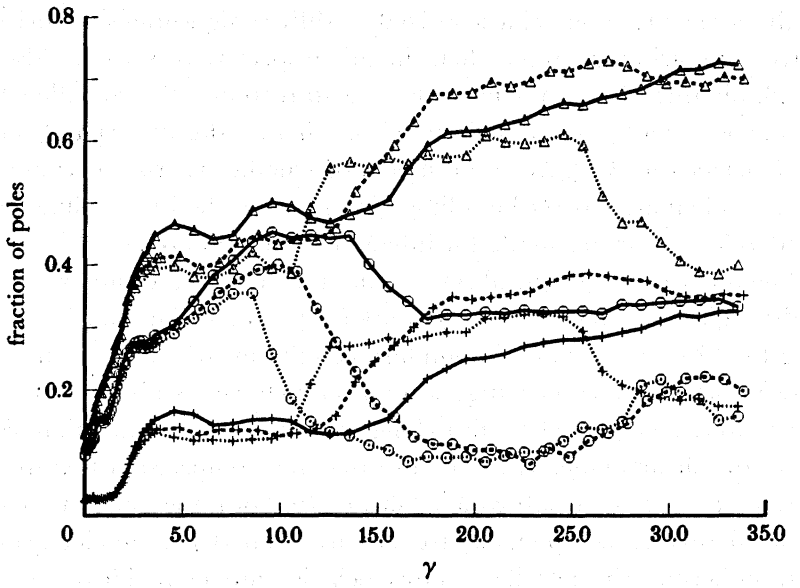

FIGURE 9. Fractions of grains (i.e. poles) within the three ideal textures A fibre (○), B fibre (△), and C (+) as a function of strain for various strain rate sensitivities: $m = 0.005$ (——), $m = 0.02$ (– – – –), and $m = 0.05$ (· · · ·). The common material parameters are $h_s = 0.0$, $q = 1.0$, and the '489' grain distribution.

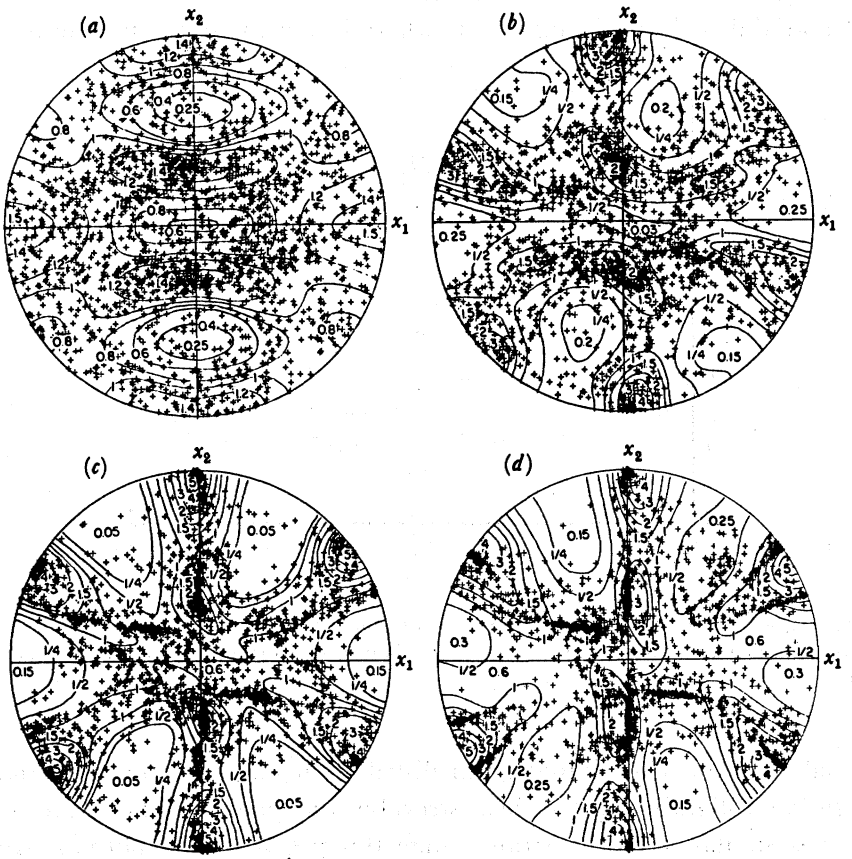

FIGURE 10. Initial and shear textures at various strains as predicted (shown by +) and as measured by Williams (1962) on prerolled copper plates (shown by solid contour lines). (*a*) shows the initial texture predicted by subjecting an initially isotropic aggregate to plane strain compression of 23%. The '489' grain distribution was used with material parameters $h_s = 0.0$, $q = 1.0$ and $m = 0.005$. (*b*), (*c*) and (*d*) show the measured and computed textures after the pretextured aggregate has been subjected to 'fully constrained' shear to $\gamma = 0.54$, 1.44, and 3.25, respectively.

figures shown, both these textures are characterized by diffuse high-intensity horizontal bands, and the qualitative comparison between them in this respect is very close. Also notice that Williams's data exhibit intensity peaks near the $\pm x_1$-directions (the so-called brass rolling texture) whereas our predictions do not. It is not clear whether this discrepancy arises because of some inherent deficiency in the polycrystal model or whether it arises because plane strain compression does not adequately describe rolling. In any case, the brass rolling component is quickly annihilated at low shear strains. As the imposed shear strain is increased a shear texture similar to those shown earlier develops, although the influence of the pretexture is felt up to strains of at least the highest strain shown in figure 10, i.e. $\gamma = 3.25$. This particular comparison was done by using the 'fully constrained' boundary conditions, which were chosen under the assumption that in Williams's tests the gauge sections (which were stubby key ways machined into the rolled plate) were constrained against elongating either in the direction of shear or the direction normal to the shear plane. We note also that the compression textures are plotted against the x_1, x_2 and x_3-axes of subsequent shear. In both the measurements and the calculations, the ideal texture components are slightly rotated counterclockwise about the x_3-axis; as the textures become sharper they rotate clockwise into nearly ideal orientations. This rotation is most readily seen by the rotation of the A-fibre intensity peak along the pole figure circumference near the x_2-direction.

Looking ahead to the next section, the shear stress–strain behaviour calculated for this pretextured material is shown in figure 11, where it is compared with the behaviour of the

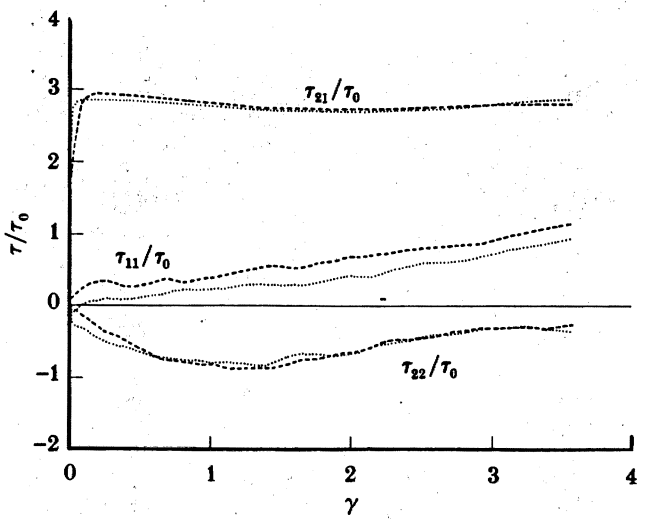

FIGURE 11. Shear stress–strain curves for the initially isotropic grain orientation distribution (----) and for the distribution obtained after 23% compression (····). The grain distributions and material parameters are as in figure 10.

virgin material with the same initial grain distribution and the same material parameters. Yielding begins at a slightly reduced shear stress but the qualitative behaviour of the curve of τ_{12} against γ is similar over the strain range $0 \leqslant \gamma \leqslant 3.6$. The normal stresses are also qualitatively similar except for the τ_{11} component which is initially *negative*. At strains larger than about $\gamma \approx 0.10$ the only substantial difference is that normal stress component τ_{11} is approximately 25% less for the prerolled material. These results show an interesting

dependence of the phenomenology of normal stress development on initial textures that are only slight departures from isotropic.

Another comparison of this type is shown in figure 12. The experimental pole figure, again taken from Williams (1962), was obtained by first subjecting the specimen to a shear strain of $\gamma = -1.38$ (i.e. in the negative x_1-direction) and then reversing the sense of shear until a strain of $\gamma = 1.70$ was achieved. The qualitative comparison between the computed and measured textures is again very good and it is interesting to note that the influence of the pretexture formed by shearing in the $-x_1$-direction is, as observed by Williams (1962), mostly lost by reverse straining. The texture after reverse straining is indeed sharply defined by the strain of $\gamma = 1.70$. The A_f bands expected during shear in the positive x_1-direction are evident in the measurements and predictions, along with the remnants of the $\bar{A}_f$ texture formed during the initial negative shear.

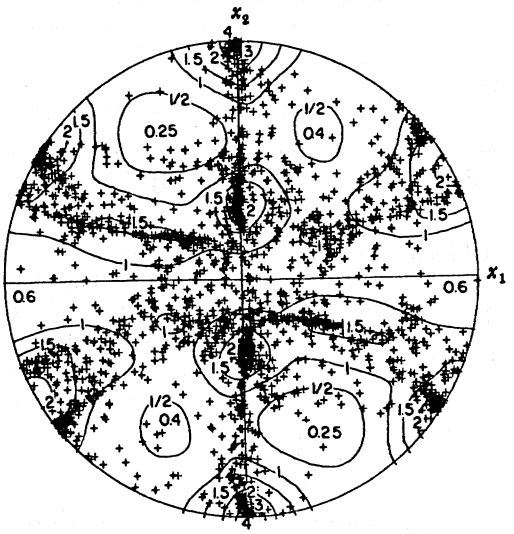

FIGURE 12. The {111} pole figure for the case of reversed straining from $\gamma = -1.38$ to $\gamma = 1.70$ corresponding to the experimental test of Williams (1962). Williams's experimental results are shown by the solid contour lines. The initial grain distribution, boundary conditions, and material parameters are as in figures 10 and 11.

3.2. *Polycrystal stress–strain behaviour*

We now examine in detail the deformation, i.e. constitutive, responses calculated along with the textures shown previously. However, it is first useful to examine the response of special grain orientations corresponding to the ideal textures described in §2.4. This exercise helps correlate the predictions of deformation response with those of texture evolution.

3.2.1. *Deformation response of ideally oriented polycrystals*

The deformation responses are calculated for polycrystals, each having 31 grains whose orientations are uniformly distributed entirely within one of the texture fibres A_f, $\bar{A}_f$, or B_f. Also, calculations were made by combining two of the fibre distributions, with each fibre distribution being constructed from 21 grains uniformly distributed about the angles α and β defined in §2.4, yielding a polycrystal with 42 grains. The response of a single grain having a C-texture orientation is also calculated. These results are shown for 'fully constrained' and 'unconstrained' boundary conditions in figures 13 and 14, respectively. Looking first at the 'fully constrained' calculation in figure 13, one notes that for all grain orientation distributions

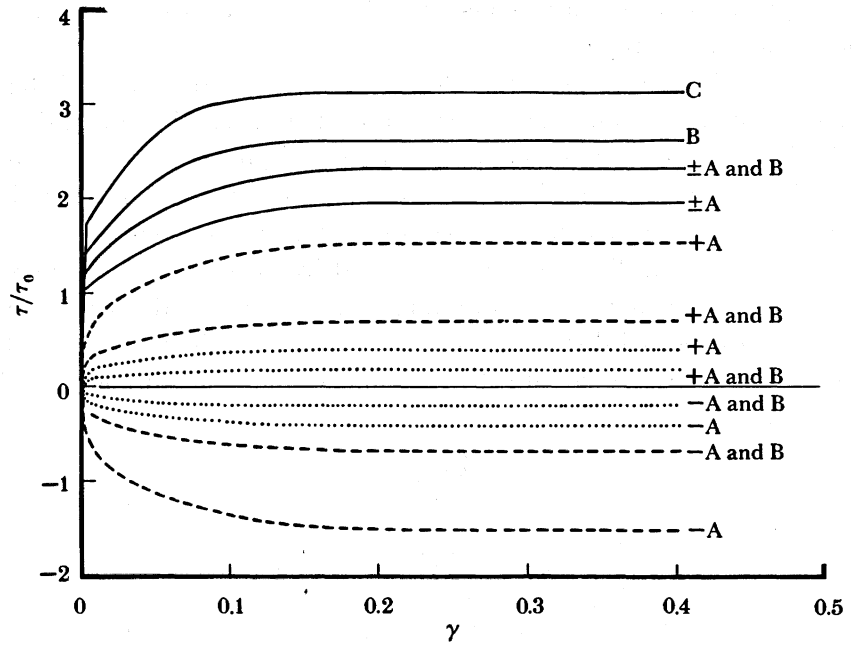

FIGURE 13. Behaviour of stress–strain components τ_{21}/τ_0(——), τ_{11}/τ_0(– – – –), and τ_{22}/τ_0(· · · ·) for the ideal textures acting individually or in combination under 'fully constrained' boundary constraints. The +A stands for A_f whereas −A stands for $\bar{A}_f$; ±A means A_f or $\bar{A}_f$. Also, B stands for B_f. Note that the B_f and C ideal textures produce no normal stress on the shear plane whereas A_f produces a tensile stress. The material parameters used are $h_s = 0.0$, $q = 1.0$, and $m = 0.005$.

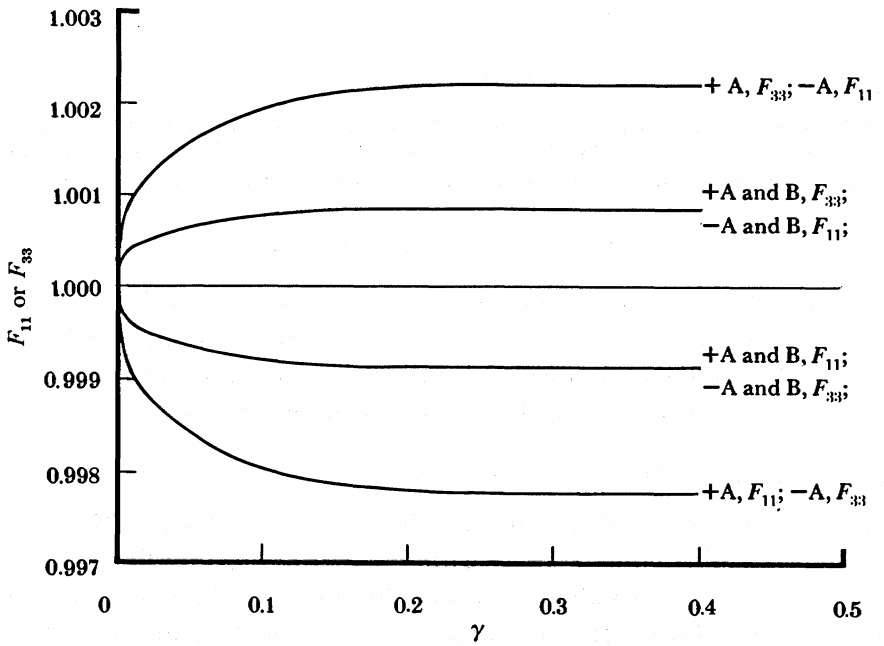

FIGURE 14. Stretches along the x_1, x_2 and x_3-axes as a function of shear strain for the ideal textures subject to unconstrained shear. Note that the ideal textures produce no stretch normal to the shear plane, i.e. produce no 'Swift' effect. The notations and material parameters used are the same as in figure 13.

the stress components saturate within a shear strain of 0.2 as expected because the ideal texture orientations are stable and the slip-system strengths saturate. The shear stress τ_{12} is largest for the C-texture and smallest for the partial A-fibre textures. The B_f fibre texture produces an intermediate shear stress and the combination of A-fibre and B-fibre textures gives a shear stress greater than that of the A-fibre alone, but less than that of the B-fibre. Similarly, mixtures of A and B-fibre textures produce axial stresses τ_{22} and hoop stresses τ_{11} that are intermediate to the stresses attained for individual texture components. The B_f and C-textures give no axial or hoop stresses. In contrast, the partial A-fibres produce a large hoop and axial stress whose signs depend upon the type of fibre, e.g. for positive shear, an A_f texture causes tensile hoop and axial stresses. In this case, the saturated stress ratios τ_{11}/τ_{12} and τ_{22}/τ_{12} are *ca.* 0.8 and *ca.* 0.2, respectively. With these results in mind, we will later examine results for '300' and '489' grain polycrystals and be able to correlate changes in texture with the calculated variations in τ_{12}, τ_{11} and τ_{22}.

For 'unconstrained' boundary conditions, the shear stress response is identical to the constrained case. The F_{11} component of the deformation gradient behaves in a manner analogous to τ_{11}, saturating within a strain of 0.2. For positive shear, the $\bar{A}_f$ texture causes hoop extension and the A_f causes hoop contraction. Both the B_f and C-textures by themselves produce no hoop deformations. Thus, mixing of A_f and B_f results in a smaller effect even though for the A-fibre, the normal stretches are small: less than 1.003. Interestingly, none of the ideal textures produce any axial deformations: F_{22} is constant. This result suggests that the axial stresses that are observed for torsion with fixed ends have origins that, at least in part, are different from the axial elongations that are observed in experiments with free ends.

3.2.2. *Deformation response of polycrystals with random grain orientation distributions*

The effect of constraint on the strain-hardening behaviour of polycrystals constituted from the '300' grain distribution is shown in figure 15. For specimens subjected to constraints, normal stresses develop and evolve with strain as shown. There is undoubtedly a significant effect due to the finite number of grains that, in part, accounts for the minor oscillations of the normal stresses. The shear stress against shear strain behaviour follows trends that in a sense parallel those shown earlier for the textures. The behaviour of τ_{12} against γ is very similar for the three constrained cases and displays a slight 'textural softening' in the strain range $0.8 \leqslant \gamma \leqslant 2.25$. Here it should be recalled that the slip plane-strain hardening, specified by equation (2.11), saturates after strains $|\gamma^{(\alpha)}| \geqslant 0.1$. For the polycrystal this means that the grains have become effectively ideally plastic after strain of about $\gamma = 0.2$. On the other hand, the 'unconstrained' specimen displays a continuous (textural) strengthening, of about the same magnitude, in the strain range where the 'constrained' specimens all soften. In this case, at a shear strain of $\gamma \approx 2.4$ a maximum is attained and τ_{12} begins to fall. Textural softening is commonly reported for polycrystal analyses based on idealized rate-independent Taylor-type models. However, the present results demonstrate that such behaviour depends not only on initial grain distributions and imposed strains, but also on overall imposed constraint.

The behaviour of the normal stresses has some qualitative similarities to what was described as background in §1.2 for an incompressible nonlinear elastic solid, e.g. for the 'fully constrained' polycrystalline specimen τ_{22} is compressive in the strain range shown, although we will see later that the normal stress on the shearing plane tends to become *tensile* at larger strains. The normal stress τ_{11} is tensile for nearly all strains except in the range $0.2 \leqslant \gamma \leqslant 0.9$,

PHILOSOPHICAL TRANSACTIONS OF THE ROYAL SOCIETY A MATHEMATICAL, PHYSICAL & ENGINEERING SCIENCES

but this behaviour, as will be shown in figure 16, is sensitive to the initial grain distribution. The difference $\frac{1}{2}(\tau_{11}-\tau_{22})$ grows slowly with strain, and in fact nearly saturates, as does the ratio $(\tau_{11}-\tau_{22})/\tau_{12}$ because τ_{12} nearly saturates. This is in marked contrast to the deformation theory behaviour discussed in §1.2 for which $(\tau_{11}-\tau_{22})/\tau_{12}$ would be expected to continuously increase.

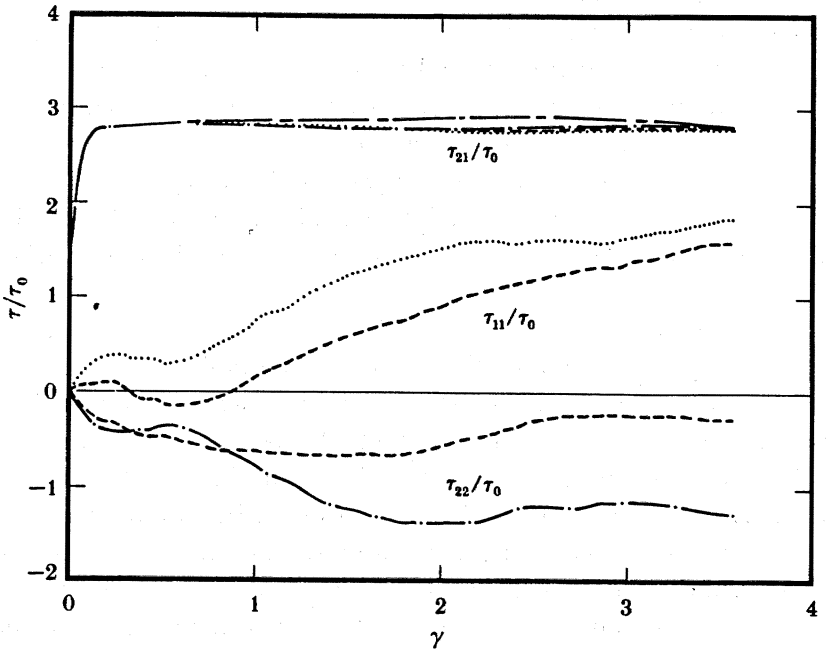

FIGURE 15. Stress–strain behaviour for the '300' grain distribution subjected to the four types of boundary constraints: fully constrained torsion (– – –), torsion with mandrel (· · · ·), torsion with end constraint (–·–·–·), and unconstrained torsion (———). The material parameters are $h_s = 0.0$, $q = 1.0$, and $m = 0.005$.

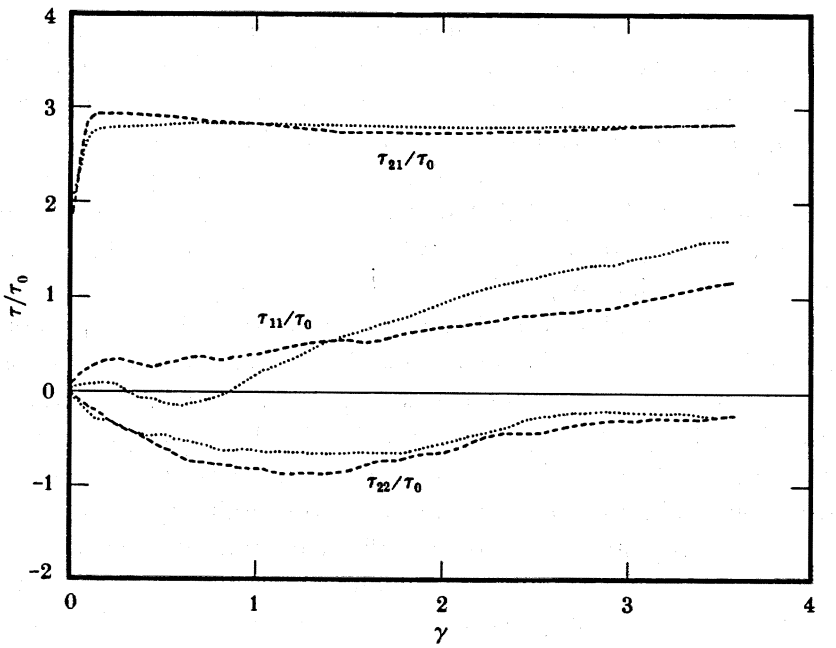

FIGURE 16. Stress–strain behaviour for the '300' (· · · ·) and '489' (– – – –) grain distributions contrasting the effect of slightly different initial grain distributions on the 'fully constrained' response. Note that the most significant effect is on the normal stress τ_{11} along the direction of shear. The material parameters are as in figure 15.

It is also of interest to note when one of the kinematical constraints is relaxed and replaced by either the condition $\tau_{11} = 0$ or $\tau_{22} = 0$, the other normal stress becomes larger in magnitude. This feature is predictable even within the context of nonlinear elasticity by the following observation. It is found that with any of the sets of constraints considered here that there is no trend for significant normal strains to develop in the x_3-direction. This means, because the overall deformation is nearly incompressible, that if either F_{11} or F_{22} is fixed at 1.0 then no normal strains will develop. Hence, the deformation is essentially 'fully constrained'. Then appealing to equations (1.12) applied to the 'fully constrained' case, when $\sigma_{11} = 0$, $\sigma_m = (\frac{-1}{\sqrt{3}})\,(\mathrm{d}\Phi/\mathrm{d}\epsilon_e)\cos 2\psi$ and $\sigma_{22} = (\frac{-2}{\sqrt{3}})\,\mathrm{d}\Phi/\mathrm{d}\epsilon_e)\cos 2\psi$, or σ_{22} is twice as large in magnitude as it would be if $\sigma_m = 0$. A similar argument applies for the case where $\sigma_{22} = 0$. There is then some rudimentary correspondence between the polycrystal model behaviour and a simple deformation theory; this is explored in more detail in connection with other phenomenological theories in §4.2.

Figure 16 shows the influence of grain orientation distribution on stress–strain behaviour for the case of a 'fully constrained' specimen. The strain-hardening behaviour itself is very similar except for an approximately 7% difference in the shear stress at full yield. The normal stresses are also similar and, as noted above, both τ_{11} and $\frac{1}{2}(\tau_{11} - \tau_{22})$ are positive over most of the strain range.

Figure 17 shows the influence of slip-system strain hardening on polycrystal strain hardening and on the development of normal stresses. The influence of introducing a non-vanishing asymptotic hardening or higher latent hardening is to raise the level of the shear stress–strain curves without changing their characteristics otherwise. Although the small amount of hardening given by $h_s = 0.1$ is seen to be sufficient to eliminate the decrease in τ_{12} because of

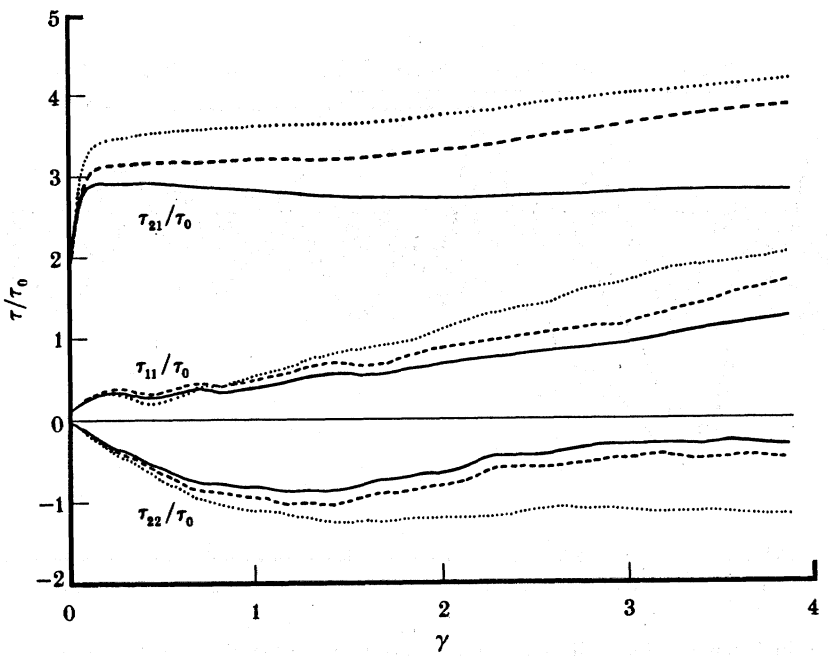

FIGURE 17. Stress–strain behaviour for 'fully constrained' shear of the '489' grain distribution illustrating the effects of strain hardening and latent hardening: $h_s = 0.0$, $q = 1.0$ (——); $h_s = 0.1$, $q = 1.0$ (– – – –); and $h_s = 0.1$, $q = 1.4$ (· · · ·). In all three cases shown, $m = 0.005$. Note that a quantitative description of texture evolution for these cases is provided in figure 8.

the textural softening, the shear stress–strain curves are still concave-outwards from the stress–strain origin. Similarly for the normal stresses, the principal effect of increasing the slip system hardening is to increase their magnitudes.

Figure 18 illustrates some of the trends that occur with increasing strain rate sensitivity. As in the earlier quantitative texture analysis of figure 9, we show results for $0.005 \leqslant m \leqslant 0.05$ and for very large strains up to 35.0. To observe some interesting effects of viscosity, we also include results for $m = 0.2$ and $m = 0.5$. When the shear strains are less than $\gamma \approx 9$ the behaviour of τ_{12} for all values of m in the range $0.005 \leqslant m \leqslant 0.05$ is qualitatively similar except that yielding occurs at lower stress levels for the more rate-sensitive materials. Also for $0.005 \leqslant m \leqslant 0.05$, at larger shear strains there occurs a rather abrupt textural shear strengthening, followed by an eventual softening. The strengthening occurs at a strain of about $\gamma \approx 10$ for $m = 0.05$ but not until a strain of $\gamma \approx 15$ for $m = 0.005$. This strengthening can be understood in terms of the texture transients shown in figure 9 and the ideal texture calculation results in figure 13. Referring to figure 9, for $m = 0.05$ one notes an abrupt decrease in the fraction of A-fibre poles at $\gamma \approx 9$ and a sharp increase in the fraction of B-fibre and C poles beginning at $\gamma \approx 10$. From figure 13 we know that the grains having B-fibre and C-texture orientations produce the largest shear stresses. Thus the τ_{12} transient appears to be a direct result of transients in texture evolution. The same sort of analysis can be applied to the τ_{12} transient between $\gamma = 1$ and $\gamma = 4$. Here, as evidenced by figure 8 for $h_s = 0.0$, $q = 1.0$ and $m = 0.005$, the C-texture increases at $\gamma \approx 1.8$ causing a slight increase in τ_{12} as evidenced by figure 18. At these smaller

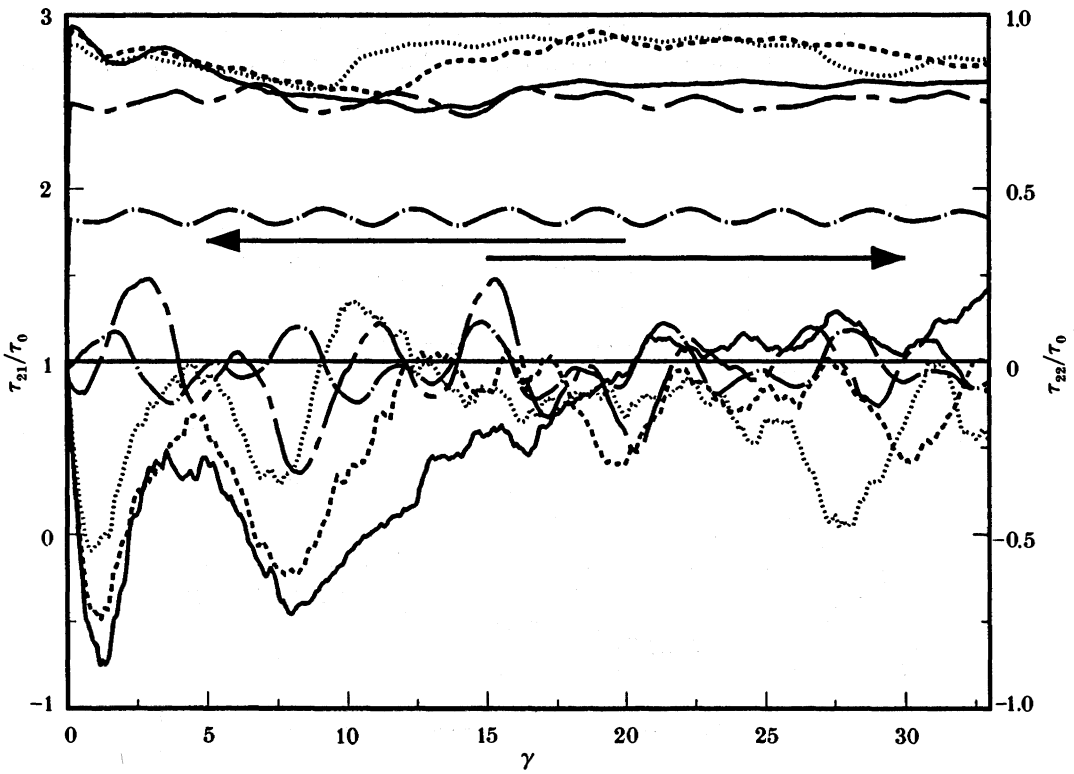

FIGURE 18. Stress–strain behaviour for 'fully constrained' shear of the '489' grain distribution illustrating the influence of very large strains and strain-rate sensitivity: $m = 0.005$ (——), $m = 0.02$ (– – – –), $m = 0.05$ (· · · ·), $m = 0.2$ (— — —), and $m = 0.5$ (—·—). Plots of the normal stress τ_{22} are referred to the right-side axis. The common material parameters are $h_s = 0.0$ and $q = 1.0$.

PHILOSOPHICAL TRANSACTIONS OF THE ROYAL SOCIETY A MATHEMATICAL, PHYSICAL & ENGINEERING SCIENCES

strains the stress transients occur as the ideal textures initially form. At the larger strains sharp textures have already formed and the transients are caused by ideal texture transitions. Direct physical interpretation of this behaviour should be made cautiously owing to the extremely large strains involved.

The axial stress τ_{22} is more sensitive to the evolution of texture than τ_{12} and, in particular, to texture transients. Referring for example to the case where $m = 0.05$, several transients are apparent that can be qualitatively understood in terms of the relative intensities of A_f, $\bar{A}_f$ and C-textures. First recall that the A_f texture by itself produces a tensile axial stress, the $\bar{A}_f$ texture produces a compressive stress, and the C-texture produces no axial stress. Thus, the increase in axial stress in the range $1.0 \lesssim \gamma \lesssim 5.0$ can be understood to result in part from the increase in the A_f partial fibre texture. In the range $5.0 \lesssim \gamma \lesssim 7.5$ the axial stress decreases because of the increase in the $\bar{A}_f$ texture as noted earlier in §3.1. Beyond this strain the axial stress increases and becomes tensile, reaching a maximum at $\gamma \approx 10$. For $7.5 \lesssim \gamma \lesssim 10.0$ both the A_f and $\bar{A}_f$ partial fibres decrease in intensity while the axial stress increases. In this strain range it is inappropriate to interpret axial stresses solely in terms of the contributions of grains within ideal textures because a large fraction of the grains are undergoing texture transitions and are outside the ideal orientations. These 'outside' grains influence the constitutive response in a way that depends sensitively on grain orientation. The constitutive response for the other strain-rate sensitivities can be similarly analysed.

Increased strain-rate sensitivity in the range $0.005 \leqslant m \leqslant 0.05$ does not change the qualitative features of normal stress development but does very much decrease the magnitudes of the stress, and as noted earlier, changes the transient strain scale. This is particularly interesting in that large decrease in normal stress magnitudes occurs even though there is relatively little change in shear strength level. An explanation in terms of ideal textures is not apparent. It should also be noted that for the three levels of strain-rate sensitivity in this range τ_{22} becomes tensile. This transition is a strictly large strain phenomenon. As expected the transition occurs first at a shear strain of $\gamma \approx 9$ for $m = 0.05$ and at a larger strain $\gamma \approx 20$ for $m = 0.005$. Transitions of this type have been observed experimentally by Montheillet *et al.* (1984). They observe a similar decrease in the magnitude of axial stress and a change in strain scale in copper with increasing temperature. One is led to speculate that their results are linked to the increase in strain-rate sensitivity with increasing temperature.

In figure 18, stress–strain behaviour is also shown for two cases of very large values of m that are beyond those characteristics of low-temperature dislocation slip. As the material's rate sensitivity increases, the normal stresses are continuously reduced in magnitude and begin to oscillate about zero. The shear stress also oscillates; this is most obvious for $m = 0.5$. As previously shown, the ideal texture components become less sharp as the strain-rate sensitivity is increased. In fact, for the very large strain-rate sensitivity considered here, we find that there is almost no tendency for textures to form. The stress oscillations and the lack of texture formation have interesting origins that are traced to the near vanishing of the plastic spin defined in equation (2.6). For an FCC crystal it may easily be shown that

$$W^{\mathrm{p}} = \sum_{\alpha=1}^{12} \dot{\gamma}^{(\alpha)} W^{(\alpha)}$$

vanishes for all stress states if $m = 1.0$. This means that the lattice spin W^* introduced in equation (2.7) is equal to the total spin W of the material. With $m = 0.5$ essentially the same

result is true. The ideal texture components are crystallite orientations that undergo shear without lattice rotation, but because $W^p \approx 0$ lattice rotations are forced to occur by the applied mode of deformation, i.e. by W, and hence ideal textures cannot form. Also, the observed oscillations of stress are caused by these lattice rotations, which periodically give geometrically harder and softer orientations.

3.3. *The 'Swift effect'*

Under 'unconstrained' shearing, where $\tau_{11} = \tau_{22} = 0$, the specimens undergo normal strains as discussed in connection with the hyperelastic model of §1.2. The phenomenology of this is shown in figure 19. For grain distributions that are initially nearly isotropic, there is extension normal to the shearing plane as is evidenced by the figure. The effect depends on the initial grain distribution although this dependence appears to decrease at larger shear strains. Note also that increasing the rate sensitivity from $m = 0.005$ to $m = 0.02$ lessens the amount of axial extension. The Swift effect is also very sensitive to boundary constraint. For the 'torsion with mandrel' conditions the imposed constraint, i.e. $F_{11} = 1.0$, limits the axial stretch F_{22} to the small values shown. As previously mentioned, this is a result of near-incompressibility and the fact that significant normal strains in the x_3-direction have no tendency to develop: in all cases this strain component has magnitude on the order of *ca.* 1%. Comparisons with Stout's experimental data (M. Stout, personal communication 1984) on α-brass tested in quasi-static torsion at room temperature are also given in the figure. Note that Stout's data are bounded by the two sets of boundary conditions. More will be said about this below.

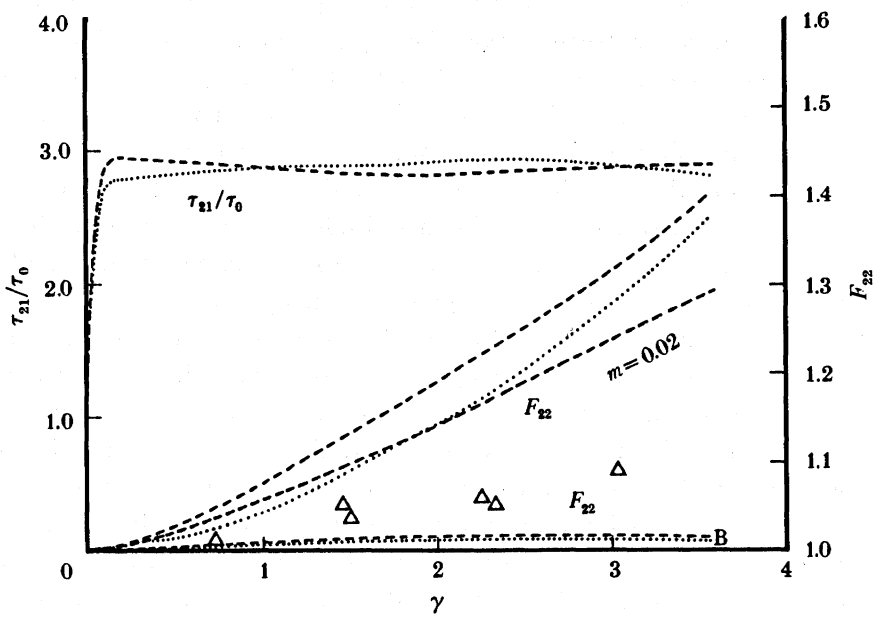

FIGURE 19. Shear stress τ_{21} and axial stretch F_{22} as a function of γ for the '300' grain distribution (· · · ·) and the '489' grain distribution (– – – –) subject to the 'unconstrained' boundary condition set. The F_{22} against γ response for both distributions under the 'mandrel' constraints is also included and indicated by the letter 'B' on the figure. The common material parameters are $h_s = 0.0$ and $q = 1.0$. In all cases $m = 0.005$ except for the one curve as indicated. The unpublished data of Stout (△) is also shown.

In figure 20 the calculated Swift effect for 'unconstrained' shear is shown compared to Stout's data (which are the same data appearing in the previous figure) and Swift's (1947) original experimental data for copper tested in quasi-static torsion. Note that both Stout's and Swift's data were obtained from torsion of thin-walled tubes. Their measurements are in close correspondence, but both are about a factor of 3 below the predicted effect based on 'unconstrained' shear. We suggest therefore that the constraint of the 'thick-walled' flanges serving as the gripping parts of thin-walled tube specimens retards the development of hoop strains in the thin-gauge section and thus retards the development of plastic strains normal to the shearing plane. Indeed, as mentioned in §1.1, it was noted by Swift (1947) that extensions were larger for tube specimens than for solid rods where in the latter the material at the outer diameters is constrained by the core material, which undergoes smaller shear strains.

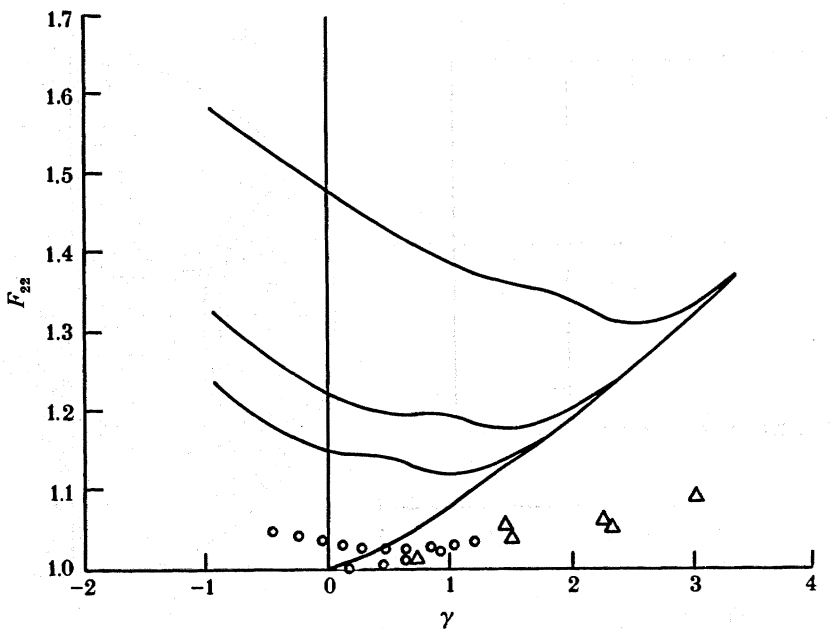

FIGURE 20. Axial stretch F_{22} for three calculations of fully reversed shear (——) following the experiments of Swift (1947). The material parameters are $h_s = 0.0$, $q = 1.0$ and $m = 0.005$. The '489' grain distribution and the 'unconstrained' shear conditions are used. The unpublished data of Stout (△) and the data of Swift (○) are shown for comparison.

Figure 20 also shows three examples of reversed shear that simulate the reverse torsion tests of Swift (1947), which are also shown in the figure. Once again the phenomenology is very similar but the calculated magnitudes are too high. As the direction of shear is reversed the normal strains at first decrease; this is followed by an increase and an eventual near-parabolic behaviour. Although one cannot tell from the figure, if the experimental curve of Swift is plotted on a different scale so as to make more evident its features, then it is seen to exhibit similar transients in F_{22} upon reversed shearing as just described. Figure 21*a* shows the shear-stress response for the three reversed shear simulations. In all cases there is essentially no perceptible Bauschinger effect for reverse yielding. At the strain levels shown in figure 21*a* reverse flow occurs initially with continued (slight) hardening at a level of magnitude consistent

PHILOSOPHICAL TRANSACTIONS OF THE ROYAL SOCIETY A MATHEMATICAL, PHYSICAL & ENGINEERING SCIENCES

with the low level of hardening during forward straining. However, in all cases hardening is accompanied by a slight (textural) softening.

Texture development is shown during reverse straining by figure 21 *b–d* for the case of a forward strain of $\gamma = 3.36$. Figure 21 *b* corresponds to a small reverse strain of 2% and illustrates a texture that is very similar to that shown earlier in figure 6 *d*. Figure 21 *c* shows that after a reverse strain of about 2.52 the texture is substantially altered. One effect is a large counterclockwise rotation of the texture such that poles that fit, at $\gamma = 3.36$, within the bands corresponding to the A_f ideal texture component in quadrants 2 and 4 are shifted more closely toward the $\bar{A}_f$ bands in quadrants 3 and 1, respectively. This gross rotation of the texture as a whole upon strain reversal is manifested in the observed transients of axial extension,

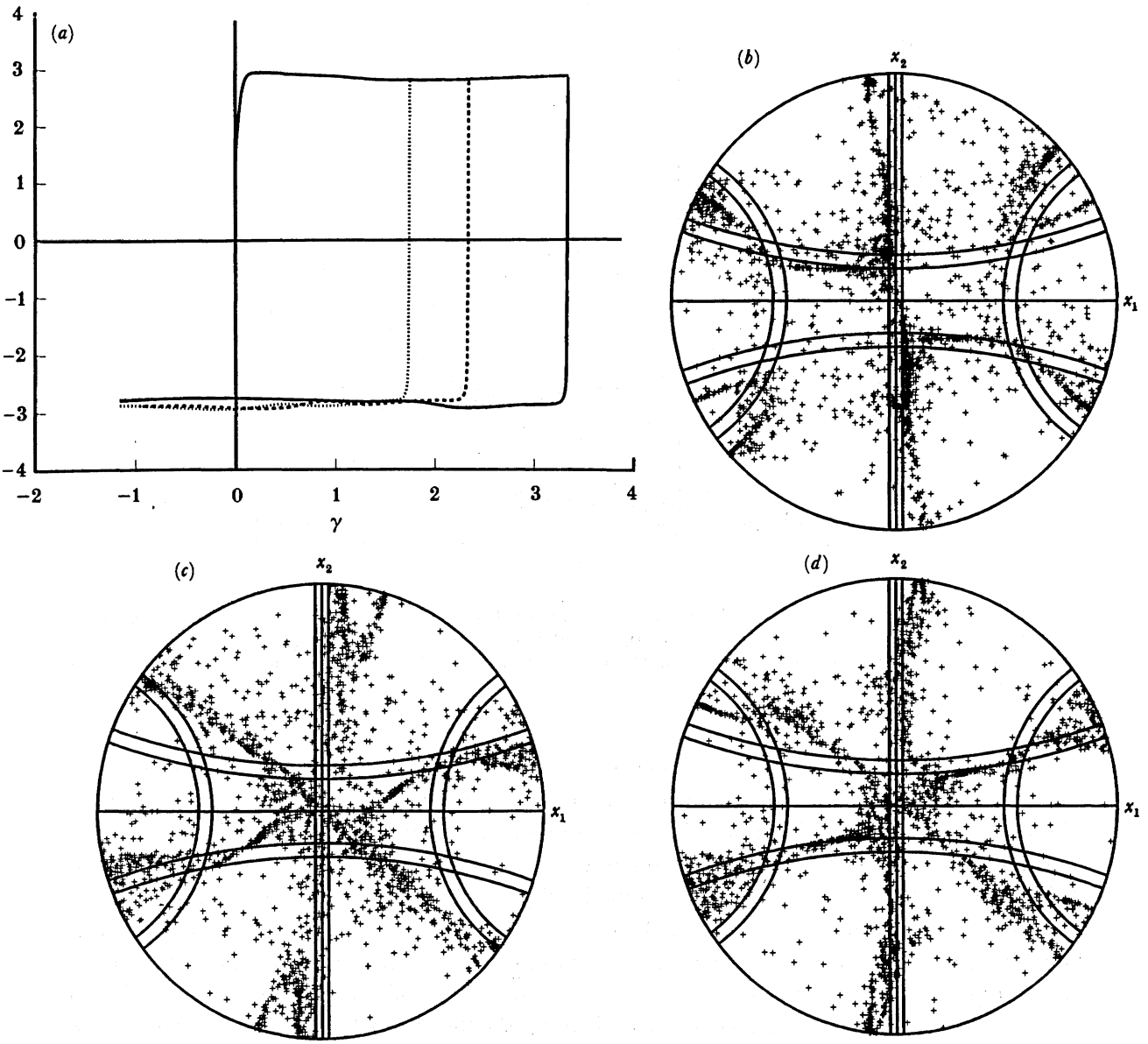

FIGURE 21. (*a*) Shear stress against shear strain for the three cases shown in figure 20. Also shown is the texture evolution for the case of reverse straining from $\gamma = 3.36$ to (*b*) $\gamma = 3.34$, (*c*) $\gamma = 0.84$, and (*d*) $\gamma = -1.16$.

PHILOSOPHICAL TRANSACTIONS OF THE ROYAL SOCIETY A MATHEMATICAL, PHYSICAL & ENGINEERING SCIENCES

although it is interesting to note that the shear strength seems unaffected by this. At a shear strain of $\gamma = -1.16$ the texture has now become very similar to what it would have been had deformation been unidirectional with shearing directed along the $-x_1$-axis, and as a result, the transients in axial extension subside.

4. Discussion

4.1. *Polycrystal model studies*

The simulations described above allow a number of correlations between texture evolution and constitutive response to be made; some of these have already been presented, a few others are described below.

Experimental studies of texture evolution during large-strain shear have indicated that the textures that form can indeed be described as a mixture of the three ideal textures defined in §2.4. In particular, it has been noted by Montheillet *et al.* (1984) that at strains greater than $\gamma \approx 5$ for copper twisted at room temperature there is a tendency for the C-component to increase whereas the A_f ideal texture decreases. Canova *et al.* (1984) have attempted to simulate this behaviour using their implementation of the 'method of relaxed constraints' introduced by Honneff & Meeking (1978). The present results demonstrate, on the other hand, that such transitions are in fact a *natural outcome* of a finite strain, strain-rate-dependent model such as ours. Figure 9 shows that when the strain-rate sensitivity is in the range corresponding to $0.005 \leqslant m \leqslant 0.05$ the A_f component undergoes large decreases as the C-component undergoes increases. The effect is quite sensitive to the value of m; the strain levels where this occurs are less with higher strain-rate sensitivity. Figure 13 further shows that the C-component is characterized by a higher shear strength than the A_f fibre texture, which correlates with the textural strengthening observed in figure 18 at the shear strains where the $A_f \rightarrow C$ transition occurs. We note also that the intensification of the ideal C-texture component does, in fact, occur as a result of grains whose orientations change from those within the A_f fibre to those within the ideal C-texture. This effect has been clearly illustrated in the motion picture films of Lowe & Asaro (1985) where the transition appears as a continuous 'stream' of poles migrating from orientations within the A_f fibre texture to those within the C-texture. Also as shown in figure 9, the B-component undergoes continuous increases, except in the case of high strain-rate sensitivity $m = 0.05$, which is also in agreement with experiment for copper twisted at elevated temperatures (Montheillet *et al.* 1985).

The inclusion of rate sensitivity is shown to lead to textures that are more diffuse than those predicted with rate-independent idealizations. A long-standing discrepancy between textures predicted from rate-independent slip theories and those measured experimentally is that the predicted textures are too sharp. Thus, the understanding of the effect of strain-rate sensitivity is an important step toward resolving past discrepancies between theory and experiment. Other causes of more diffuse textures are clearly important and should be evaluated in future studies. Included in these are the non-uniform plastic strains and non-uniform slip modes that develop within grains, especially at interfaces. This particular problem has currently been studied quantitatively (Harren *et al.* 1988) via finite-element methods and the results provide suggestions for including the effects of interfaces in initiating non-uniform slip in improved models.

Another interesting experimental observation that, to date, has been difficult to explain via

PHILOSOPHICAL TRANSACTIONS OF THE ROYAL SOCIETY A MATHEMATICAL, PHYSICAL & ENGINEERING SCIENCES

simple polycrystal models is the transition from compressive to tensile normal stresses on the shear plane (Montheillet *et al.* 1985). This transition is also evident in figures 9 and 18 and can be partly understood in terms of the ideal texture behaviour illustrated in figure 13. The model calculations for the ideal textures show that the A_f fibre texture in itself, or in combination with the other two ideal textures, gives rise to a *tensile* stress on the shear plane; the B-fibre and C ideal textures produce no normal stresses of this type. This suggests that the compressive stresses that initially develop are caused by the collection of grains (acting together) that are *not* in any of the three ideal textures that characterize the overall texture at large strains. Similarly, the tensile stresses that occur at large strains must also be attributed to the collected effect of grains not having ideal texture orientations. Comparing figures 9 and 18, it is clear that the tensile stresses occur during texture transitions and are not caused by the tensile stress contribution of the A_f fibre texture. Peak tensile stresses occur while the fraction of grains with A_f orientations is decreasing and the fraction of grains with C-texture orientations is increasing. The motion pictures of Lowe & Asaro (1985) have shown that a large number of grains simultaneously have non-ideal orientations as they migrate together from A_f orientations towards C orientations. Note also that strain-rate sensitivity has an influence on this transition; as m increases the strain at which τ_{22} first becomes tensile decreases. In addition, at 'smaller' strains, e.g. $\gamma < 15$, the magnitude of τ_{22} is less for the more rate-sensitive materials.

We now present correlations of the 'Swift effect' for 'unconstrained' shear as illustrated in figure 19 with the gross rotation of the developed texture as illustrated in figure 6*d*. Looking at any of the figures 6*a–c*, the shear plane normal is in the x_2-direction. Now, turning to figure 6*d*, one is led to say that the shear plane normal is located at *ca.* 7° counterclockwise from the x_2-axis for $\gamma = 3.60$ because the pole figure exhibits a gross 7° (or 0.12 rad) rotation about the x_3-axis at this strain level. Because the pole figures 6*a–c* are effectively the results of simple shearing along the x_1-axis, one speculates that the pole figure 6*d* corresponds to simple shearing along an axis that is inclined at *ca.* 7° counterclockwise from the x_1-axis. As it turns out, this is very nearly true.

First, note that the 'unconstrained' axial extensions in figure 19 are represented fairly well by the relation

$$\mathrm{d}F_{22}/\mathrm{d}\gamma \approx 0.15, \quad \text{for} \quad \gamma \gtrsim 3. \tag{4.1}$$

Next, to aid this discussion, introduce a coordinate system x_1', x_2', and x_3' whose axes are obtained by rotating the x_1, x_2, x_3 system counterclockwise about the x_3-axis by an angle ϕ, which is meant to be *ca.* 7°. Now, let $\dot{F}_{22}'$ be the rate of stretching along the x_2'-axis. One finds that

$$\dot{F}_{22}' = \dot{F}_{22} - \dot{\gamma}\phi + O(\phi^2), \tag{4.2}$$

where the small angle approximation of ϕ has been used. Because we want to look at simple shearing along these inclined axes, $\dot{F}_{22}' = 0$ and hence

$$\mathrm{d}F_{22}/\mathrm{d}\gamma \approx \phi. \tag{4.3}$$

The observation (4.1) indicates that $\phi \approx 0.15$ rad or *ca.* 8.6° should be true whereas figure 6*d* indicates $\phi \approx 7°$ or *ca.* 0.12 rad. If one examines the calculated $\dot{F}$ for the case at hand, e.g. 'unconstrained' shear of the '300' grain distribution with $h_s = 0.0$, $q = 1.0$, and $m = 0.005$ at $\gamma = 3.60$, one finds that the deformation is very nearly simple shear on inclined axes defined by $\phi = 0.13$ rad or 7.7°. Hence, the angle of rotation ϕ of the pole figure and the rate of axial stretching are closely correlated.

These obervations have some important ramifications. The correlations of axial stress development with pole figure rotations as performed by Montheillet *et al.* (1985) seem to be a bit misdirected: our results indicate that *axial strains* are associated with texture rotations whereas axial stresses are associated with textures that are more or less unrotated. These observations on axial stretching also have interesting similarities to the 'unconstrained' hyperelastic model of §1.2. The polycrystal calculations indicate that the pole figure initially exhibits $\phi = 0$ and then quickly develops to $\phi \approx 7°$ after $\gamma \gtrsim 3$. For $\gamma \gtrsim 3$, the motion picture films of Lowe & Asaro (1985) indicate that ϕ increases very slowly with increasing shear strain. Hence, in a sense, equation (4.3) represents a sort of asymptotic condition for the polycrystal model. Under this asymptotic condition of simple shearing on these inclined axes, a scribe line initially parallel to the x_2-axis will be oriented at about 7° above the x_1-axis at large strains, whereas at large strains for the hyperelastic model, this scribe line would lie 45° above the x_1-axis.

Influences of latent hardening on texture development and stress–strain response are shown in figures 8 and 17. In general the tendency is for sharper textures to develop with higher latent hardening ratios, at least for strains less than $\gamma \approx 4$, as indicated by the stronger intensities of the A_f and B_f-ideal textures. It is noteworthy that the shear textures are still well represented by combinations of the ideal textures but with different intensities. As evidenced by figure 8, the 'shapes' of the texture intensity curves are relatively unaffected by the latent hardening, and thus the qualitative features of the strain hardening curves are similar, as shown in figure 17. As mentioned earlier, the slip system strain hardening law given by equations (2.10) and (2.11) leads to a saturation of slip system strength when $h_s = 0$; with $h_o = 8.9\tau_o$ this effectively means that saturation occurs at shear strains $|\gamma^{(\alpha)}|$ of about 0.1. The structure of the strain hardening curves is thus a direct result of textural effects, and in particular the softening in the curve of τ_{12} against γ is a 'textural softening'. Textural softening is offset by the introduction of stronger strain hardening h_s.

As mentioned in the Introduction, an aim of the present work is to provide a comprehensive framework for analysing large-strain shear and for guiding the development of phenomenological theories that can in turn be used to analyse general types of large-strain deformation processes. The latter include metal-forming processes and failure caused by strain localization and ductile rupture. More complete analysis of the micro- and macromechanical phenomenology of large-strain shear requires much more experimental study. This should include more detailed studies of the evolution of textures as influenced by stress and strain state, as well as by material properties. Correlations of texture and microstructure with constitutive response are also needed. The framework given here, although comprehensive, is incomplete in that mechanisms such as non-uniform slip within grains, and non-uniform material properties, are not yet included. Future combined experimental and model studies will provide a quantitative means of including such effects. Our models are, however, in a form to provide important guidance for the development of phenomenological theories. As a first important step in this direction we next present a comparison of the shear response predicted by a number of phenomenological theories, including J_2-corner theory and two kinematic hardening models, with those of our physical model. We note that both corner theories and kinematic hardening models have been used over the past several years to study problems related to shear localization and necking and this provides a special impetus for correlating them with the physical theory.

PHILOSOPHICAL TRANSACTIONS OF THE ROYAL SOCIETY A MATHEMATICAL, PHYSICAL & ENGINEERING SCIENCES

4.2. *Phenomenological studies*

It is well known that the classical theory of the Prandtl–Reuss flow rule (which incorporates an isotropically hardening smooth von Mises yield surface), i.e. J_2-flow theory, is inconsistent with the predictions of physically based, crystallographic slip models: rate-independent crystallographic slip models predict the existence of corners or vertices on the yield surface. In fact, Asaro & Needleman (1985) have used the rate-independent limit of their rate-dependent polycrystal model to calculate off-set plastic strain yield surfaces of plastically strained polycrystals, and the development of vertices (or at least areas of very high curvature) at the yield surfaces' load points was shown. The classical von Mises Prandtl–Reuss theory states that the direction of the plastic rate of deformation $\boldsymbol{D}^{\mathrm{p}}$ is independent of the direction of the Jaumann rate of deviatoric Kirchhoff stress $\overset{\nabla}{\boldsymbol{S}}$, whereas in rate-independent crystallographic slip models, the direction of $\boldsymbol{D}^{\mathrm{p}}$ depends upon that of $\overset{\nabla}{\boldsymbol{S}}$, and appropriately enough, this dependence is called a vertex effect. The simplest vertex model of plasticity is the hypoelastic deformation theory of Stören & Rice (1975). In this theory, $\boldsymbol{D}^{\mathrm{p}}$ is not necessarily normal to what would be the von Mises yield surface. Also, being a deformation theory, it is not directly applicable to paths of plastic loading that exhibit significant deviation from proportionality, i.e. to paths in which the direction of $\overset{\nabla}{\boldsymbol{S}}$ differs significantly from that of the deviator of Kirchhoff stress $\boldsymbol{S}$. The J_2-corner theory of Christoffersen & Hutchinson (1979) eliminates this restriction. In this theory, the yield surface vertex is modelled as a stress space hypercone with axis $\boldsymbol{S}$. For plastic loading along paths that coincide or nearly coincide with proportional loading, the response is taken as that of hypoelastic deformation theory. This régime of behaviour is called 'total loading'. Elastic unloading occurs when the direction of $\overset{\nabla}{\boldsymbol{S}}$ lies in or within the cone surface. For loading paths that lie between total loading and elastic unloading, the Christoffersen–Hutchinson theory provides a region of transitional response where the instantaneous moduli smoothly increase from the deformation theory moduli of the total loading régime to the linear elastic moduli of the unloading régime. The J_2-corner theory has been extended by Hutchinson & Tvergaard (1980) to include hyperelastic total loading response.

The high curvature of the yield surface in the neighbourhood of its load point can be described to some extent by the classical plasticity theory of kinematic hardening. Here the hardening behaviour of the material is described by a constant radius von Mises yield surface that translates through stress space as the plastic loading proceeds. Nagtegaal & de Jong (1982) have shown that the traditional Prager–Ziegler form of this theory leads to oscillatory solutions of stress against strain in simple shear for a monotonically hardening material. This oscillation is a direct result of the evolution equation for the centre of the yield surface $\boldsymbol{\alpha}$, i.e. for the back stress, where the Jaumann derivative of $\boldsymbol{\alpha}$, i.e. $\overset{\nabla}{\boldsymbol{\alpha}}$, is taken proportional to $\boldsymbol{D}^{\mathrm{p}}$. Various authors have taken the viewpoint that the choice of objective rate is the salient issue in the resolution of this undesirable behaviour. Lee *et al.* (1983) have replaced $\overset{\nabla}{\boldsymbol{\alpha}}$ with a modified Jaumann derivative of $\boldsymbol{\alpha}$ where the spin measure is the rotation rate of the material line element that instantaneously coincides with the maximum tensile eigenvector of $\boldsymbol{\alpha}$. This approach eliminates the oscillatory behaviour in simple shear, at least for the case of constant hardening modulus.

Dienes (1979) has also taken this viewpoint. In the context of the simplest hypoelastic solid, where the Jaumann rate of stress is related to the rate of deformation by the usual linear elastic constants, the stress–strain response is also periodic in simple shear. Dienes eliminated this oscillatory behaviour by replacing the Jaumann derivative of stress with a modified Jaumann derivative (the Green–Naghdi derivative) whose spin measure is $\boldsymbol{R}\cdot\boldsymbol{R}^{\mathrm{T}}$, where $\boldsymbol{R}$ is the rotation tensor afforded by the polar decomposition theorem. In the context of kinematic hardening theory, Key (1984) has replaced $\overset{\nabla}{\boldsymbol{\alpha}}$ with the Green–Naghdi derivative of $\boldsymbol{\alpha}$ to eliminate the oscillations in simple shear (again at least for the case of constant hardening modulus). A more fundamental approach has been taken by Fressengeas & Molinari (1983). Along with exploring the effects of different objective rates of back stress, they modify the form of the evolution: the objective rate of $\boldsymbol{\alpha}$ is taken proportional to a linear combination of $\boldsymbol{D}^{\mathrm{p}}$ and $\boldsymbol{\alpha}$. Obviously, once a suitable form of the evolution equation (or any constitutive equation for that matter) has been established, it is a simple matter to express it in terms of any objective rate that one may desire.

To compare the polycrystal predictions of §3 to predictions based on phenomenological vertex-type descriptions, large-shear calculations have been performed with J_2-corner theory and two versions of kinematic hardening theory. In these calculations, attention is confined to plane strain incompressible deformations and $\boldsymbol{S}$ may be interpreted as the deviator of Cauchy stress. Within this context, the essential details of the three models are now presented.

The J_2-corner theory total loading (or deformation theory) material is taken as hyperelastic. The stress deviator is given by

$$\boldsymbol{S}=\frac{2}{\gamma_{\mathrm{e}}}\frac{\mathrm{d}\Phi}{\mathrm{d}\gamma_{\mathrm{e}}}(\epsilon_1\boldsymbol{N}_1\boldsymbol{N}_1+\epsilon_2\boldsymbol{N}_2\boldsymbol{N}_2), \tag{4.4}$$

where $\boldsymbol{N}_i$ are unit eigenvectors of $\boldsymbol{S}$ and ϵ_i are the principal values of logarithmic strain. The strain energy function is taken to depend only on the effective shear strain γ_{e}:

$$\Phi=\int\tau_{\mathrm{e}}(\gamma_{\mathrm{e}})\,\mathrm{d}\gamma_{\mathrm{e}},\quad \tau_{\mathrm{e}}=\sqrt{[(\tfrac{1}{2})\,\boldsymbol{S}:\boldsymbol{S}]},\quad \gamma_{\mathrm{e}}=\sqrt{[2(\epsilon_1^2+\epsilon_2^2)]}, \tag{4.5}$$

where τ_{e} is the effective shear stress. Hence, the deformation theory material is completely described by a curve of τ_{e} against γ_{e}. Relations (4.4) and (4.5) may be cast in rate form as (see Hill (1970))

$$\boldsymbol{D}=\boldsymbol{C}^{\mathrm{d}}:\overset{\nabla}{\boldsymbol{S}}, \tag{4.6}$$

where $\boldsymbol{D}$ is the rate of deformation. The elastic response is that of the simplest hypoelastic material, i.e.

$$\boldsymbol{D}^{\mathrm{e}}=\frac{1}{2\mu}\overset{\nabla}{\boldsymbol{S}}=\boldsymbol{C}^{\mathrm{e}}:\overset{\nabla}{\boldsymbol{S}}, \tag{4.7}$$

where $\boldsymbol{D}^{\mathrm{e}}$ is the elastic rate of deformation and μ is the elastic shear modulus. Using $\boldsymbol{D}=\boldsymbol{D}^{\mathrm{e}}+\boldsymbol{D}^{\mathrm{p}}$ gives the plastic response for total loading:

$$\boldsymbol{D}^{\mathrm{p}}=\boldsymbol{C}^{\mathrm{p}}:\overset{\nabla}{\boldsymbol{S}},\quad \boldsymbol{C}^{\mathrm{p}}=\boldsymbol{C}^{\mathrm{d}}-\boldsymbol{C}^{\mathrm{e}}. \tag{4.8}$$

The angular measure θ used to describe the transitional response of the material is

$$\cos\theta=\boldsymbol{\lambda}:\boldsymbol{P},\quad (\boldsymbol{S}:\boldsymbol{C}^{\mathrm{p}}:\boldsymbol{S})^{\frac{1}{2}}\boldsymbol{\lambda}=\boldsymbol{S},\quad (\overset{\nabla}{\boldsymbol{S}}:\boldsymbol{C}^{\mathrm{p}}:\overset{\nabla}{\boldsymbol{S}})^{\frac{1}{2}}\boldsymbol{P}=\boldsymbol{C}^{\mathrm{p}}:\overset{\nabla}{\boldsymbol{S}}. \tag{4.9}$$

The material behaviour lies: within the total loading régime when $0 \leqslant \theta \leqslant \theta_o$, within the transitional régime when $\theta_o < \theta < \theta_c$, and within the elastic unloading régime when $\theta_c \leqslant \theta \leqslant \pi$. The angle θ_c is determined from

$$(\overset{\nabla}{\boldsymbol{S}}_c : \boldsymbol{C}^p : \overset{\nabla}{\boldsymbol{\tau}}_c)^{\frac{1}{2}} \cos\theta_c = \boldsymbol{\lambda} : \boldsymbol{C}^p : \overset{\nabla}{\boldsymbol{S}}_c, \quad \overset{\nabla}{\boldsymbol{S}}_c = \cos\beta_c \boldsymbol{S} + \tau_e \sin\beta_c (\boldsymbol{N}_1 \boldsymbol{N}_2 + \boldsymbol{N}_2 \boldsymbol{N}_1), \tag{4.10}$$

where

$$\beta_c = \arctan\left(\frac{-\tau_y}{\sqrt{(\tau_e^2 - \tau_y^2)}}\right) + \pi \quad \text{or} \quad \beta_c = \beta_c^{\max}, \tag{4.11}$$

whichever is least. In (4.11), τ_y is the value of τ_e at initial yield, $\beta_c^{\max}$ is the angle introduced by Hutchinson & Tvergaard (1980) that defines the maximum allowable sharpness of the yield surface vertex, and the inverse tangent function refers to the principal branch. The angle θ_o is taken as $\theta_o = r(\theta_c - \frac{1}{2}\pi)$, where r is a constant such that $0 \leqslant r \leqslant 1$. The transition function $f(\theta)$ is

$$f(\theta) = 4g(\phi)\{4(g(\phi))^2 + (g'(\phi))^2\}^{-1}, \tag{4.12}$$

where prime denotes differentiation with respect to the indicated argument and

$$g(\phi) = \left\{1 - \left(\frac{\phi - \theta_o}{\theta_c - \theta_o - \frac{1}{2}\pi}\right)^n\right\}^{-2}, \quad \theta = \phi + \arctan\left(\frac{g'(\phi)}{2g(\phi)}\right), \tag{4.13}$$

where $n \geqslant 2$ and where the inverse tangent function returns values between 0 and $\frac{1}{2}\pi$. The plastic response in the transitional régime is given by

$$\left.\begin{aligned} \boldsymbol{C}^{tr} &= \tfrac{1}{2} f''(\theta) \boldsymbol{QQ} + \tfrac{1}{2} f'(\theta)\{\cot\theta(\boldsymbol{C}^p - \boldsymbol{PP} - \boldsymbol{QQ}) + \boldsymbol{PQ} + \boldsymbol{QP}\} + f(\theta)\boldsymbol{C}^p, \\ \boldsymbol{Q} &= \boldsymbol{P}\cot\theta - \boldsymbol{C}^p : \boldsymbol{\lambda}\,\mathrm{cosec}\,\theta, \quad \boldsymbol{D}^p = \boldsymbol{C}^{tr} : \overset{\nabla}{\boldsymbol{S}}. \end{aligned}\right\} \tag{4.14}$$

The shear calculations have been carried out with $\beta_c^{\max} = 135°$, $r = 0.5$, and $n = 3$. These constants have been used previously by Hutchinson & Tvergaard (1980) and Tvergaard *et al.* (1981).

In kinematic hardening theory, the direction of the plastic flow coincides with that of the radial tensor $\boldsymbol{r}$ of the yield surface, i.e.

$$\boldsymbol{D}^p = \frac{\dot\gamma_e^p}{2\tau_y}\boldsymbol{r}, \quad \boldsymbol{r} = \boldsymbol{S} - \boldsymbol{\alpha}, \quad \dot\gamma_e^p = \sqrt{(2\boldsymbol{D}^p : \boldsymbol{D}^p)}, \tag{4.15}$$

where $\dot\gamma_e^p$ is the effective plastic shear strain rate. In this theory, the plastic response is governed by the compliances

$$\boldsymbol{C}^k = \frac{1}{4\tau_y^2}\left\{\frac{1}{\mu_t} - \frac{1}{\mu}\right\}\boldsymbol{rr}, \tag{4.16}$$

where μ_t is the slope of the curve of effective shear stress against effective shear strain. Two types of back stress evolution have been used in the following calculations. The first type will be referred to as F.M. (Fressengeas–Molinari) evolution. The second type will be referred to as K (Key) evolution. Both forms have been considered previously by Fressengeas & Molinari (1983), and the K form has been considered previously by Key (1984). The F.M. evolution of back stress is given by

$$\overset{\nabla}{\boldsymbol{\alpha}} = B\boldsymbol{D}^p - \frac{1}{\sqrt{3}} A \dot\gamma_e^p \boldsymbol{\alpha}, \quad A \geqslant 0, \tag{4.17}$$

where the parameter A may be regarded as a damping constant. For rigid-plastic simple shear

with constant tangent modulus μ_t, it is an elementary exercise to show that oscillatory solutions of stress against strain are obtained if $A < 2\sqrt{3}$, and that $\boldsymbol{S}$ exponentially approaches a finite limit (as the shear strain tends to infinity) if $A > 2\sqrt{3}$. For constant μ_t, $A = 2\sqrt{3}$ corresponds to critical damping. Having chosen A (we have taken $A = 40$ in the following calculations), application of the consistency condition to (4.17) yields

$$B = \frac{1}{\tau_y}\left(\frac{1}{\dot{\gamma}^p_e}\boldsymbol{r}:\overset{\nabla}{\boldsymbol{S}}+\frac{1}{\sqrt{3}}A\boldsymbol{r}:\boldsymbol{\alpha}\right), \quad \dot{\gamma}^p_e = \frac{1}{2\tau_y}\left\{\frac{1}{\mu_t}-\frac{1}{\mu}\right\}\boldsymbol{r}:\overset{\nabla}{\boldsymbol{S}}. \tag{4.18}$$

The plastic and elastic rates of deformation are given by

$$\boldsymbol{D}^p = \boldsymbol{C}^k:\overset{\nabla}{\boldsymbol{S}}, \quad \boldsymbol{D}^e = \boldsymbol{C}^e:\overset{\nabla}{\boldsymbol{S}}, \tag{4.19}$$

where $\boldsymbol{C}^k$ is as in (4.16) and $\boldsymbol{C}^e$ is as in (4.7). The K evolution of back stress is given by

$$\overset{*}{\boldsymbol{\alpha}} = \frac{\boldsymbol{r}:\overset{*}{\boldsymbol{S}}}{\tau_y\dot{\gamma}^p_e}\boldsymbol{D}^p, \tag{4.20}$$

where * denotes the Green–Naghdi derivative, e.g.

$$\overset{*}{\boldsymbol{\alpha}} = \dot{\boldsymbol{\alpha}}-\dot{\boldsymbol{R}}\cdot\boldsymbol{R}^T\cdot\boldsymbol{\alpha}-\boldsymbol{\alpha}\cdot\boldsymbol{R}\cdot\dot{\boldsymbol{R}}^T, \tag{4.21}$$

and where $\dot{\gamma}^p_e$ may be determined from the second relation of (4.18) with $\overset{*}{\boldsymbol{S}}$ replacing $\overset{\nabla}{\boldsymbol{S}}$. Also, the plastic and elastic rates of deformation are given by relations (4.19) with $\overset{*}{\boldsymbol{S}}$ replacing $\overset{\nabla}{\boldsymbol{S}}$.

In each of the theories discussed above, it is necessary to describe the material hardening characteristics in terms of an effective-stress–effective-strain curve. Persuant, two effective shear stress-effective plastic shear strain curves have been calculated by means of two plane strain ($\epsilon_3 = 0$) compression polycrystal simulations. The first polycrystal calculation used the initial crystallite distribution with 196 grains (see §2.3), and the second used 489 grains. The first of the two polycrystal calculations was presented previously by Asaro & Needleman (1985), and the plane strain compression boundary conditions used for the two are given in relations (3.32) of that paper. Both polycrystals are characterized by $h_s = 0.0$, $q = 1.0$, and $m = 0.005$. Not surprisingly, the simulations yield curves that may be fitted accurately to the form

$$\tau_e = \tau_y + h_\infty\gamma^p_e + (\tau_\infty-\tau_y)\tanh\{((h_s-h_\infty)/(\tau_\infty-\tau_y))\,\tau^p_e\}, \tag{4.22}$$

where τ_y is as above, and where the effective plastic shear strain γ^p_e is $\gamma_e-\tau_e\div\mu$. When calculating τ_e and γ_e from the polycrystal results, $\boldsymbol{S}$ in (4.5) was taken as the deviator of Kirchhoff stress, and ϵ_1 and ϵ_2 in (4.5) were taken as the logarithmic strains in the x_1- and x_2-directions, respectively. Note that the use of the deformation-type measure of effective shear strain (4.5) is valid here because in the two compression simulations the loading is (very nearly) proportional: ϵ_1 and ϵ_2 closely correspond to the principal values of logarithmic strain. Also, when calculating γ^p_e from the polycrystal results, $\mu = 273.2\tau_o$ (which is the value of $\bar{L}^o_{1212} = \bar{L}^o_{1313} = \bar{L}^o_{2323}$ for the distribution with 489 grains) was used. The meanings of the other parameters which appear in (4.22) may be ascertained by identifying them with their counterparts of the single-slip relation (2.10). The first polycrystal simulation may be fit closely

with the constants

$$\tau_y = 1.50\tau_0, \quad h_s = 22.8\tau_0, \quad \tau_\infty = 2.92\tau_0, \quad h_\infty = 0.0199\tau_0, \tag{4.23}$$

and the second with

$$\tau_y = 1.60\tau_0, \quad h_s = 22.3\tau_0, \quad \tau_\infty = 3.00\tau_0, \quad h_\infty = 0.00429\tau_0, \tag{4.24}$$

where τ_0 is as in §2.1. These two hardening curves are used in the following phenomenological calculations: the material characterization (4.23) will be referred to as material I; and characterization (4.24), material II. Both materials I and II are taken to have $\mu = 273.2\tau_0$.

The specific boundary conditions used in the phenomenological calculations are the extension-shear conditions of §1.2: the form of the deformation gradient is as in (1.1), and the boundary condition sets are those described therein. Subsequently, the condition $e = 1$ will be referred to as constrained; and the condition $\sigma_{11} = \sigma_{22} = 0$, unconstrained. The faces of the material element (depicted in figure 1) defined by the unit normals $\pm e_3$ are taken as traction free, which alludes to a traction free lateral surface on a torsion specimen. Under these conditions, the stress deviator $\boldsymbol{S}$ corresponds to the Cauchy stress, which because of incompressibility, corresponds to the Kirchhoff stress $\boldsymbol{\tau}$.

For the constrained case, the resulting curves of stress versus strain generated by J_2-corner theory are presented in figure 22. For comparison's sake, results of two polycrystal simulations are also included in the figure. Both polycrystal simulations are characterized by $h_s = 0.0$, $q = 1.0$, $m = 0.005$, and the 'fully constrained torsion' boundary condition set. After initial yield, the phenomenological materials exhibit hyperelastic (total loading) response until about $\gamma = 0.5$, where the response becomes transitional and the stress–strain curves flatten out. Both materials I and II give effectively the same normal stress response whereas their shear-stress response differs by some (rather small) amount. Although not explicitly shown, the shear-stress–shear-strain curves for the constrained corner theory materials are nearly coincident with those of the unconstrained corner theory materials, as per the predictions of §3. As seen in figure 22, the agreement with the polycrystal predictions is quite satisfactory.

The corresponding set of curves for the F.M. evolution version of kinematic hardening theory are presented in figure 23. Again, the normal stress response of materials I and II is effectively the same. The shear stress curves of these materials have been made quite close to those of the polycrystals by proper choice of the value of the damping parameter A. As seen in the figure, the magnitude of the normal stresses predicted by this model is somewhere between those predicted by J_2-corner theory and the classical J_2-flow theory presented in §1.2 (which would predict $\tau_{11} = \tau_{22} = 0$). The magnitude of the normal stresses may be increased by using a smaller value of A, but doing so would cause the shear stresses to dip down below those of the polycrystals. As is the case for the corner theory materials, the τ_{21}–γ curves of the F.M. materials are nearly unaffected by the choice of boundary conditions, at least for $A = 40$.

For the unconstrained case, plots of extensional stretch e against shear strain γ for both J_2-corner theory materials and F.M. evolution materials are given in figure 24. The polycrystal curves of extensional stretch (which was referred to as F_{22} in §3) shown in the figure belong to the same two polycrystals of figures 22 and 23, but here the 'unconstrained torsion' boundary conditions are used. As in the constrained case, the corner theory predictions are in good agreement with the polycrystals', and the F.M. response is between those of J_2-corner theory and J_2-flow theory.

PHILOSOPHICAL TRANSACTIONS OF THE ROYAL SOCIETY A MATHEMATICAL, PHYSICAL & ENGINEERING SCIENCES

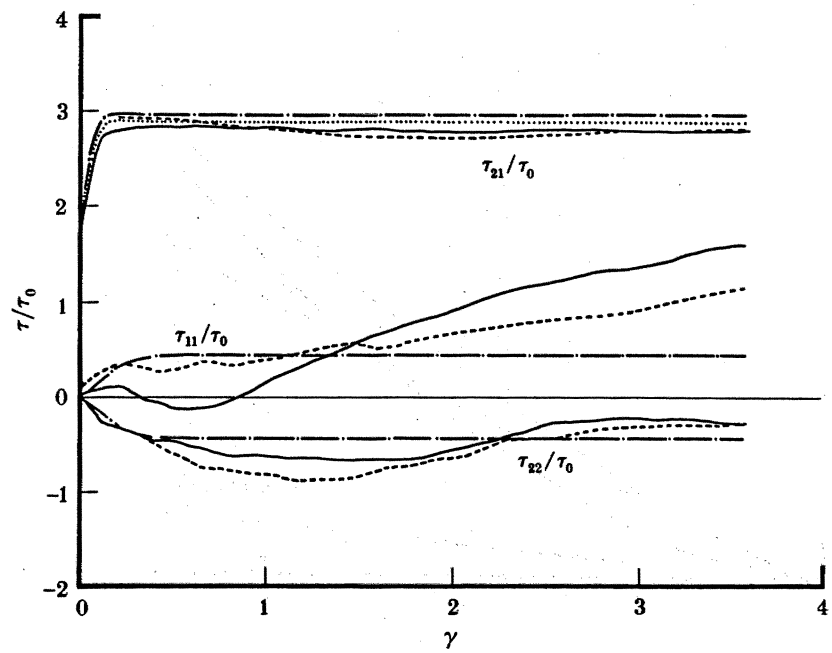

FIGURE 22. Stress response under 'constrained' shear for the two J_2-corner theory materials, material I (····) and material II (—·—), as described by equations (4.23) and (4.24), respectively. These are compared with the response of the '300' grain polycrystal (——) and the '489' grain polycrystal (----) deformed by 'constrained' shear.

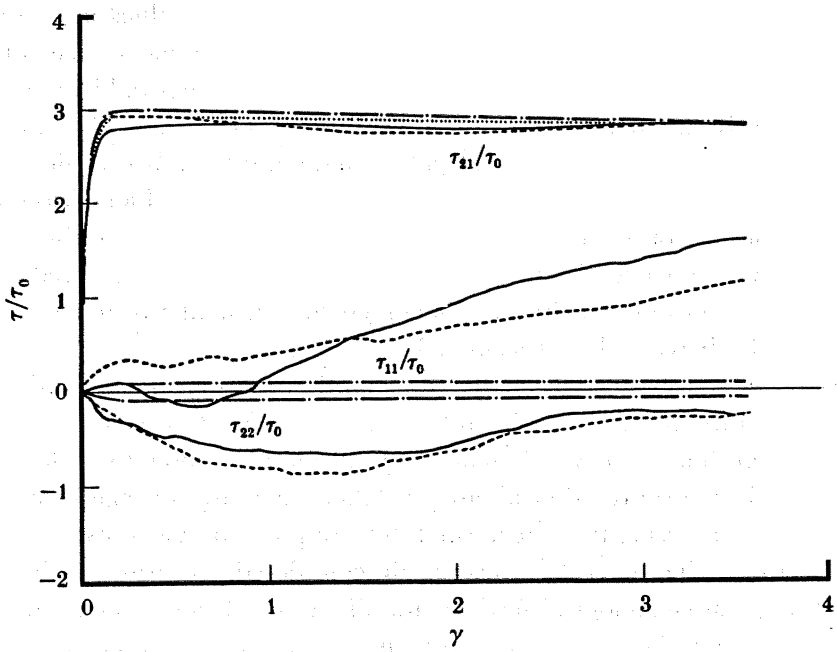

FIGURE 23. Stress response under 'constrained' shear for materials I (····), and II (—·—) obeying the F.M. version of kinematic hardening. The curves showing polycrystal response are the same as those in figure 22.

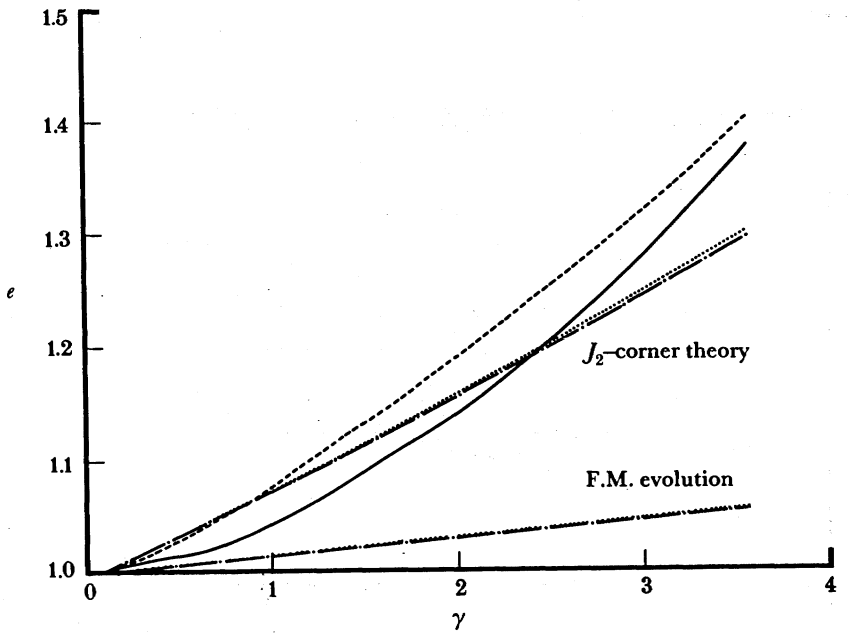

FIGURE 24. The 'Swift effect' for 'unconstrained' shear of materials I (· · · ·) and II (—·—) as predicted by J_2-corner theory and F.M. kinematic hardening theory. Curves showing the polycrystal response for the '300' grain distribution (——) and the '489' grain distribution (– – – –) are shown for comparison.

Although the J_2-corner theory predictions agree excellently with those of the polycrystal model (especially out to about $\gamma = 2$), experimental data for e tend to lie much closer to the F.M. prediction. As mentioned previously, the low experimental values of e are probably caused by constraints that act on the test specimen (it is difficult to remove such constraints in practice) and one wonders if a totally constraint-free test specimen would increase e to the extent that is indicated by the polycrystal model. If this proves to be the case, then the value of J_2-corner theory for localization analysis of polycrystalline materials is evident. The main difficulty in such analyses is the correct prediction of the initial mode of localization (which is the dominant aspect of such problems). The localization modes probably establish themselves at strain levels below 2, and hence, J_2-corner theory would be useful for such predictions. Also, the amount of computation required by the phenomenological model is much less than that required by a physically based polycrystal model.

The stress–strain curves obtained from the K evolution version of kinematic hardening theory are shown in figure 25. The polycrystal curves in the figure are the same as those in figures 22 and 23. Even though the τ_e–γ_e^p relation (4.22) increases monotonically, the K-type shear stresses drop rather abruptly after about $\gamma = 0.25$. Given the strange behaviour of the shear stresses, it is quite surprising that the normal stress response provided by this model is not all that bad, at least over the interval of shear strain considered. Contrary to the predictions of the two preceding phenomenological models, and like those of the hyperelastic material of §1.2, the K evolution material τ_{21}–γ curves are quite sensitive to the choice of boundary conditions. This effect is illustrated in figure 26. Also in figure 26, the K-type extensions for the unconstrained case are compared to the polycrystal predictions. In this figure, the curves of the polycrystalline response are the same as those appearing in figure 24, and as is indicated, this model overestimates these extensions by more than an order of magnitude. Perhaps the large

normal (especially extensional) effects, the abrupt drop in shear stress, and the shear-stress sensitivity to boundary conditions all could be reduced by writing the back stress evolution equation in the form of (4.17), with $\overset{*}{\alpha}$ replacing $\overset{\nabla}{\alpha}$.

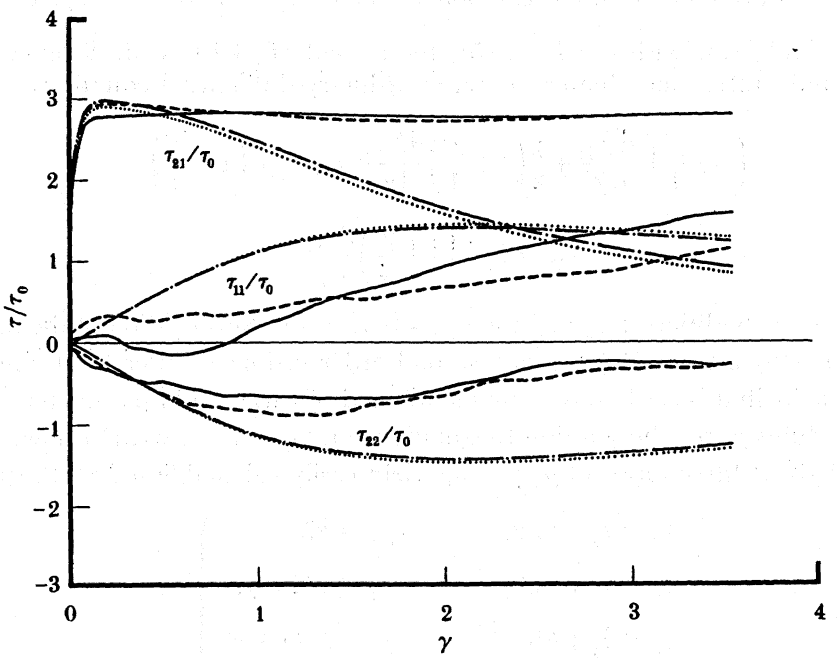

FIGURE 25. Stress response under 'constrained' shear for materials I (····) and II (—·—) obeying the K version of kinematic hardening. The curves depicting the polycrystal responses are the same as those in figures 22 and 23.

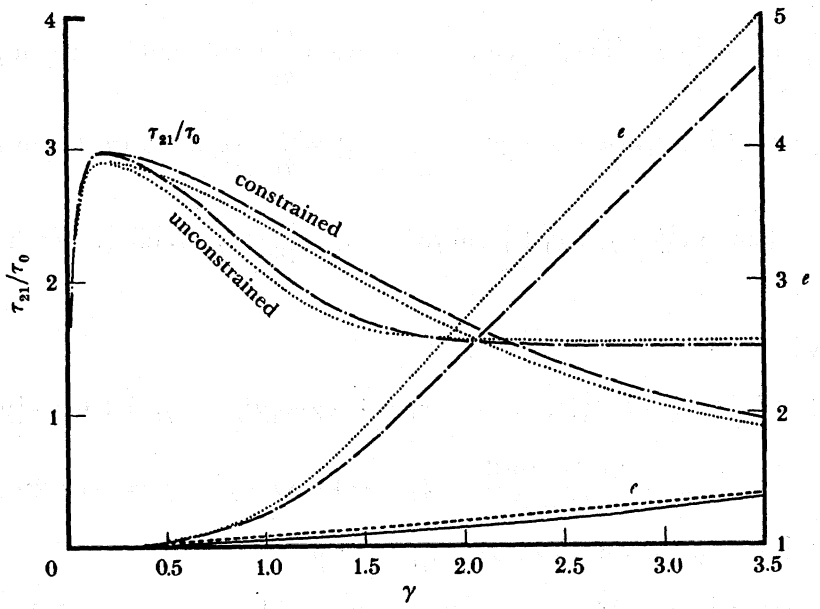

FIGURE 26. The 'Swift effect' for 'unconstrained' shear of materials I (····) and II (—·—) as predicted by K kinematic hardening theory. Curves for 'constrained' shear are also shown to illustrate the sensitivity to boundary conditions of the K shear stress response. The curves showing the polycrystal responses are the same as those in figure 24.

To investigate the rather strange solutions provided by the K version of kinematic hardening, we now turn to some simple cases for which closed form solutions may be found. Specifically, attention is restricted to the constrained case and the material is taken as rigid-plastic so that the only non-vanishing components of $\boldsymbol{D}^{\mathrm{p}}$ are $D^{\mathrm{p}}_{12} = D^{\mathrm{p}}_{21} = \frac{1}{2}\dot{\gamma}$. Using $\gamma^{\mathrm{p}}_{\mathrm{e}} = \gamma$, equations (1.8) and (1.9) with $e = 1$, (4.15), the second of (4.18) with $\overset{*}{\boldsymbol{S}}$ replacing $\overset{\nabla}{\boldsymbol{S}}$ and $\mu \to \infty$, (4.20) and (4.21), one obtains the set of ordinary differential equations

$$\left(1+\frac{\gamma^2}{4}\right)^2 \frac{\mathrm{d}^2\tau_{11}}{\mathrm{d}\gamma^2} + \frac{\gamma}{2}\left(1+\frac{\gamma^2}{4}\right)\frac{\mathrm{d}\tau_{11}}{\mathrm{d}\gamma} + \tau_{11} = \mu_{\mathrm{t}}\left(1+\frac{\gamma^2}{4}\right), \tag{4.25$_1$}$$

$$\tau_{21} = \tau_{\mathrm{y}} + \left(1+\frac{\gamma^2}{4}\right)\frac{\mathrm{d}\tau_{11}}{\mathrm{d}\gamma} \tag{4.25$_2$}$$

subject to the initial conditions $\tau_{21} = \tau_{\mathrm{y}}$ and $\tau_{11} = 0$ at $\gamma = 0$. Substitution of the independent variable $2\arctan(\frac{1}{2}\gamma)$ into (4.25$_1$) yields a second-order ordinary differential equation with constant coefficients that is easily solved by the method of variation of parameters. Hence, for any tangent modulus $\mu_{\mathrm{t}}(\gamma)$, the solution to equations (4.25) may be written down in integral form. We will look at three forms of $\mu_{\mathrm{t}}(\gamma)$ that yield easily calculable integrals, specifically

$$\left.\begin{aligned} \tau_{\mathrm{e}} &= \tau_{\mathrm{y}} + \mu^{\mathrm{o}}_{\mathrm{t}}\gamma, & \mu_{\mathrm{t}} &= \mu^{\mathrm{o}}_{\mathrm{t}}, \\ \tau_{\mathrm{e}} &= \tau_{\mathrm{y}} + k\sqrt{\gamma}, & \mu_{\mathrm{t}} &= k/2\sqrt{\gamma}, \\ \tau_{\mathrm{e}} &= \tau_{\mathrm{y}} + h\ln(1+\gamma), & \mu_{\mathrm{t}} &= h/(1+\gamma), \end{aligned}\right\} \tag{4.26}$$

which will be referred to as linear, power law, and logarithmic materials, respectively. These three τ_{e}–$\gamma^{\mathrm{p}}_{\mathrm{e}}$ relations are plotted in figure 27 with $\mu^{\mathrm{o}}_{\mathrm{t}} = 0.2\tau_{\mathrm{y}}$, $k = 0.4\tau_{\mathrm{y}}$ and $h = 0.497\tau_{\mathrm{y}}$. The solutions of (4.25) for the linear, power law, and logarithmic materials are

$$\left.\begin{aligned} \tau_{21} &= \tau_{\mathrm{y}} + \frac{\mu^{\mathrm{o}}_{\mathrm{t}}}{q_1}\{4q_2\arctan\tfrac{1}{2}\gamma + 2\gamma\ln q_1 - q_2\gamma\}, & \tau_{11} &= \frac{\mu^{\mathrm{o}}_{\mathrm{t}}}{q_1}\{4\gamma\arctan\tfrac{1}{2}\gamma - 2q_2\ln q_1 - \gamma^2\}, \\ \tau_{21} &= \tau_{\mathrm{y}} + \frac{k}{q_1}\{q_4\arctan q_5 + q_3\ln q_6 - q_2\sqrt{\gamma}\}, & \tau_{11} &= \frac{k}{q_1}\{-q_3\arctan q_5 + q_4\ln q_6 - \gamma\sqrt{\gamma}\}, \\ \tau_{21} &= \tau_{\mathrm{y}} + \frac{h}{5q_1}\{-q_7\arctan\tfrac{1}{2}\gamma + q_8\ln q_1 + \tfrac{1}{4}q_9\ln q_{11}\}, & \tau_{11} &= \frac{h}{5q_1}\{2q_8\arctan\tfrac{1}{2}\gamma + \tfrac{1}{2}q_7\ln q_1 - q_{10}\ln q_{11}\}, \end{aligned}\right\} \tag{4.27$_1$}$$

respectively, with

$$\left.\begin{aligned} q_1 &= 1+\tfrac{1}{4}\gamma^2, & q_2 &= 1-\tfrac{1}{4}\gamma^2, & q_3 &= 1-\gamma-\tfrac{1}{4}\gamma^2, & q_4 &= 1+\gamma-\tfrac{1}{4}\gamma^2, \\ q_5 &= \frac{2\sqrt{\gamma}}{2-\gamma}, & q_6 &= \frac{\gamma+2\sqrt{\gamma}+2}{\sqrt{(4+\gamma^2)}}, & q_7 &= -4-8\gamma+\gamma^2, & q_8 &= -4+2\gamma+\gamma^2, \\ q_9 &= 12-16\gamma-3\gamma^2, & q_{10} &= -4-3\gamma+\gamma^2, & q_{11} &= 1+\gamma. \end{aligned}\right\} \tag{4.27$_2$}$$

Note that the $\arctan q_5$ in (4.27) returns values between $\frac{1}{2}\pi$ and π for $\gamma > 2$. In all other cases the inverse tangent function refers to the principal branch. Plots of the solutions (4.27) are shown in figure 28, where the constants given just below (4.26) have been used. Note also that the τ_{21}–γ curve for the power-law material exhibits the most pronounced dipping behaviour

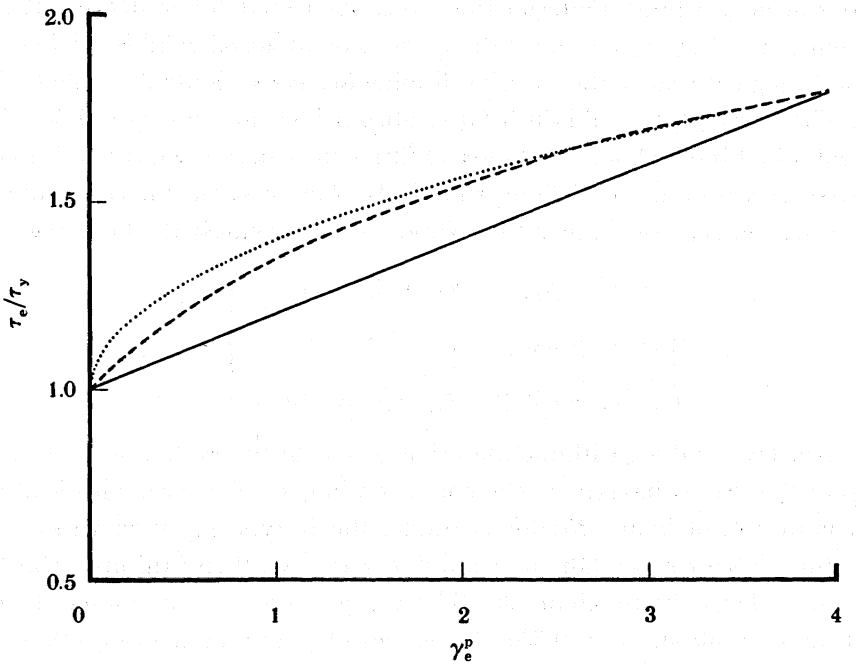

FIGURE 27. Simple effective shear stress-effective plastic shear strain curves for which closed-form solutions to equation (4.25) may be found for a linear hardening material (——), power law hardening material (· · · ·), and a logarithmic hardening material (– – – –).

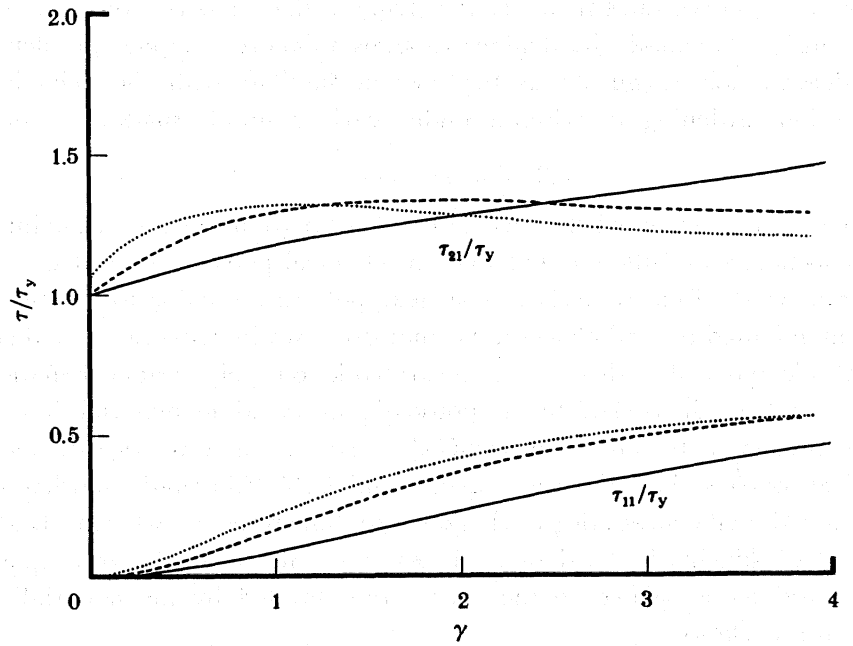

FIGURE 28. Stress response under 'constrained' shear for materials obeying K kinematic hardening theory and using the linear (——), power law (· · · ·), and logarithmic (– – – –) hardening curves shown in figure 27. Note that $\tau_{22} = \tau_{11}$ here.

PHILOSOPHICAL TRANSACTIONS OF THE ROYAL SOCIETY A MATHEMATICAL, PHYSICAL & ENGINEERING SCIENCES

whereas that for the logarithmic material dips to a somewhat lesser degree. Referring to figure 27, it is seen that the τ_e–γ_e^p curve for the power-law material exhibits higher curvature than does that of the logarithmic material. This dipping behaviour is attributable to this rather high curvature. The curve (4.22) exhibits a fairly abrupt knee around $\gamma_e^p = 0.25$. Hence, the high curvature exhibited by the knee of relation (4.22) is the cause of the (undesirable) abrupt drop in shear stress shown in figure 25. The undesirable behaviour of the constrained K-type solutions is a transient effect: for large γ the relations (4.27) exhibit the behaviour

$$\left.\begin{aligned} &\tau_{21}-\tau_y \sim \mu_t^o\gamma, && \tau_{11} \sim 4\mu_t^o \ln\gamma,\\ &\tau_{21}-\tau_y \sim k\sqrt{\gamma}, && \tau_{11} \to k\pi,\\ &\tau_{21}-\tau_y \sim h\ln\gamma, && \tau_{11} \to \tfrac{4}{5}h\,(\pi-\ln 2), \end{aligned}\right\} \tag{4.28}$$

for the linear, power law, and logarithmic materials, respectively. Note that in every case the τ_{21}–γ curve approaches the behaviour of the corresponding τ_e–γ_e^p curve. This is also true for the constrained materials of figure 25: for example, the K-type τ_{21}–γ curve for material I reaches a minimum of about $\tau_{21} = 0.3\tau_o$ at around $\gamma = 10$, and then exhibits a constant slope of h_∞ for values of γ larger than about 25. The τ_{11}–γ curve for this material appears to have a constant value of about $\tau_{11} = 0.35\tau_o$ for values of γ greater than *ca.* 60. The longest transient is exhibited by the power-law material where τ_{11} reaches 90 % of its asymptotic value at around $\gamma = 570$.

Hopefully, the reader has been left with the impression that the practice of merely replacing $\overset{\nabla}{\boldsymbol{\alpha}}$ (in the traditional Prager–Ziegler form of back stress evolution) by some other objective rate of $\boldsymbol{\alpha}$ is a rather precipitous fix. As shown here, the K form would appear to be adequate if one only looked at the case of constant tangent modulus, but in fact this form is highly sensitive to the shape of the τ_e–γ_e^p curve (and hence to the shape of the uniaxial stress–strain relation). Obviously, the use of kinematic hardening relations in more complex problems of non-homogeneous deformation requires that the user be familiar with the behaviour of the particular evolution-hardening description under various simple modes of homogeneous deformation.

4.3. *Closing remarks*

In this paper we have examined the mechanics of shear from several viewpoints: those of classical macromechanics and those of our micromechanical polycrystal model.

Within the framework of macromechanics, a 'textbook' introduction to the shear problem was given that highlighted the differences in normal stress–strain response as predicted by the classical hyperelastic and J_2-flow theories. As illustrated by our polycrystal calculations and by the experiments of others, the constitutive response of polycrystalline materials lies somewhere between those predicted by the two classical theories. In this regard, more recent phenomenological models, i.e. J_2-corner theory and F.M. kinematic hardening theory, have been shown to describe more adequately polycrystalline response, whereas the description afforded by the K kinematic hardening theory was shown to be inadequate. These inadequacies proved to be related to the curvature exhibited by the material's effective-stress–effective-strain relation.

Within the framework of micromechanics, several important observations and correlations have been made. Experimentally observed texture transitions such as those described in §3.1 have been predicted by our model and have been shown to be related to the overall response

of the aggregate. We have found that the gross rotations exhibited by the texture components are related to the normal strain response of the polycrystal as a whole, whereas the overall normal stress response is associated with textures that are more or less unrotated. Consistent with these observations, our calculated axial strain transients of figure 20 correspond to the gross texture rotations depicted in figure 21*b–d*. These transients are also observed experimentally. Although our calculated textures have a tendency to be too sharp, the decreased magnitude of plastic spin with increased strain-rate sensitivity has been shown to be at least partly responsible for the more diffuse textures that are characteristic of experimental observation. We have also found that increasing the strain-rate sensitivity captures some of the phenomena observed in experiments done at elevated temperatures.

This work was supported by the U.S. National Science Foundation. R.J.A. gratefully acknowledges support from the Metallurgy, Polymer and Ceramics Section through grant DMR 8503554. Supercomputing at Boeing Computer Services and at the San Diego Supercomputer Center was made possible through this grant and NSF's Office of Advanced Scientific Computing. Supercomputing at Sandia National Laboratories, Livermore, California, was supported by the U.S. Department of Energy under contract DE-AC04-76DP00789. T.C.L. gratefully acknowledges support provided by Sandia National Laboratories under the same contract. S.H. and A.N. are grateful for the support provided by the Materials Research Group at Brown University, funded by the U.S. National Science Foundation through grant DMR 8714665.

References

Aernoudt, E. & Gil-Sevillano, J. G. 1973 *J. Iron Steel Inst.* **211**, 718.
Asaro, R. J. 1979 *Acta metall.* **27**, 445.
Asaro, R. J. 1983*a* Micro and macromechanics of crystals and polycrystals. In *Adv. Appl. Mech.* **23**, 1.
Asaro. R. J. 1983*b* *J. appl. Mech.* **50**, 921.
Asaro, R. J. & Needleman, A. 1985 *Acta metall.* **33**, 923.
Asaro, R. J. & Rice, J. R. 1977 *J. Mech. Phys. Solids* **25**, 309.
Backofen, W. A. 1950 *Trans. Am. Inst. Min. Engrs.* **188**, 1454.
Backofen, W. A. & Hundy, B. B. 1953 *Trans Am. Inst. Min. Engrs.* **197**, 61.
Billington, E. W. 1976 *J. Phys.* D**9**, 519, 533.
Bishop, J. F. W. & Hill, R. 1951*a* *Phil. Mag.* **42**, 1298.
Bishop, J. F. W. & Hill, R. 1951*b* *Phil. Mag.* **42**, 414.
Budiansky, B., Dow, N., Peters, R. & Shepherd, R. 1951 *Proc. 1st U.S. National Congress Appl. Mech., ASME, New York*, p. 503.
Canova, G. R., Kocks, U. F. & Jonas, J. J. 1984 *Acta metall.* **32**, 211.
Canova, G. R., Kocks, U. F., Tome, C. N. & Jonas, J. J. 1985 *J. Mech. Phys. Solids*, **33**, 371.
Chadwick, P. 1976 *Continuum mechanics: concise theory and problems*, p. 71. New York: John Wiley and Sons.
Chang, Y. W. & Asaro, R. J. 1981 *Acta metall.* **29**, 241.
Christoffersen, J. & Hutchinson, J. W. 1979 *J. Mech. Phys. Solids* **27**, 465.
Dienes, J. K. 1979 *Acta mech.* **32**, 217.
Fressengeas, C. & Molinari, A. 1983 *C. r. Séanc. Acad. Sci. Paris* (II) **297**, 7.
Gibbard, W. R. 1951 *Trans. Am. Inst. Min. Engrs.* **191**, 1062.
Gil-Sevillano, J., van Houtte, P. & Aernoudt, E. 1975 *Z. Metallk* **66**, 367.
Gurtin, M. 1981 *An introduction to continuum mechanics*, p. 177. New York: Academic Press.
Hahn, H. T. 1974 *Int. J. Solids Struct.* **10**, 111.
Harren, S. V., Dève, H. E. & Asaro, R. J. 1988 *Acta metall.* **36**, 2435.
Hart, E. W. 1976 *J. Engng. Mater. Technol.* **98**, 193.
Hecker, S. S. & Stout, M. G. 1982 *Strain hardening of heavily cold-worked metals*, Los Alamos National Laboratory Report.
Hill, R. 1950 *The mathematical theory of plasticity*, p. 325. Oxford: Clarendon Press.

PHILOSOPHICAL TRANSACTIONS OF THE ROYAL SOCIETY A MATHEMATICAL, PHYSICAL & ENGINEERING SCIENCES

Hill, R. 1966 *J. Mech. Phys. Solids* **14**, 95.
Hill, R. 1970 *Proc. R. Soc. Lond.* A **314**, 457.
Hill, R. 1972 *Proc. R. Soc. Lond.* A **326**, 131.
Hill, R. & Havner, K. S. 1982 *J. Mech. Phys. Solids* **30**, 5.
Hill, R. & Rice, J. R. 1972 *J. Mech. Phys. Solids* **20**, 401.
Honneff, H. & Meeking, H. 1978 In *Texture of materials* (ed. G. Gottstein & K. Lucke), p. 265. Berlin: Springer.
Hughes, D. A. 1986 Ph.D. thesis, Stanford University.
Hughes, D. E. R. 1952 *J. Iron Steel Inst.* **170**, 214.
Hutchinson, J. W, & Tvergaard, V. 1980 *Int. J. Mech. Sci.* **22**, 339.
Key, S. W. 1984 In *Mechanics of elastic and inelastic solids* **6**: *theoretical foundations for large-scale computations for nonlinear material behavior* (ed. S. Nemat-Nasser, R. J. Asaro & G. A. Hegemier). Dordrecht: Martinus Nijhoff Publishers.
Kocks, U. F. 1970 *Metall. Trans.* **1**, 1121.
Lee, E. H. 1969 *J. appl. Mech.* **36**, 1.
Lee, E. H., Mallett, R. L. & Wertheimer, T. B. 1983 *J. appl. Mech.* **50**, 554.
Lowe, T. C. & Asaro, R. J. 1985 In *AIME Symposium on Texture, Microstructure, and Yield Surfaces, Toronto, Ontario, Canada.*
McMeeking, R. M. 1982 *Int. J. Solids Struct.* **18**, 199.
Montheillet, F., Cohen, M. & Jonas, J. J. 1984 *Acta metall.* **32**, 2077.
Montheillet, F., Gilormini, P. & Jonas, J. J. 1985 *Acta metall.* **33**, 705.
Nadai, A. 1950 *Theory of flow and fracture of solids*, vol. 1, p. 349. New York: McGraw Hill.
Nagtegaal, J. C. & de Jong, J. E. 1982 In *Plasticity of metals at finite strain: theory, computation and experiment* (ed. E. H. Lee & R. L. Mallett), vol. 65. Stanford University Division of Applied Mechanics, Stanford, California.
Peirce, D., Asaro, R. J. & Needleman, A. 1982 *Acta metall.* **30**, 1087.
Peirce, D., Asaro, R. J. & Needleman, A. 1983 *Acta metall.* **31**, 1951.
Portevin, P. A. 1970 *Revue Métall.* **67**, 761.
Poynting, J. H. 1909 *Proc. R. Soc. Lond.* A **82**, 546.
Rice, J. R. 1971 *J. Mech. Phys. Solids* **19**, 433.
Rivlin, R. S. 1953 *J. rat. Mech. Analysis* **2**, 53.
Ronay, M. 1966 *J. Inst. Metals* **94**, 392.
Ronay, M. 1967 *Int. J. Solids Struct.* **3**, 167.
Ronay, M. 1968 *Int. J. Solids Struct.* **4**, 509.
Shrivastava, S. C., Jonas, J. J. & Canova, G. 1982 *J. Mech. Phys. Solids* **30**, 75.
Stören, S. & Rice, J. R. 1975 *J. Mech. Phys. Solids* **20**, 421.
Swift, H. W. 1947 *Engineering* **163**, 253.
Taylor, G. I. 1938*a* *J. Inst. Metals* **62**, 307.
Taylor, G. I. 1938*a* In *Stephen Timoshenko 60th anniversary volume* (ed. J. M. Lessels), p. 218. New York: Macmillan.
Tvergaard, V., Needleman, A. & Lo, K. K. 1981 *J. Mech. Phys. Solids* **29**, 115.
Van Arsdale, W. E., Hart, E. W. & Jenkins, J. T. 1980 *J. appl. Phys.* **51**, 953.
van Houtte, P. & Aernoudt, E. 1976 *Mater. Sci. Engng.* **23**, 11.
Williams, R. O. 1962 *Trans. Am. Inst. Min. Engrs.* **224**, 129.

PHILOSOPHICAL TRANSACTIONS OF THE ROYAL SOCIETY A MATHEMATICAL, PHYSICAL & ENGINEERING SCIENCES